Contribution to the study of the response of heterogeneous materials subjected to environmental and mechanical loading

Matthieu Le Saux

HABILITATION À DIRIGER DES RECHERCHES

présentée à

L'UNIVERSITÉ BRETAGNE SUD

ED n°647 : Sciences pour l'Ingénieur

par

Matthieu LE SAUX

Contribution à l'étude de la réponse de matériaux hétérogènes soumis à des sollicitations environnementales et mécaniques

Contribution to the study of the response of heterogeneous materials subjected to environmental and mechanical loading

Soutenue le 14 Janvier 2025 devant le jury composé de :

Michel CORET Professeur, École Centrale de Nantes, GeM	Rapporteur
Ivan GUILLOT Professeur, Université Paris-Est Créteil, ICMPE	Rapporteur
Nicolas SAINTIER Professeur, Arts et Métiers, I2M	Rapporteur
Jacques BESSON Directeur de Recherche, Mines Paris, CdM	Examinateur
Jean-Luc BOUVARD Professeur, Mines Paris, CEMEF	Examinateur
Anne-Françoise GOURGUES-LORENZON Professeure, Mines Paris, CdM	Présidente
Philippe PILVIN Professeur émérite, Université Bretagne Sud, IRDL	Garant

ENSTA | Institut Polytechnique de Paris, IRDL, UMR CNRS 6027
2 rue François Verny, 29200 Brest, France

A Rozenn, Yorell et Ohann.

Remerciements

Tout d'abord, je remercie sincèrement Jacques Besson, Jean-Luc Bouvard, Michel Coret, Anne-Françoise Gourgues-Lorenzon, Ivan Guillot, Philippe Pilvin et Nicolas Saintier d'avoir accepté de faire partie du jury.

Je remercie par ailleurs les organismes qui ont soutenu les projets de recherche présentés dans ce document. Merci en particulier aux personnes directement impliquées dans la gestion de ces projets.

Les travaux présentés dans ce document sont le fruit d'un travail d'équipes. Je remercie l'ensemble des personnes avec qui j'ai eu la chance de collaborer, notamment les étudiants et les collègues avec qui j'ai travaillé en synergie (je ne me risque à les nommer ici par peur d'en oublier...).

Contents

Glossary

Acronyms

at%	atomic percent
AE	acoustic emission
ANR	Agence nationale de la recherche
ANRT	Association nationale de la recherche et de la technologie
CEA	Commissariat à l'énergie atomique et aux énergies alternatives
CIFRE	Convention industrielle de formation par la recherche
(µ-)CT	(micro) X-ray computed tomography
DIC	digital image correlation
DSC	differential scanning calorimetry
EBSD	electron backscatter diffraction
ENSTA	École nationale supérieure de techniques avancées
EPMA	electron-probe micro analysis
µ-ERDA	micro elastic recoil detection analysis
FE	finite element
FEG	field emission gun
FFT	fast Fourier transform
HT	high temperature
IR	infrared
IRDL	Institut de recherche Dupuy de Lôme
µ-LIBS	micro laser induced breakdown spectroscopy
LOCA	loss-of-coolant accident
MCU	microcellular polyurethane
OM	optical microscopy
PA66 GF50	Polyamide 66 reinforced with 50 w% of short glass fibers
PEEK CF30	PolyEtherEtherKetone reinforced with 30 w% of short carbon fibers
PVD	physical vapor deposition
PWR	pressurised water nuclear reactor
SEM	scanning electron microscopy
SFRT	short fiber-reinforced thermoplastic
TEM	transmission electron microscopy
wppm	weight part per million
w%	weight percent

XRD	X-ray diffraction

Symbols

RH	relative humidity
R_σ	(minimum to maximum) stress ratio
T	test temperature
T_g	glass transition temperature

Introduction

This dissertation is submitted as part of my application for the diploma of "habilitation à diriger des recherches". According to article 1 of the french order of 23 November 1988: "L'habilitation à diriger des recherches sanctionne la reconnaissance du haut niveau scientifique du candidat, du caractère original de sa démarche dans un domaine de la science, de son aptitude à maîtriser une stratégie de recherche dans un domaine scientifique ou technologique suffisamment large et de sa capacité à encadrer de jeunes chercheurs". Certainly, but I also see the preparation of my application as an opportunity to "take a break", to step back a little, to take stock of my career, to identify the logic behind it, and finally to establish a guideline for the future.

My (applied) research activities are focused on the behavior (mainly mechanical) of heterogeneous materials. My first forays into research began in 2005, during my Master's internship at the research institute in civil and mechanical engineering (GeM) [1]. This work was concerned with characterization and modeling of the anisotropy of mechanical behavior induced by the Mullins effect in elastomers. Between 2005 and 2008, I completed a PhD [2] thesis at the Section of irradiated materials studies [3] of the french alternative energies and atomic energy commission (CEA [4]) Paris-Saclay, in collaboration with the "Centre des matériaux" from "École des Mines ParisTech". This work concentrated on the mechanical behavior and fracture of zirconium alloys under specific conditions that require consideration of various factors, such as irradiation, hydrogen absorption, temperature, and mechanical loading.

In 2008, I joined the Section for applied metallurgy research [5] of CEA Paris-Saclay as a research engineer. Over a ten-year period, I conducted research on the behavior of metallic materials for nuclear applications under conditions where these materials may be subjected to significant temperature variations (several hundred °C), an oxidizing environment (steam), and mechanical loading. My research has been primarily focused on zirconium alloys, as well as chromium-coated zirconium alloys, and martensitic steels. My particular interest was in their corrosion at high temperature (HT, typically above 800 °C), their thermomechanical behavior, and

[1] "Institut de recherche en génie civil et mécanique" in french.
[2] *Philosophiæ doctor*.
[3] "Service d'étude des matériaux irradiés" in french.
[4] "Commissariat à l'énergie atomique et aux énergies alternatives" in french.
[5] "Service de recherches métallurgiques appliquées" in french.

the influence of microstructural changes occurring under the conditions of interest, such as solid phase changes, oxidation, or absorption of oxygen and hydrogen.

In 2018, I left CEA and joined the "École nationale supérieure de techniques avancées Bretagne" (ENSTA Bretagne), now ENSTA | Institut Polytechnique de Paris, since early 2025, as a lecturer-researcher. I conduct my research activities within the team working on the behavior and durability of heterogeneous materials at the Dupuy de Lôme research institute (IRDL [6]) laboratory. I have aligned my activities with those of the group I have joined. The focus is now on the thermomechanical behavior and fatigue resistance of (heterogeneous) polymer-based materials when subjected to cyclic mechanical loading (often multiaxial), in environments (especially temperature and humidity) that are likely to vary in some cases. More specifically, to date, I have mainly worked on short fiber-reinforced thermoplastic matrix composites, long fiber-reinforced thermoset matrix composites, and elastomer foams.

This version of the manuscript does not include a detailed presentation of my career and my teaching, research and supervisory activities. This dissertation summarizes the main research projects to which I contributed *after completing my PhD thesis*. For those who are interested, the results of my Master's thesis has been published in 2016 (Marckmann et al., 2016) and my PhD thesis work is presented in the following references: Le Saux (2008), Le Saux et al. (2008), Le Saux et al. (2010), and Le Saux et al. (2015). The work presented in this document is the result of numerous collaborations [7]. A number of the activities were conducted in collaboration with students or young researchers, including two Master 2 apprenticeships, five Master 1 internships, ten Master 2 internships, eight PhD theses (six of which were defended) and two post-doctoral fellowships.

The document is organized by topic:

1. Corrosion at HT and its consequences on the mechanical behavior of zirconium alloys.
2. Corrosion at HT and mechanical behavior of chromium-coated zirconium alloys.
3. Thermo-metallurgical-mechanical behavior of a martensitic steel at HT.
4. Thermomechanical behavior and fatigue of short fiber-reinforced thermoplastic composites.
5. Fatigue of thermoset composite laminates under compression.
6. Microstructure and mechanical behavior of elastomer foams.

A final chapter outlines the common thread of these activities and provides an overview of current research projects.

Only work that has already been made public is presented. Some of the work to which I contributed is therefore not presented. Wherever possible, references are provided to articles that have been published in peer-reviewed journals. Nevertheless,

[6] "Institut de recherche Dupuy de Lôme" in french.

[7] This is demonstrated by the hundreds of co-authors from approximately thirty different organizations with whom I have joint publications.

a few references are made to conference presentations or papers, when the results have not been published in journals and which I consider worthy of presentation in this document.

I have chosen not to provide a detailed and exhaustive overview of the current state of knowledge and work in each of the topics under discussion. Instead, I have chosen to focus on the essential elements to understand the industrial *context* and the scientific issues that arise from it, the *objectives* that have been set, the *approach* taken to achieve them, the main *results* obtained, and the main *conclusions* drawn. In terms of writing, my objective was to limit the length of each chapter (chapter 3, for example), or of each section when there are several in a chapter (section 1.2, for example), to a maximum of five pages, including figures, in order to ensure that this chapter does not exceed one hundred pages. Thus, this document contains minimal references, with the exception of those that I have contributed. It does not provide detail regarding the methods developed or the manner in which the analyses were conducted, nor does it include any equations. I encourage any frustrated readers to consult the cited documents for further references and information regarding the work carried out [8].

[8] These documents can be sent on request to the following e-mail address: `matthieu.le_saux@ensta.fr`.

Chapter 1

Corrosion at HT and mechanical response of zirconium alloys

Contents

1.1 Introduction

The fuel rod claddings of pressurized water nuclear reactors (PWRs) take the form of a tube with an external diameter of about 9.5 mm and a thickness of approximately 0.57 mm. They represent the primary barrier for confining radioactive products. During nominal operation, the claddings are immersed in the primary circuit water at approximately 300–340 °C (155 bar, with Li, B, and H_2). Fuel claddings are currently made of zirconium alloys [1]. In hypothetical accident scenarios such as a

[1] In particular, these alloys offer low absorption of thermal neutrons, good corrosion resistance, adequate mechanical properties, and good resistance to radiation.

loss-of-coolant accident (LOCA), the claddings may be exposed to steam at HT, between 700 and 1200 °C typically, for a few minutes before being cooled and quenched with water during reflooding of the reactor core (figure 1.1).

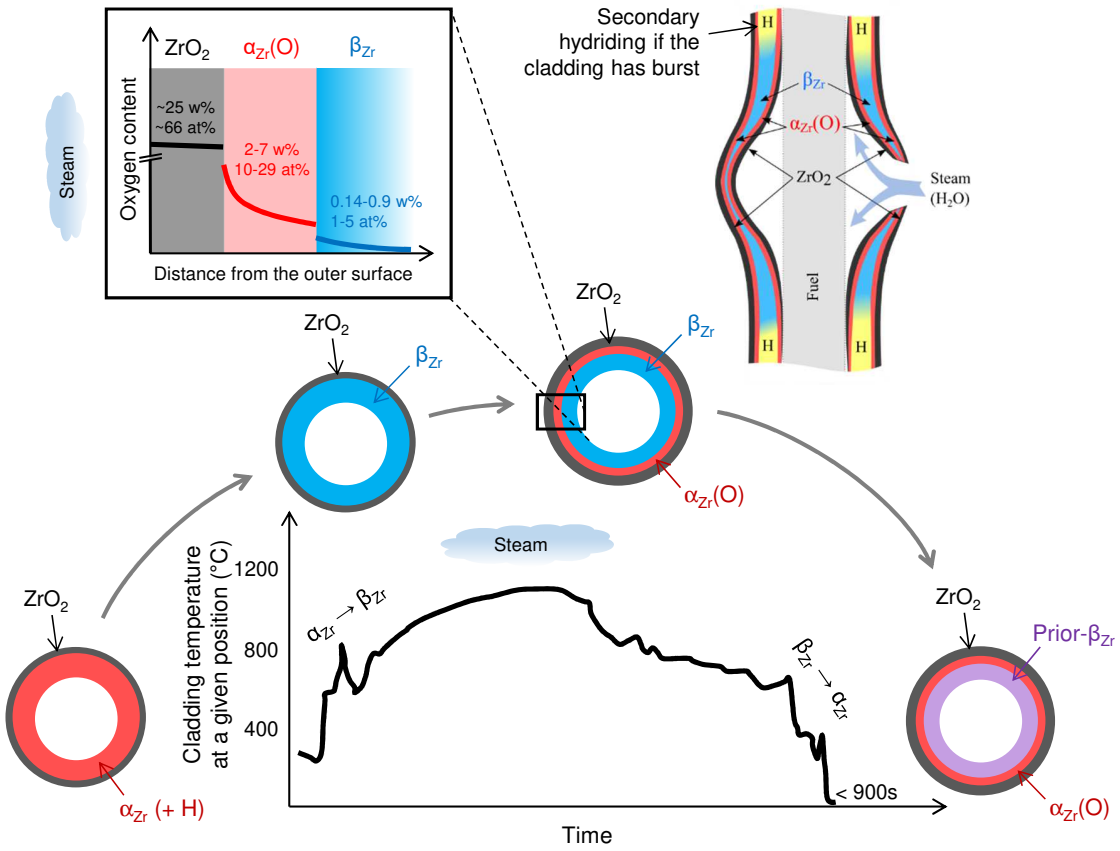

Figure 1.1 – Example of (large break) LOCA transient and schematic representation of the metallurgical changes taking place within the cladding made of a zirconium alloy (assuming that only the outer surface of the cladding oxidizes at HT).

Under these conditions, the material undergoes several microstructural changes, as illustrated in figure 1.1. On the one hand, a layer of zirconium oxide (zirconia, ZrO_2) growths, at a much faster rate than under normal operating conditions. It is composed of tetragonal zirconia (t_{ZrO2}) [2], or of a mixture of monoclinic zirconia (m_{ZrO2}) and t_{ZrO2}, depending on temperature in particular. On the other hand, the low-temperature hexagonal close-packed α_{Zr} phase of zirconium [3] undergoes a

[2] This phase is stable above 1170 °C for pure zirconia at equilibrium and atmospheric pressure. However, it can be stabilized at lower temperature by stresses, a small crystal size, or elements with a lower valence or a different size than zirconium.

[3] This phase is stable below 864 °C for pure zirconium, at equilibrium and atmospheric pressure. The temperature range in which it is stable depends in particular on the chemical composition of the material and the kinetics of temperature variation.

transformation into the HT body-centered cubic β_{Zr} phase during heating. A significant fraction of the oxygen resulting from the oxidation reaction by steam at HT diffuses into the metal. Once the oxygen solubility limit is reached in the β_{Zr} phase, a metallic layer of oxygen-stabilized α_{Zr} phase, designated $\alpha_{Zr}(O)$, forms between the oxide and the β_{Zr} phase layers. In certain conditions, a portion of the hydrogen generated by corrosion may be absorbed by the material and subsequently diffuse into the metal. During cooling after oxidation at HT, a significant proportion of t_{ZrO2} undergoes a transformation into m_{ZrO2}. In addition, the β_{Zr} phase undergoes a transformation back to the α_{Zr} phase, resulting in the formation of the so-called prior-β_{Zr} structure [4]. These processes are accompanied by a redistribution of chemical elements within the material. All these changes make the material heterogeneous at different scales, which naturally affects its mechanical response.

During the cooling at the end of the transient, the cladding is subjected to thermal stresses caused by thermal expansion gradients within the oxidized material and dimensional variations due to phase changes, as well as additional mechanical loading. To ensure the safe operation of the reactor, it is necessary to guarantee that the cladding would withstand the quenching mechanically and retain sufficient mechanical strength or residual ductility after the transient. To this end, the safety criteria require, among other things, that the maximum temperature of the cladding remains below a certain value [5], and that its level of oxidation does not exceed a certain threshold [6]. The use of new materials, the changes in reactor operating conditions and the implementation of enhanced safety standards necessitate the consideration of effects and phenomena that were not previously taken into account. It is not feasible to conduct multiple tests under real reactor conditions. Safety studies are largely based on numerical simulations, which are sometimes validated through semi-integral tests that aim to reproduce most of the phenomena involved. In order to feed these simulations, models that describe the various, often complex, numerous, and coupled phenomena are required. The development of such models necessitates the availability of experimental data and a comprehensive understanding of the phenomena involved.

Most of the work I carried out at CEA between 2008 and 2018 was focused on contributing to this field [7]. The objective was to characterize, understand, and model the oxidation of zirconium alloys in steam at HT, the stresses generated in the material during the transient, and the mechanical response of the material during and after post-oxidation cooling. We have worked to study the effect of multiple factors that may play a role, for which data were lacking in the literature in the domains of interest. The following sections summarize the work carried out.

[4] This phase exhibits the typical Widmanstätten structure, which can be easily distinguished from the equiaxed $\alpha_{Zr}(O)$ one.

[5] 1200 °C for as-received materials.

[6] 17% of the thickness of the cladding consumed by oxidation for as-received materials (assuming that all the oxygen is absorbed to form stoichiometric zirconia, which is actually not the case).

[7] Most of this work was supported by CEA, AREVA/Framatome, and EDF.

1.2 Influence of the pre-transient state

Context: Under normal reactor operating conditions, the cladding experiences corrosion upon contact with primary water. A layer of zirconia growths and the material absorbs a fraction of the hydrogen generated [8]. The hydrogen content in the cladding material [9] can reach a few dozen to a few hundred weight parts per million (wppm) at the end of its life in the reactor [10], depending on the material and the conditions to which it has been exposed. The thickness of the outer oxide layer can reach several tens of micrometers after several years of exposure, depending on the alloy and exposure conditions in the reactor. An oxide layer can also form on the inner surface of the cladding due to physicochemical interaction with the fuel. According to the literature, a pre-existing oxide layer may influence the subsequent oxidation of the material under HT steam. However, results and conclusions vary between studies. This suggests that the effect of pre-oxidation depends on the alloy, HT oxidation conditions and pre-oxidation conditions. This raises the question of whether the results obtained from samples pre-oxidized in the laboratory, under conditions that differ from those in the reactor, can be considered representative of the effect of a pre-oxide formed in the reactor. Furthermore, most paper dealing with the oxidation of pre-oxidized zirconium alloys do not address the potential absorption of hydrogen by the material during HT oxidation. Nevertheless, the limited available data shows that the pre-oxide may have an effect on hydrogen absorption during HT oxidation.

Objectives: We have therefore conducted a study with the objective of enhancing the existing experimental database and knowledge on the impact of a pre-existing oxide layer on the corrosion of zirconium alloys under HT steam, as well as on the residual mechanical behavior after quenching from HT. This study was the subject of two papers, published in 2011 (Le Saux et al., 2011) and 2019 (Le Saux et al., 2019).

Methods: Two zirconium alloys, Zircaloy-4 [11] and M5 [12], were used to study the effect of the material. To examine the impact of the pre-oxidation conditions, the cladding samples were pre-oxidized under different conditions, including air at 550 °C, steam at 415 °C, static water at 340–360 °C with typical PWR primary water chemistry, and flowing water at 350 °C with typical PWR primary water thermal-hydraulic and chemical environment. Samples with pre-oxide thicknesses ranging

[8] The fraction of hydrogen absorbed is between 5% and 20% depending on the alloy and operating conditions.

[9] The hydrogen content is generally less than 5 wppm in the as-received materials.

[10] The cladding is typically used for five reactor cycles. A cycle is defined as the period of time during which a reactor operates between two fuel reloads, i.e., between one and two years for a PWR.

[11] Chemical composition: 1.3 w% Sn, 0.2 w% Fe, 0.1 w% Cr, 0.13 w% O, less than 5 wppm H, Zr balance

[12] Chemical composition: 1 w% Nb, 0.14 w% O, 0.04 w% Fe, less than 5 wppm H, Zr balance. The notation of this alloy has changed over time: M5™, M5® or $M5_{Framatome}$. It is simply noted as M5 in this document.

from 3 µm to 60 µm were tested to investigate the impact of pre-oxide thickness. Oxidation tests were carried out under flowing steam at atmospheric pressure and at several temperatures between 850 °C and 1200 °C, with holding times ranging from 55 s to 9500 s, to study the effect of the HT oxidation conditions. The hydrogen content of the samples was quantified before [13] and after oxidation at HT to assess the hydrogen uptake. Observations were conducted using optical microscopy (OM) and scanning electron microscopy (SEM) in order to measure the thickness of the oxide, $\alpha_{Zr}(O)$ and β_{Zr} layers. Electron-probe micro analysis (EPMA) was used to quantity the oxygen concentration profile across the thickness of the samples. Diametral compression tests were conducted at 20 °C and 135 °C [14] on ring samples cut from HT oxidized and quenched tube samples in order to investigate ductility after quenching.

Results: As illustrated in figure 1.2, the results showed that the presence of a pre-oxide typically delays the HT steam oxidation. The effect is more pronounced with thicker pre-oxides. It is demonstrated that at HT, the oxidation kinetics of the pre-oxidized material gradually aligns with that of the non-pre-oxidized material. Observations showed that at the beginning of oxidation at HT, the pre-oxide reduces, and then a fresh oxide grows when the oxygen flux balance at the metal-oxide interface reverses (see figure 1.3). Both processes are linked to the diffusion of oxygen through the metallic substrate. At a specific pre-oxide thickness and HT oxidation conditions, the growth rate of the new oxide at HT is dependent on the pre-oxidation conditions. In some cases, the pre-oxidized material absorbs hydrogen during oxidation under HT steam, while the non-pre-oxidized material does not. Hydrogen absorption depends on various factors, including the thickness and formation conditions of the pre-oxide layer, the type of alloy, and the oxidation conditions at HT. The percentage of hydrogen pickup can range from zero to several tens. The results therefore indicated that the mechanisms and kinetics of oxygen and hydrogen transport, as well as the locations of water dissociation and hydrogen reduction/recombination at HT, may differ depending on whether or not a pre-oxide was present.

The results of diametral compression tests showed that, although weight gains at HT were lower, the post-quench ductility of pre-oxidized samples oxidized at HT is close to that of non-pre-oxidized samples pre-hydrided to an equivalent hydrogen content and oxidized under similar conditions. Indeed, EPMA showed that the quantity of oxygen that diffuses into the metal is comparable, whether it is linked to the reduction of the pre-oxide or the growth of a new oxide. Indeed, the mechanical behavior of the material oxidized at HT is directly correlated to the amount of oxygen having diffused within the metal (excluding additional effect of hydrogen).

Conclusions: The oxidation and hydrogen pickup in steam at HT are influenced

[13] The samples absorbed more or less hydrogen during pre-oxidation, depending on the conditions.

[14] This temperature is the core stabilization temperature at the end of a large break LOCA transient.

[15] The term weight gain is used to refer to an increase in mass per unit surface area, which is a common practice in this field.

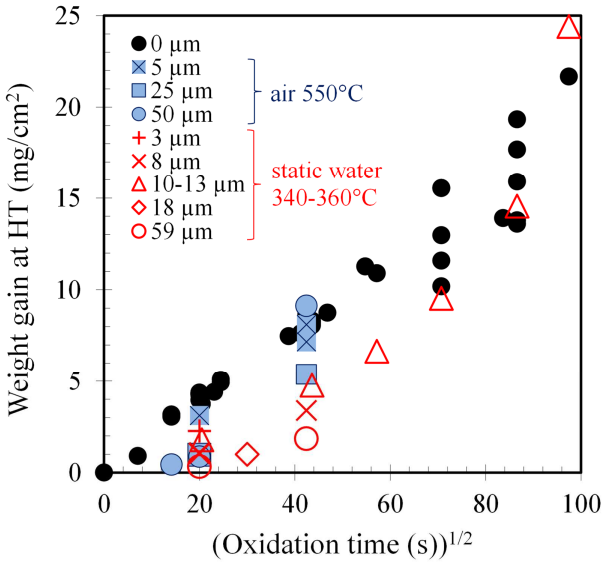

Figure 1.2 – Evolution of the weight gain [15] as a function of oxidation time under steam at 1000 °C measured for Zircaloy-4, as-received and with various pre-oxide thicknesses formed under either air at 550 °C or static water at 340–360 °C (Le Saux et al., 2019).

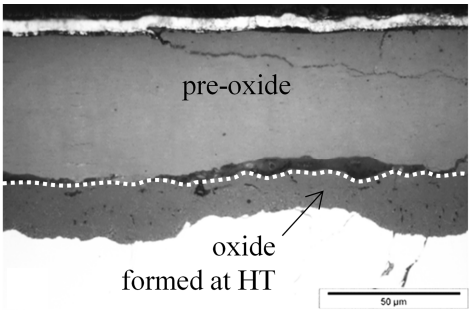

Figure 1.3 – Optical micrograph of the transverse cross-section of a Zircaloy-4 sample with a 59 µm-thick pre-oxide layer formed under static water at 360 °C, steam oxidized during 1800 s at 1000 °C (Le Saux et al., 2019).

by the presence of a pre-oxide, with the influence varying depending on the thickness of the pre-oxide and the conditions under which it was formed. It can be concluded that the results obtained on samples pre-oxidized in the laboratory cannot be extrapolated without precaution to materials pre-oxidized in the reactor. Furthermore, the pre-oxidation of the material has no significant effect on its ductility after HT oxidation and quenching, unless the pre-oxidized material absorbs more hydrogen than the non-pre-oxidized material at HT. Additional research is still required to enhance comprehension of the correlation between pre-oxide characteristics, corrosion mechanisms at HT, and their impact on oxidation and hydrogen pickup at HT. Ultimately, this will permit the prediction of the effect of a pre-transient oxide formed under real PWR conditions.

1.3 Breakaway oxidation

Context: At HT, zirconium alloys without pre-existing oxide typically exhibit parabolic or sub-parabolic oxidation kinetics. The higher the temperature, the faster the kinetics. Furthermore, the material generally does not absorb a significant amount of hydrogen. The oxide layer in these cases is dense, adherent, and protective against hydrogen absorption. However, under certain conditions, typically at temperatures between 600 °C and 1050 °C, an increase in the oxidation rate and hydrogen absorption may occur after a period of incubation. This phenomenon is commonly referred to as breakaway oxidation. The oxidation rate increases and hydrogen absorption can accelerate the deterioration of the cladding's mechanical properties due to the embrittlement effects of oxidation and hydrogen. Several factors can influence breakaway oxidation and its incubation time, including the oxidation temperature, material, fabrication process, and surface preparation. The sensitivity of breakaway oxidation is illustrated by the differences observed in the results reported in the literature. The results published in the 1980s for Zircaloy-4 alloy, which had a higher tin content than modern commercial ingots, showed that the incubation period for breakaway oxidation under steam is shortest at 1000 °C. Subsequent studies on the breakaway oxidation of zirconium alloys have mostly been conducted at this temperature. The literature reports limited data on the effect of temperature on the breakaway oxidation of contemporary zirconium alloys in steam. Furthermore, most studies use double-sided oxidation [16]. There are no real comparative studies between single-sided oxidation [17] and double-sided oxidation. In most of the papers, breakaway oxidation is determined by an increase in the oxidation rate and visual examination of the oxide. Indeed, after the breakaway oxidation transition, the outer surface of the oxide layer often changes color. However, hydrogen uptake is usually not provided. Breakaway oxidation occurs due to a loss of protection of the oxide layer during oxidation, which affects the transport of oxygen

[16] Both the inner and outer surfaces (and the ends) of the tube sample are exposed to steam.

[17] Only the outer surface (and the ends) of the tube sample is exposed to steam. The inner surface is under vacuum.

and hydrogen to the metal-oxide interface. However, the mechanisms that cause it are not well understood yet. Understanding the mechanisms behind breakaway oxidation is crucial for understanding the phenomenon and explaining its sensitivity, as well as the variability observed between laboratories.

Objectives: We conducted a study to investigate the breakaway of two "modern" zirconium alloys. We studied the sensitivity to oxidation temperature around 1000 °C, the single- or double-sided nature of oxidation, and chemical composition variation of the material. We have also investigated the mechanisms responsible for breakaway oxidation. This study was the subject of two articles, published in 2019 (Le Saux et al., 2019) and 2020 (Le Saux et al., 2020).

Methods: Single-sided and two-sided oxidation tests were conducted on Zircaloy-4 and M5 cladding samples, under flowing steam at several temperatures ranging from 950 °C to 1050 °C, with holding times between 55 s and 15000 s. Oxidation tests were also performed at 1000 °C on M5 samples with varying contents of Nb, Fe, O, S, and Hf. The hydrogen concentration of the samples was measured to quantify hydrogen uptake. OM and SEM were used to determine the thickness of the different layers in the oxidized materials. SEM with field emission gun (FEG) observations were conducted to examine the morphology of the oxide layer. EPMA was employed to investigate the spatial distribution of chemical elements within the oxide and the metal.

Figure 1.4 – Post-quenching appearance of Zircaloy-4 cladding samples two-sided oxidized in steam at 950 °C, 1000 °C and 1050 °C (Le Saux et al., 2020).

Results: The results showed that the pre-breakaway oxidation kinetics and breakaway resistance are different between the two alloys. Nevertheless, it was demonstrated that the difference in oxidation rate between Zircaloy-4 and M5 observed at 1000 °C is reduced in the presence of a pre-oxide. Pre-oxidation does not significantly modify the resistance to breakaway oxidation under steam at 1000 °C. According to visual examination (figure 1.4), weight gain measurements (figure 1.5 (a)), and hydrogen content measurements (figure 1.5 (b)), the incubation time required for breakaway oxidation is highly dependent on the oxidation temperature. For Zircaloy-4, it is shortest at 1000 °C and increases as the temperature deviates from this value. The study found that the investigated chemical composition varia-

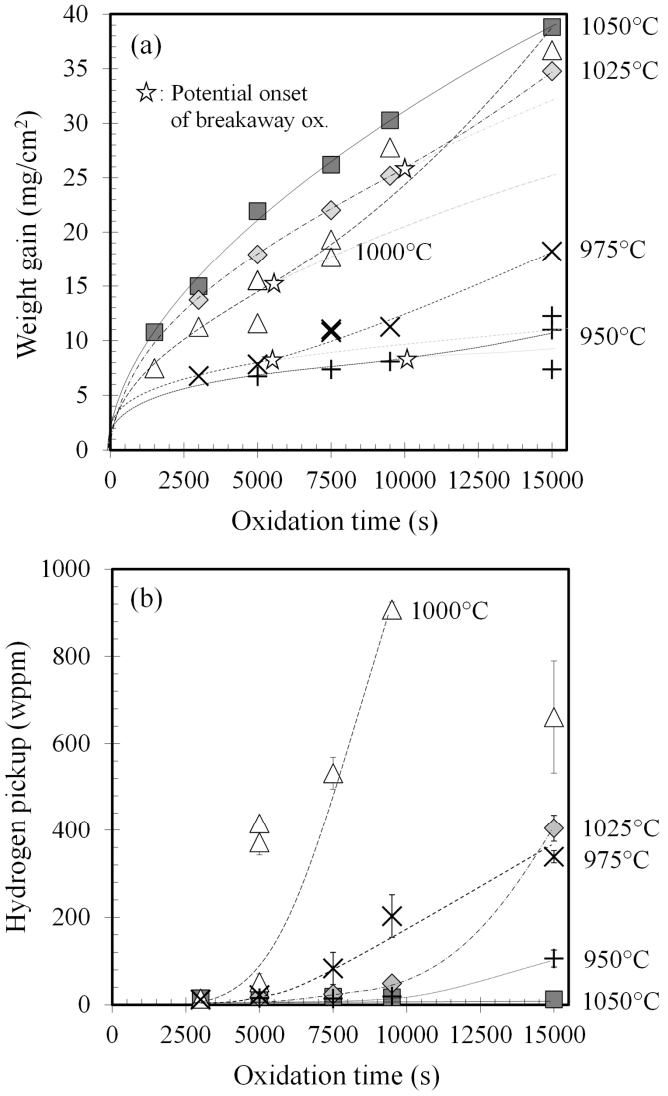

Figure 1.5 – Evolution of (a) the weight gain and (b) the hydrogen pickup as a function of the oxidation time under steam at temperatures between 950 °C and 1050 °C, for Zircaloy-4 (Le Saux et al., 2020).

tions for M5 do not significantly modify the pre-breakaway oxidation kinetics or the incubation time required for breakaway oxidation. The results showed an effect of the type of oxidation (single- or double-sided oxidation), depending on the material.

It was demonstrated that the material absorbs a large fraction of the hydrogen released during oxidation (at least 50%) at the beginning of breakaway oxidation. The fraction decreases to a few tens of percent for longer oxidation times. Observations showed that, after quenching, the post-breakaway oxide layers exhibit a higher number of cracks and micro-pores, as well as shorter and wider crystallites compared to the pre-breakaway oxide layers. As shown in figure 1.6, the metal-oxide interface displays an undulated appearance well before the breakaway oxidation stage. As illustrated in the same figure, chemical microanalysis showed microscale segregation of tin in Zircaloy-4 and niobium in M5 during oxidation at 1000 °C, with a certain continuity of the chemical modulations on either side of the metal-oxide interface and a correlation with the undulation of the metal-oxide interface.

Conclusions: To accurately determine the incubation period for breakaway oxidation, it is more reliable to consider hydrogen uptake than to rely on the color change of the oxide, the increase in oxidation rate, or the appearance of undulations at the metal-oxide interface. Breakaway oxidation is sensitive to the oxidation temperature, the material and the oxidation type. The microstructural and microchemical analyses conducted permit the formulation of a hypothesis regarding the mechanism for breakaway oxidation at around 1000 °C: the initiator of this mechanism is believed to be the local destabilization of the tetragonal phase of zirconia into the monoclinic phase [18]. However, further research is required to verify some of the assumptions and explain the differences between materials.

1.4 Influence of steam pressure

Context: Most studies on the oxidation of zirconium alloys at HT have been conducted under atmospheric pressure. However, in certain conditions (such as small and intermediate break LOCA), the steam pressure remains relatively high (several tens of bar) in the reactor primary circuit. The impact of steam pressure has been little investigated in the literature, despite some data showing that it can be significant. Furthermore, the mechanisms responsible for the steam pressure effect at HT are not yet clearly identified.

Objectives: Therefore, we investigated the effect of steam pressure on the HT oxidation of two zirconium alloys, Zircaloy-4 and M5. There were no data in the literature for M5. Our aim was to enrich the database and improve understanding of the mechanisms responsible for the effect of pressure. The sensitivity of pressure

[18] This phase transformation is likely to be heterogeneous due to microchemical partitions and/or crystallographic heterogeneities in both the metal and the oxide. The sequence of events that would result from this phase transformation includes heterogeneous oxide growth, local oxygen saturation, local oxide micro-cracking, decohesion of the metal-oxide interface, and oxide cracking. This sequence would ultimately lead to breakaway oxidation.

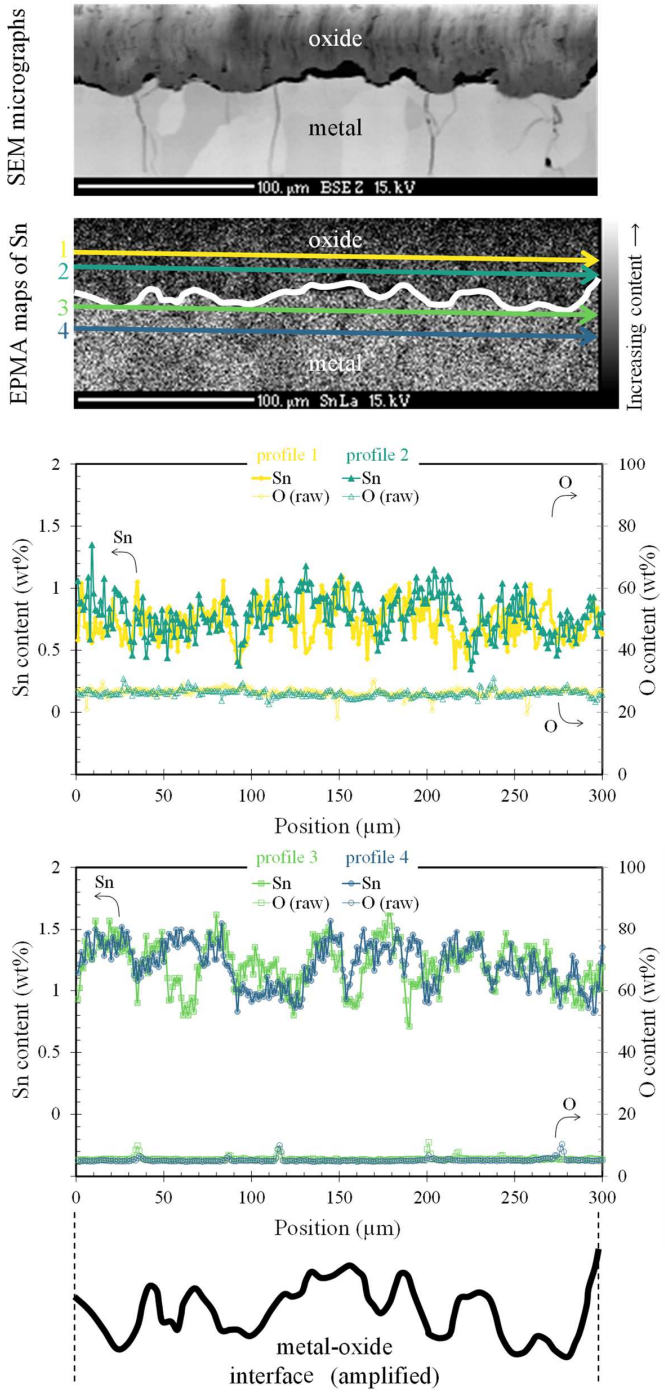

Figure 1.6 – SEM micrograph, EPMA X-ray map of tin, and tin and oxygen concentrations along the profiles numbered 1, 2, 3 and 4 in the map of tin, along the tube hoop direction, within the oxide and the metallic substrate, at a few micrometers from the metal-oxide interface, within a Zircaloy-4 sample oxidized 3270 s at 1000 °C and water-quenched (Le Saux et al., 2020).

effect was studied with respect to oxidation temperature and pre-transient state of the material. This study has been published in 2015 (Le Saux et al., 2015).

Methods: The study was conducted on as-received samples, on samples pre-charged with hydrogen up to the hydrogen content expected at the end of the life of the material in the reactor, and on samples with 3 µm to 8 µm-thick pre-oxides formed at 360 °C in water with typical PWR primary water chemistry. Oxidation tests were conducted at temperatures ranging from 750 °C to 1200 °C, for duration ranging from 200 s to 18000 s, under steam with pressures ranging from 1 bar to 80 bar. Hydrogen content measurements were conducted before and after oxidation. OM observations were carried out to measure the oxide thickness. EPMA was carried out to study the oxygen concentration profile through the thickness of the oxidized samples. Micro laser induced breakdown spectroscopy (µ-LIBS) analysis was employed to map the distribution of hydrogen within the metal matrix of selected samples. The microstructure of the oxides was studied using FEG-SEM observations. In addition, diametral ring compression tests were conducted at room temperature and 135 °C on the samples after oxidation and cooling in order to characterize the post-quench mechanical behavior.

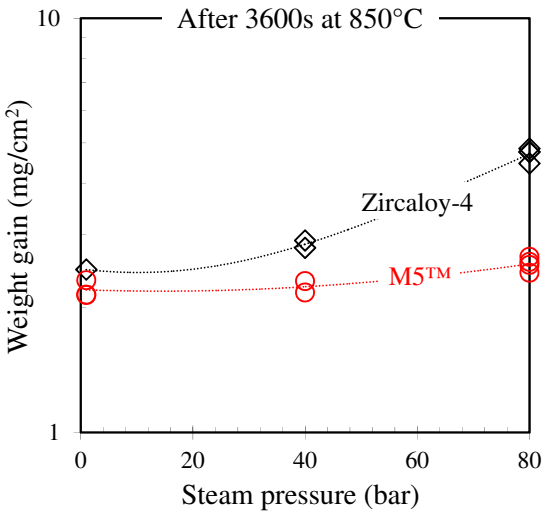

Figure 1.7 – Evolution of the weight gain of Zircaloy-4 and M5 as a function of steam pressure after 3600 s of oxidation at 850 °C (Le Saux et al., 2015).

Results: As illustrated in figure 1.7, it was demonstrated that the oxidation kinetics of Zircaloy-4 is faster under high steam pressure within the 750 °C to 1000 °C oxidation temperature range. The effect is relatively insignificant at such temperatures for M5, and at 1100 °C and 1200 °C for both alloys. The faster oxidation observed in some cases under high pressure is accompanied by significant hydrogen uptake. The effect of steam pressure is not significantly affected by pre-hydriding. The results revealed that the effect of steam pressure and the differences in sensitivity of the alloys to steam pressure are reduced by the presence of a pre-existing oxide. Observations and chemical analysis have indicated that the increased oxidation kinetics under high steam pressure are correlated with a thickening of the oxide

layers formed at HT, but not with additional oxygen diffusion through the metallic substrate. As shown in figure 1.8, it has been observed that pressure affects the microstructure of the formed oxide (e.g., morphology of the cristallites and density of pores and cracks), for conditions in which pressure has an effect on the oxidation kinetics.

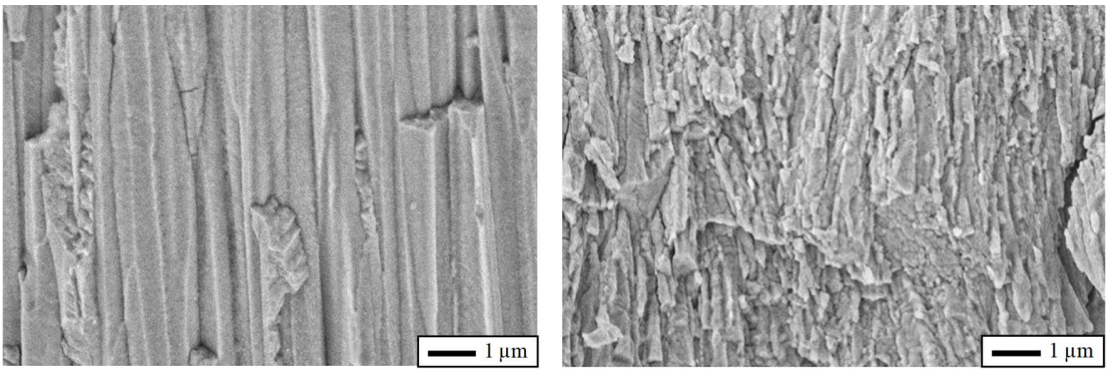

(a) 1 bar (b) 80 bar

Figure 1.8 – FEG-SEM micrographs of the fracture surfaces of the oxide formed on Zircaloy-4 after 1800 s of oxidation at 1000 °C under steam at (a) atmospheric pressure and (b) 80 bar (Le Saux et al., 2015).

The results of the compression tests showed that additional oxidation and hydrogen absorption under high steam pressure can have a significant effect on the mechanical properties of the cladding sample. However, the impact remains limited. In specific cases, a particular failure mode was observed. It is related to the presence of a continuous network of prior-β_{Zr} phase, where the hydrogen is concentrated.

Conclusions: The oxidation kinetics and the hydrogen pickup are dependent on steam pressure, to varying degrees depending on the material, the presence of a pre-oxide, or the oxidation temperature. The effect on post-quench ductility remains limited in all cases. The results have been used to assess the impact of steam pressure during representative in-reactor LOCA transients. It was concluded that the impact is very low or negligible and has no significant consequence on LOCA cladding acceptance criteria. Our observations and analysis of the literature have led us to hypothesize that the effect of pressure is linked to a destabilization of tetragonal zirconia into monoclinic zirconia which is favored when steam pressure increases. However, to improve the understanding of the effect of steam pressure and its dependence on the alloy, further investigation is still needed.

1.5 Structural evolutions in the oxide

Context: As discussed in the previous sections, the behavior of the cladding material during a LOCA is closely related to the structural changes that occur in the

oxide and the metal during the transient. For instance, it can be assumed that these changes play a role in the phenomenon of breakaway oxidation (section 1.3) or in the effect of steam pressure (section 1.4). To properly understand the cladding behavior, it is therefore necessary to have a good knowledge of these structural evolutions. The zirconia formed under the conditions of interest has a very different structure to that expected for pure zirconia at equilibrium. However, to date, the evolutions occurring in the oxide have been poorly quantified under the conditions of interest for LOCA, i.e., for oxidation temperatures exceeding 700 °C. X-ray diffraction (XRD) seems to be an appropriate methodology for studying such structural evolutions. XRD studies reported in the literature on the oxidation of zirconium alloys have been conducted primarily on samples oxidized at temperatures below 500 °C, with the majority of these studies performed after the material has cooled to room temperature. The few XRD experiments performed at higher temperatures have been carried out in air. However, zirconium alloys oxidize differently in air and in steam [19].

Objectives: We have conducted a study using XRD to gain a deeper understanding of the structural changes that occur in the zirconia layer during oxidation at temperatures above 700 °C and subsequent cooling. This study has been the subject of several communications, notably in 2012 (Gosset et al., 2012), 2015 (Gosset and Le Saux, 2015), and 2019 (Guillou et al., 2019a, b).

Methods: We have set up in situ XRD analyses, during heating, oxidation and cooling. The first experiments were carried out using a conventional laboratory X-ray source (Gosset et al., 2012; Gosset and Le Saux, 2015). During these experiments, the thickness of the oxide layer that could be probed was limited to a few micrometers. Furthermore, the long measurement times did not allow for the structural changes occurring during the fast oxidation process [20] to be monitored with sufficient temporal resolution. Consequently, during R. Guillou's post-doctorate [21], we conducted new experiments, this time using X-rays generated by synchrotron light sources (Guillou et al., 2019a, b). A O_2-He gas mixture was used as the oxidizing atmosphere, serving as a surrogate for steam [22], which was excluded for use in the facilities. XRD analyses were conducted on two zirconium alloys (Zircaloy-4 and M5), in situ during heating and isothermal oxidation, and during and after step-cooling. Oxidation was conducted at temperatures between 700 °C and 1100 °C for periods ranging from 30 s to 10800 s. The depth of penetration of the X-rays was greater than the thickness of the oxides formed. Following testing, the thickness of the oxide layers was observed using FEG-SEM. The morphology and crystallographic orientation of the grains of the oxide layer were analyzed using EBSD. The distribution of chemical elements within the metallic substrate was characterized using EPMA.

[19] This is mainly due to the presence of nitrogen in air.

[20] For example, for Zircaloy-4, an oxidation of one minute at 900 °C results in the formation of a 5 µm-thick oxide layer.

[21] This post-doctorate was funded by CEA, AREVA and EDF.

[22] It was demonstrated that the oxidation kinetics at HT under steam and under an O_2-He environment are comparable.

Results: The post-test measurements have confirmed that the temperature and oxidizing atmosphere were successfully controlled throughout the experiments. The thickness of the formed oxides varied from a few micrometers to approximately fifty micrometers depending on the oxidation conditions. As illustrated in figure 1.9, the results showed that the oxide formed under the conditions studied is composed of a mixture of m_{ZrO2} and t_{ZrO2}, or only t_{ZrO2}, depending on the oxidation temperature. As shown in figure 1.10, it was demonstrated that the volume fraction of t_{ZrO2} decreases during oxidation. A portion of t_{ZrO2} formed during oxidation undergoes a transformation into m_{ZrO2} on cooling. The relative proportion of t_{ZrO2} is observed to decrease significantly upon cooling. The higher the oxidation temperature, the lower the proportion of t_{ZrO2} remaining at room temperature after cooling. Furthermore, the results indicated that the average crystal size tends to increase during oxidation and that t_{ZrO2} crystals tend to be smaller than m_{ZrO2} crystals. Accordingly, it was proposed that the evolution of the oxide structure during oxidation and cooling may be related, at least in part, to the size dependence of the critical size of crystals below which t_{ZrO2} is stabilized.

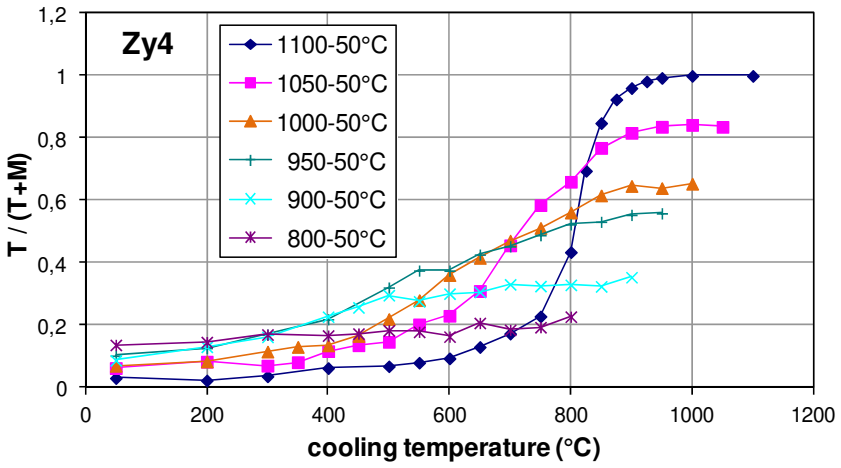

Figure 1.9 – Evolution of the volume fraction of tetragonal zirconia in the oxide formed on Zircaloy-4 as a function of temperature, determined by in situ XRD during oxidation at temperatures between 800 °C and 1100 °C (rightmost point of the curves) and subsequent cooling down to room temperature (Gosset and Le Saux, 2015).

Conclusions: The oxide formed at temperatures above 700 °C contains a mixture of m_{ZrO2} and t_{ZrO2}. The proportion and size of crystals of each phase evolve during heating, oxidation and cooling. It is not possible to determine the structure of the growing oxide from *post facto* measurements, either at room temperature or after reheating to the prior oxidation temperature, due to irreversible transformations occurring during cooling.

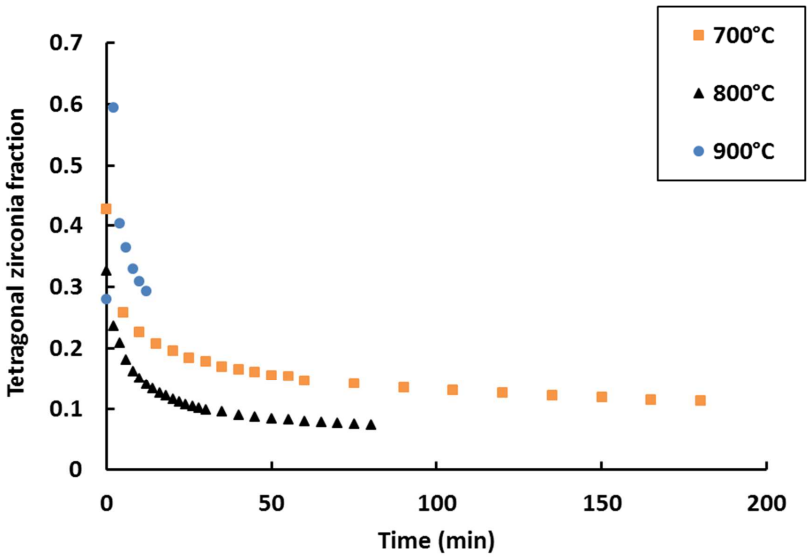

Figure 1.10 – Evolution of the volume fraction of tetragonal zirconia in the oxide formed on Zircaloy-4 as a function of oxidation time at 700 °C, 800 °C and 900 °C, determined by in situ XRD (Guillou et al., 2019b).

1.6 Stresses due to structural evolutions and changes in temperature

Context: Even in the absence of external mechanical loading, the various layers that constitute zirconium alloys oxidized at HT are subjected to stresses (at micro and macro scales) resulting from the metallurgical changes that occur during oxidation. These changes include the growth of an oxide layer, the diffusion of chemical elements through the metal, and phase changes. The stresses in the oxide are expected to have an effect on the oxide structure and the oxidation kinetics of the material. Stresses are also generated during cooling after oxidation at HT. These are due in particular to phase transformations and to differences between the thermal coefficients of the different phases/layers constituting the material oxidized at HT. These stresses can result in the failure of the material once it is heavily oxidized and hydrided. Residual stresses after cooling may finally have some consequences on the long-term evolution of the material after quenching. Therefore, the determination of these stresses is of particular interest. However, there is very little data in the existing literature on the stresses associated with oxidation at temperatures above 700 °C. Indeed, the majority of the methodologies commonly employed to assess oxidation-related stresses are ill-suited to the case under investigation or particularly challenging to implement [23].

[23] It is sometimes possible to estimate oxidation-related stresses from residual stresses measured after returning to room temperature. However, this estimation is particularly difficult in the case studied because of the complexity of the material's microstructure and the changes that occur during cooling.

Objectives: We have endeavored to develop methodologies for assessing the stresses generated in zirconium alloys during oxidation at HT and subsequent cooling. The work carried out was the subject of communications made in 2018 (Guillou et al., 2018; Le Saux et al., 2018) and 2023 (Guillou et al., 2018; Bouayoune et al., 2023).

Methods: We have implemented two different but complementary approaches. The first one has been developed during R. Guillou's post-doctorate. It consists of estimating the stresses in the oxide through the use of synchrotron XRD measurements, conducted in situ during heating, oxidation, and cooling (Guillou et al., 2018; Bouayoune et al., 2023). Oxidation was carried out on Zircaloy-4 samples, under a O_2-He gas mixture, for 10800 s at 700 °C, 4500 s at 800 °C, and 600 s at 900 °C. The oxides formed have a thickness of approximately ten micrometers. The X-ray penetration depth was about 20 µm, i.e., larger than oxide thickness. The $\sin^2\psi$ method was used to estimate the stresses in the oxide in directions perpendicular to the direction of oxide growth (in-plane stresses).

In the second approach, the stresses within the various layers of the oxidized material were studied through the combination of two methods (Le Saux et al., 2018). First, the macroscopic deformation of cladding samples was measured in situ during oxidation at HT and subsequent cooling. Second, finite element (FE) simulations [24] of the multiphase and multilayered oxidized material were implemented. The model was used to perform parametric calculations and determine the factors that have a first order effect on oxidation-related stresses. The experiments were conducted using a modified quenching dilatometer. Oxidation was conducted under a mixture of O_2 and He. The samples were maintained at 1100 °C for a period of 520 s, which resulted in the formation of oxide layers with a thickness of approximately 50 µm on all sample surfaces. In order to quantify the strains induced by oxidation, samples were subjected to the same thermal cycles but using an inert gas in order to establish a baseline without significant oxidation. The FE model takes into account the evolution of the material during oxidation at HT and subsequent cooling, as well as the associated strains. This includes oxide growth, diffusion of oxygen through the metal substrate and β_{Zr} to $\alpha_{Zr}(O)$ phase transformation during oxidation, and β_{Zr} to prior-β_{Zr} and t_{ZrO2} to m_{ZrO2} phase transformations during cooling. The oxide growth and the diffusion of oxygen were modeled by an oxygen concentration field that evolves over time, according to the kinetic data discussed in section 1.4. The temperature range over which the t_{ZrO2} to m_{ZrO2} transformation occurs was defined on the basis of the results presented in section 1.5. Furthermore, the model considered the thermomechanical properties of the different phases and their evolution as a function of temperature and oxygen content. The behavior laws have been numerically implemented [25] so that they can be used for the FE simulations.

Results: The results of the first approach are illustrated in figure 1.11. They show that during oxidation, both t_{ZrO2} and m_{ZrO2} phases are subjected to compressive in-plane stresses on average. Nevertheless, the compressive stresses are different

[24] These simulations were conducted using the `Cast3M` code: `https://www-cast3m.cea.fr/`.

[25] The implementation was carried out by defining a `UMAT` subroutine.

in the two zirconia phases. Furthermore, it was demonstrated that the stresses depend on the oxidation temperature. The stress levels obtained are considerably lower than those reported in the literature for oxidations conducted at lower temperatures. In addition, it was observed that the in-plane stresses in the zirconia phases significantly decrease during cooling. Finally, it was shown that the residual stresses at room temperature depend on the oxidation temperature.

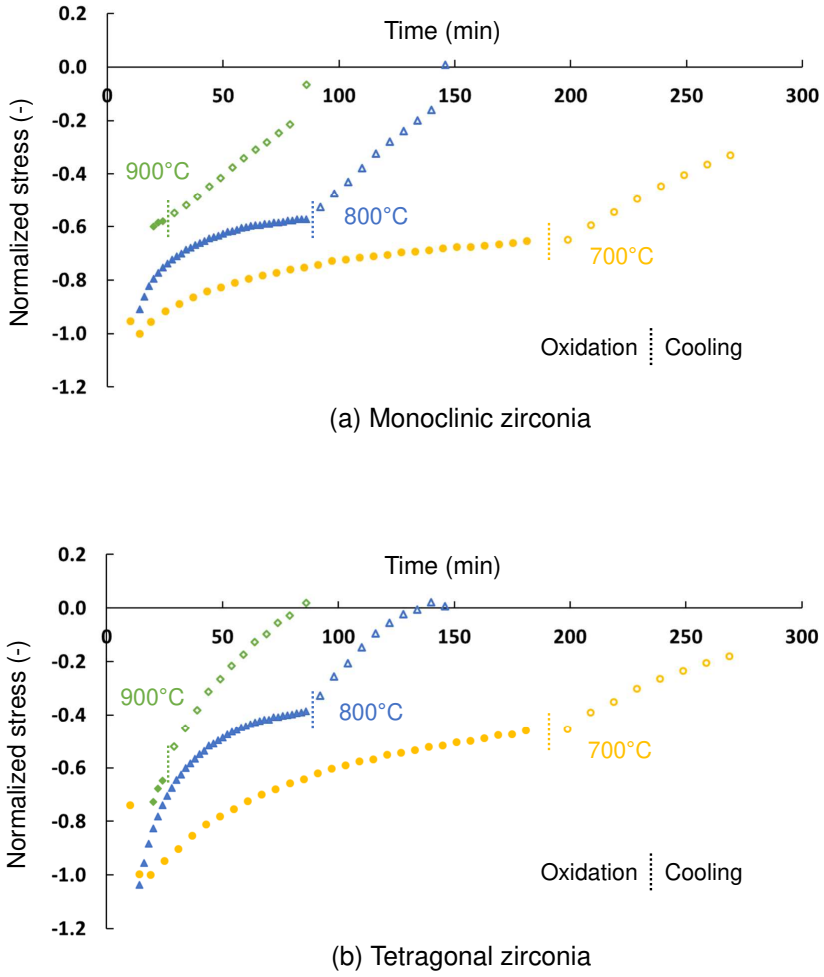

Figure 1.11 – Normalized average in-plane stress as a function of the oxidation time determined through in situ XRD in (a) the m_{ZrO2} phase and (b) the t_{ZrO2} phase of the oxide, during oxidation of Zircaloy-4 at 700 °C, 800 °C and 900 °C, and cooling (Guillou et al., 2018; Bouayoune et al., 2023).

As illustrated in figure 1.12, the results of the second approach showed that the sample deforms significantly during oxidation and cooling. These measurements provided insight into the material's evolution during the transient. The results of the FE simulations indicated that the diffusion of oxygen within the metallic substrate and the viscoplasticity of the phases constituting the material, which are enhanced at HT, have a significant impact on the stresses generated during oxidation. The

results also suggested that the cooling rate may influence the stresses, that the stresses may be different in the oxide layers on the inner and outer periphery of the cladding, and that the $\alpha_{Zr}(O)$ phase layer probably cracks during cooling from HT. The parametric study has demonstrated that the factors that have a primary influence on the deformation of the sample and the stresses in the material during oxidation and cooling include the mechanical properties of zirconia and the strains induced by the t_{ZrO2} to m_{ZrO2} phase transformation (see figure 1.13). Discrepancies between simulation and experimental results confirmed the need for further investigation. In particular, more data is needed to challenge some model assumptions and material properties.

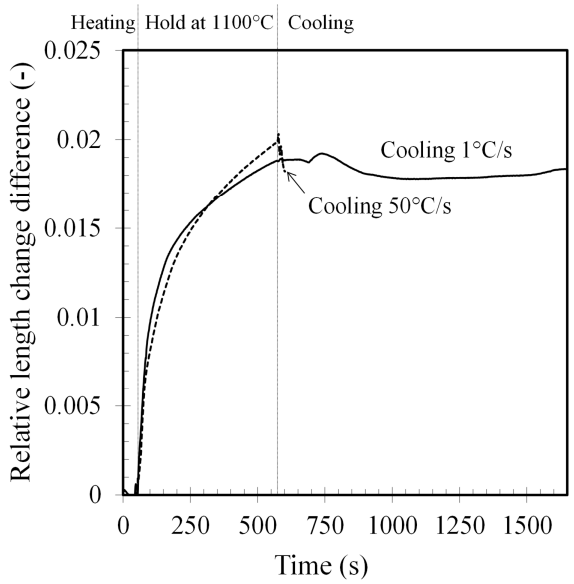

Figure 1.12 – Evolution, as a function of time, of the difference between the engineering strains measured in situ on Zircaloy-4 samples held for 520 s at 1100 °C under oxidizing atmosphere and under inert gas, after heating at 20 °C/s and before cooling at 1 °C/s or 50 °C/s under an inert atmosphere (Le Saux et al., 2018).

Conclusions: The value of conducting in situ measurement, during oxidation and cooling, to assess the stresses generated is clearly demonstrated. Analyses based on measurements made after the material has returned to room temperature must therefore be conducted with great caution. The stresses generated during oxidation at HT are very different from those reported for lower temperatures. They evolve significantly during the oxidation and cooling processes. These stresses are strongly related to the mechanical properties of zirconia and to the strains induced by the phase transformation in zirconia.

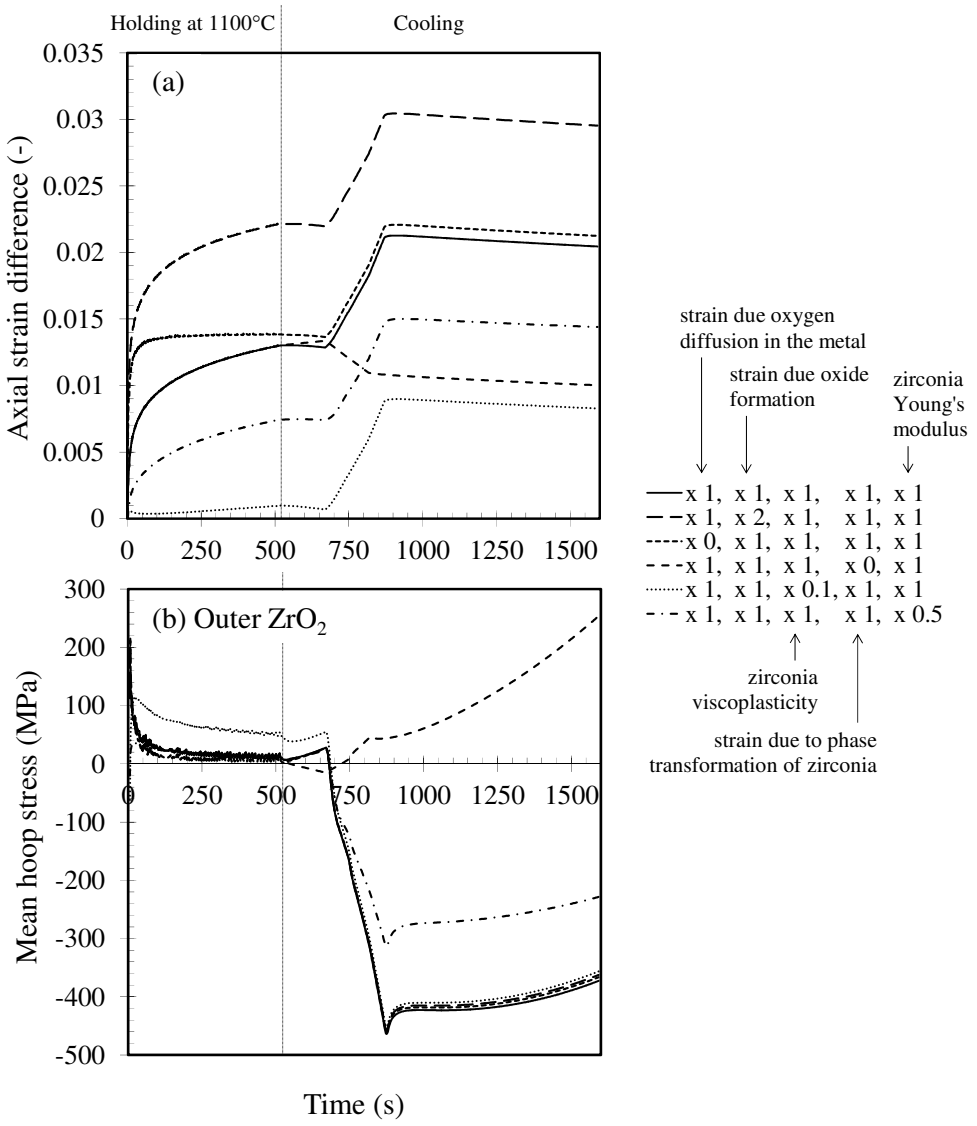

Figure 1.13 – (a) Difference between engineering axial strains calculated by FE simulations with and without oxidation and (b) mean hoop stress calculated in the outer zirconia layer, for different parameter values, for Zircaloy-4 oxidized 520 s at 1100 °C and cooled at 1 °C/s to room temperature (Le Saux et al., 2018).

1.7 Secondary hydriding

Context: During the first moments of the LOCA transient, the cladding heats up and is subjected to internal pressure, which can cause it to balloon and burst. So-called semi-integral tests, which reproduce the sequence of heating, ballooning and bursting, oxidation and cooling, followed by quenching, have shown rapid and massive hydrogen uptake of the cladding after only a few tens of seconds of exposure to steam at HT. This phenomenon called secondary hydriding occurs when steam enters the gap between the nuclear fuel pellets and the cladding inner surface through the burst opening [26]. The distribution of hydrogen and oxygen in the cladding is not homogeneous a priori. As discussed in the following sections, the material is embrittled by hydrogen and oxygen, which increases the risk of cladding failure during cooling. Therefore, quantitatively characterizing the concentration and spatial distribution of hydrogen and oxygen in the cladding is particularly useful. Performing this type of measurement is challenging, especially for hydrogen [27]. The hydrogen concentration is typically measured using a destructive, inert gas fusion thermal conductivity technique, on small rings extracted from various axial positions. These measurements provide average values and do not provide information on azimuthal or radial gradients. More recently, neutron radiography has been utilized to obtain semi-quantitative maps of hydrogen concentration. This technique highlights azimuthal and axial gradients of the hydrogen content. However, the resolution is insufficient to quantify the distribution of hydrogen throughout the thickness of the cladding, i.e., between the different phases/layers.

Objectives: We have therefore conducted a study to gain further insights into the secondary hydriding phenomenon. Specifically, our objectives were to produce secondary hydriding in cladding samples, to quantify the spatial distribution of hydrogen and oxygen at different scales, and then to examine the effects on the hardness the prior-β_{Zr} layer. This work was published in 2017 (Brachet et al., 2017).

Methods: Cladding tube samples in M5 with an internal alumina rod (to simulate the presence of fuel pellets) were subjected to a two-stage treatment, carried out in two installations, to produce secondary hydriding: a first stage of ballooning and bursting under the effect of an increase in temperature and internal pressure; a second stage of oxidation under steam at HT (1100–1200 °C), followed by quenching with water at room temperature. The thickness of the different layers in the oxidized material (inner and outer oxide, $\alpha_{Zr}(O)$, and prior-β_{Zr}) was measured through OM and SEM observations. The spatial distribution of oxygen in the material was quantified by EPMA with a spatial resolution of 1 µm. Neutron radiography and tomography was used to non-destructively map the hydrogen content over a large

[26] In the gap between the pellet and the cladding, the oxidation of the cladding results in enrichment of the steam in hydrogen gas. The ratio between the partial pressure of hydrogen and that of steam increases when moving away from the burst zone, until it reaches a critical value at which the hydrogen can be absorbed rapidly and in large quantities by the cladding, according to Sievert's law.

[27] Even if hydrogen was precipitated in the form of zirconium hydrides, these hydrides are not easily visible through optical or electron microscopy in the material cooled rapidly from HT.

part of the sample with a spatial resolution (pixel or voxel side length) of 25 µm. µ-ERDA and µ-LIBS [28] made it possible to quantitatively map the hydrogen concentration (in smaller zones) with a finer spatial resolution of 2–3 µm. Micro-hardness measurements were carried out to investigate the impact of secondary hydriding on the local mechanical response of the material.

Results: The results showed that internal oxidation is very heterogeneous and depends in particular on the distance from the burst. The hydrogen is distributed heterogeneously along the axis of the tube (figure 1.14), and along its circumference (figure 1.15). Furthermore, as shown in figure 1.15, it was evidenced that hydrogen is concentrated in the prior-β_{Zr} layer, where the hydrogen content reaches the very high value of 3000–4000 wppm (20–25 atomic percent, at%). Oxygen is also distributed heterogeneously. The oxygen content in the prior-β_{Zr} layer reaches the very high value of 10000–12000 wppm [29] (5–6 at%). The study found that oxygen diffusion in the prior-β_{Zr} layer is accentuated in regions highly enriched in hydrogen, in accordance with thermodynamic and kinetic considerations. The measurements indicated that more than 50% of the amount of gaseous hydrogen resulting from the HT oxidation of the cladding inner surface is absorbed by the material. Finally, it has been observed that oxygen and hydrogen uptake results in the local hardening of the prior-β_{Zr} material.

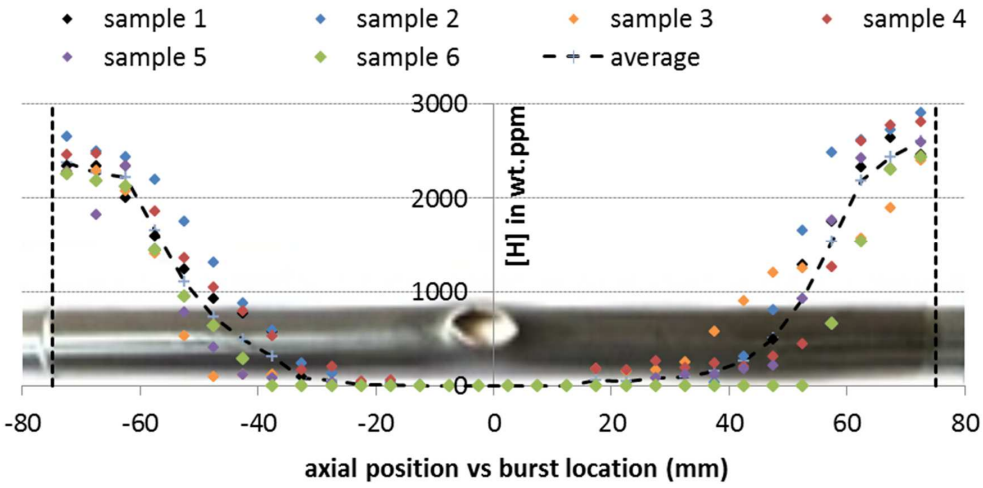

Figure 1.14 – Profiles, obtained using neutron radiography, of the azimuthal mean hydrogen concentration (in wppm) along the axis of M5 tube samples that were burst, oxidized 160 s under steam at 1200 °C and quenched (Brachet et al., 2017).

Conclusions: The use of advanced techniques permitted the demonstration that internal oxidation and secondary hydriding of the cladding under steam at HT following burst can result in significant gradients of hydrogen and oxygen concen-

[28] Unlike µ-ERDA, µ-LIBS requires calibration to provide quantitative measurements.

[29] The solubility limit of oxygen in the β_{Zr} phase at temperatures between 1100 °C and 1200 °C is less than 5000–6000 w% in the absence of hydrogen.

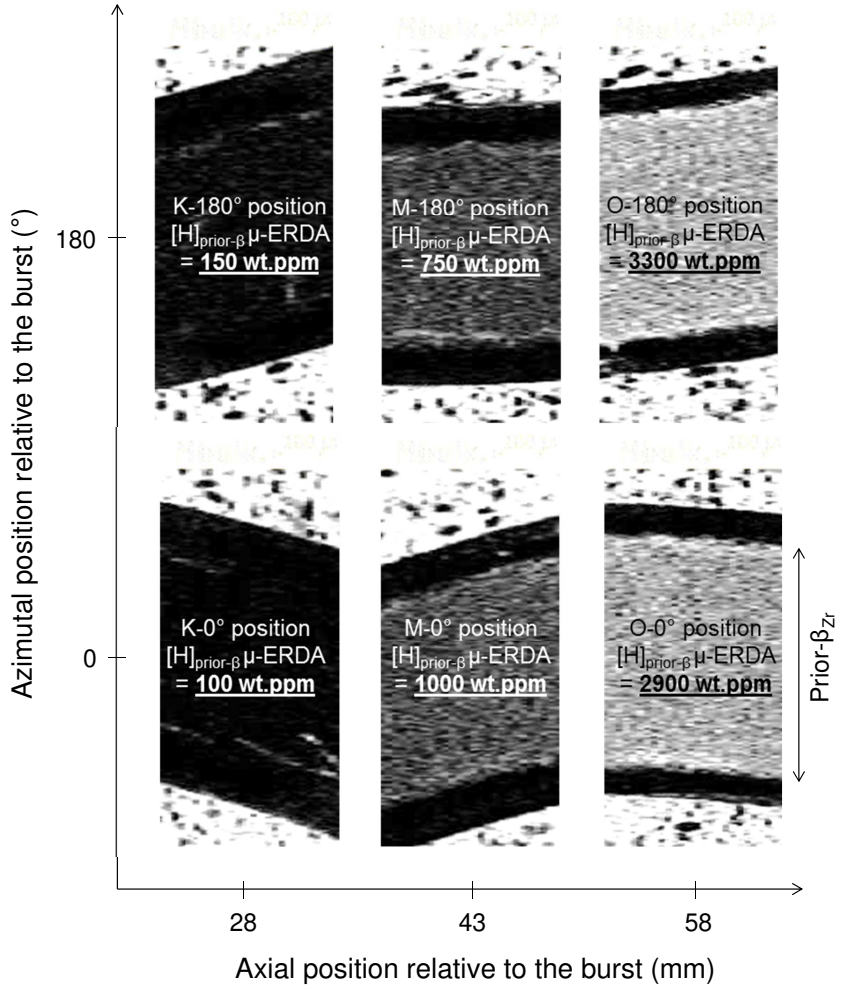

Figure 1.15 – Hydrogen content maps (the lighter the color, the higher the hydrogen content) obtained using µ-ERDA in sections perpendicular to the axis of a M5 tube sample that has been burst, oxidized under steam at 1200 °C for 160 s and quenched, at three axial positions relative to the burst and two azimuthal positions; the average hydrogen content in the section is given on each map in wppm (Brachet et al., 2017).

trations at different scales. These concentrations can reach very high levels locally, well above average spatial values.

1.8 Post-quench mechanical response

Context: The diametral ring compression test is the historical reference test widely used in LOCA-related studies to evaluate the residual ductility of the cladding after oxidation at HT and quenching. However, the load-displacement curves obtained have a complex evolution, mainly due to the presence of different layers that constitute the material, with very different mechanical behaviors. These curves are open to different interpretations, which makes it difficult to compare one study with another and can lead to different conclusions.

Objectives: As part of A. Cabrera's PhD thesis [30] (Cabrera, 2012), we carried out investigations to establish the failure scenario of oxidized and quenched cladding samples during the diametral compression test, and thus support the interpretation of the load-displacement curves. A portion of this work has been presented in 2010 (Cabrera et al., 2010).

Methods: To this end, Zircaloy-4 and M5 cladding samples were oxidized on their oxide surface under steam (at atmospheric pressure) at 1100 °C and 1200 °C and quenched in water at room temperature. The stresses resulting from quenching after HT oxidation were assessed using semi-analytical calculations and neutron diffraction analysis. Subsequently, interrupted compression tests were conducted at room temperature on oxidized and quenched samples. Additionally, compression tests were performed on a single-phase prior-β_{Zr} material. Comprehensive observations of the distinct layers in the material oxidized at HT were made using OM and SEM.

Furthermore, tensile tests were conducted at various temperatures between −150 °C and 135 °C on samples of prior-β_{Zr} material charged with oxygen up to about 5000 wppm [31] and hydrogen up to about 400 wppm. Indeed, it was anticipated that the post-quenching ductility of the material oxidized at HT mainly depends on the mechanical response of the prior-β_{Zr} layer. This response is expected to be influenced by the loading temperature and the concentration of oxygen and hydrogen in the material [32]. On the basis of the results obtained, a finite element (FE) model of the ring compression test was developed, taking into account the different layers in the material and their respective mechanical behavior, in order to inform the establishment of a failure scenario for the samples during the diametral compression tests (figure 1.16).

[30] This thesis was defended in 2012. It was funded by CEA, AREVA and EDF. In 2012, A. Cabrera won the Jean Bourgeois prize awarded by SFEN for a PhD thesis on a subject relating to nuclear energy and having implications for the safety of nuclear installations.

[31] The oxygen content is approximately 1400 wppm in the as-received material.

[32] The concentration of oxygen and hydrogen in the prior-β_{Zr} layer is contingent upon the concentration in the material before HT oxidation and the oxidation conditions at HT.

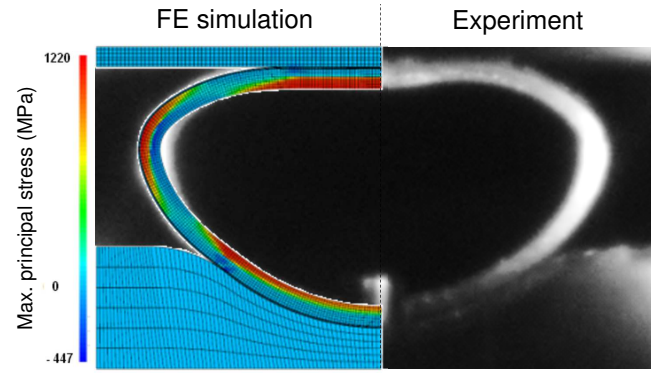

(a)

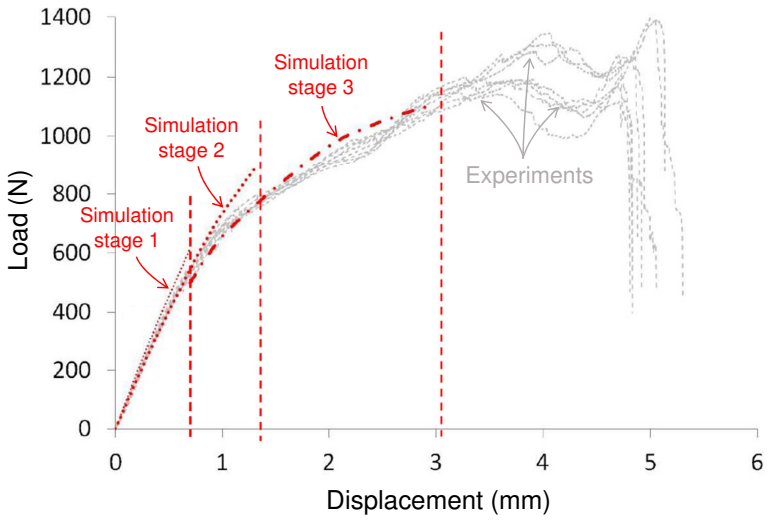

(b)

Figure 1.16 – Diametral compression on Zircaloy-4 claddings oxidized from their outer surface during 467 s at 1100 °C and water-quenched: (a) view of the ring sample (perpendicular to its axis) during an experiment (left) and deformed mesh of the FE model (right), for a displacement of 4 mm; (b) load-displacement curves measured experimentally and calculated from the FE model considering that all the layers are undamaged (stage 1), zirconia at the poles of the circular section no longer contributes to the response (stage 2) and zirconia no longer contributes at all (stage 3) (Cabrera et al., 2010; Cabrera, 2012).

Results: It was observed that the prior-β_{Zr} layer has a pronounced texture, yet its mechanical behavior remains globally isotropic. This mechanical behavior depends on the oxygen and hydrogen content and the loading temperature. It may be ductile or brittle. The results enabled the formulation of a law describing the mechanical behavior of the prior-β_{Zr} phase as a function of oxygen and hydrogen contents and temperature. The α_{Zr}(O) layer shows a very pronounced texture and an oxygen content gradient across its thickness, resulting in a gradient of mechanical properties. It is brittle at low temperature. According to the results, after quenching, the α_{Zr}(O) layer would be subjected to residual tensile stresses and the zirconia layer to compressive stresses in directions perpendicular to the oxide growth direction. The results suggested that the α_{Zr}(O) cracks during water quenching after oxidation, under the effect of the thermal stresses generated (as also suggested by the study presented in section 1.6). It was demonstrated that the cladding tube sample oxidized on its outer surface undergoes three main stages of damage during the diametral compression test: spalling of the oxide layer at the outer generatrices of the tube sample, initially at the top and bottom poles and subsequently at the left and right sides, and finally rupture of the prior-β_{Zr} layer. The post-quench ductility of the oxidized cladding is thus determined by the ductility of the prior-β_{Zr} phase.

Conclusions: As illustrated in figure 1.16, the combination of experimental and simulation results has made it possible to establish a failure scenario for the various layers of the material during the diametral compression test. The results provide guidance on how to analyze the load-displacement curves obtained from diametral compression tests on claddings oxidized at HT.

1.9 Influence of the cooling scenario

Context: During a LOCA, after being subjected to HT steam for a period of time, the cladding is cooled at a moderate rate of 1–10 °C/s typically, down to a "rewetting" temperature, which can drop to around 400 °C/s, from which it is finally quenched very quickly with the water injected by the emergency core cooling system. The cooling scenario varies depending on the transient. Furthermore, the cooling conditions applied in the tests carried out to examine the residual mechanical behavior of the cladding after oxidation at HT are not always the same from one paper to another. There is little data in the literature on the effect of the cooling scenario.

Objectives: Therefore, we conducted a study, presented in 2010 (Vandenberghe et al., 2010), to examine the effect of the cooling scenario on the residual mechanical behavior of zirconium alloy claddings after oxidation under steam at HT and quenching. The influence of material pre-hydriding on this effect was also investigated.

Methods: The study was carried out on cladding samples from two materials, Zircaloy-4 and M5, in their as-received state, or pre-hydrided up to the hydrogen content levels expected at the end of the life of the material in the reactor. The

samples were oxidized under steam at 1000 °C or 1200 °C, then cooled to temperatures between 1050 °C and 20 °C at various rates ranging from a few tenths of a °C/s to 10 °C/s, and finally quenched in water at room temperature. The oxidized and quenched samples were then tested in diametral compression and 3-point bending at 20 °C and 135 °C. In order to interpret the results, we made SEM observations of the fracture surfaces of selected samples, and carried out EPMA and micro elastic recoil detection analysis (µ-ERDA).

Results: As illustrated in figure 1.17, the results showed that for the same duration of the isothermal oxidation stage, the cooling prior to quenching can have a negligible, beneficial or detrimental effect on the post-quench ductility, depending on the HT oxidation conditions, the cooling rate and temperature from which quenching is performed, the alloy or the initial hydrogen content of the material. Indeed, cooling before quenching can have two opposing effects on the cladding post-quench ductility: on the one hand, an effect of the additional anisothermal oxidation accumulated during cooling [33], which tends to be detrimental; on the other hand, an "intrinsic" effect (i.e., excluding additional oxidation) of cooling, which tends to be beneficial. It was observed the effect of the cooling scenario is more marked when the level of oxidation at HT is relatively low, i.e., when the "continuous" prior-β_{Zr} layer remains relatively thick and when the material is significantly pre-hydrided. Indeed, this work showed that the effect of the scenario on the post-quench ductility of the cladding is largely related to its effect on the thickness and the microstructure of the prior-β_{Zr} layer [34]. In particular, the metallurgical analyses illustrated in figure 1.17 (on the right) showed a redistribution of chemical elements (oxygen and hydrogen in particular) in the prior-β_{Zr} layer during the β_{Zr} to α_{Zr} phase transformation that takes place during cooling. This transformation occurs at different temperature ranges depending on the alloy and the average concentrations of oxygen and hydrogen (see section 1.10). The micro-chemical redistribution is more or less pronounced depending on the cooling rate.

Conclusions: The cooling scenario has an effect on the ductility of the cladding after HT oxidation and quenching, with the effect varying depending on the material, its initial hydrogen content, and the oxidation conditions at HT. This effect may explain the differences that are sometimes observed between the studies presented in the literature.

1.10 Effects of high hydrogen and oxygen contents

Context: As already mentioned, at the end of the LOCA transient, the mechanical strength and ductility of the cladding are primarily determined by the mechanical

[33] Oxidation continues during cooling, resulting in a total level of oxidation accumulated during the test that may be significantly greater than that reached at the end of the isothermal holding when cooling is slow.

[34] The zirconia and α_{Zr}(O) layers are brittle at low temperatures.

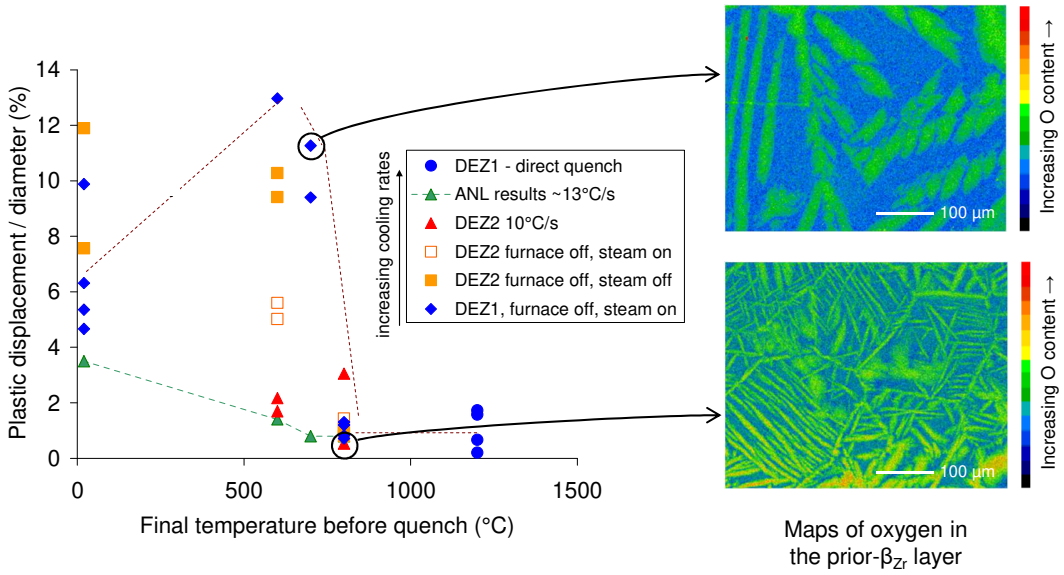

Figure 1.17 – Evolution of the plastic displacement at failure in relation to the initial sample diameter measured during diametral compression tests performed at 135 °C, as a function of the temperature before quenching after steam oxidation at 1200 °C for 60 s on Zircaloy-4 samples pre-hydrided at 600 wppm, for different cooling rates before quenching (left); EPMA X-ray maps of oxygen in two samples quenched from 800 °C after cooling at different rates (right) (Vandenberghe et al., 2010).

properties of the residual prior-β_{Zr} layer. The mechanical behavior of the prior-β_{Zr} material is primarily influenced by its oxygen and hydrogen contents, and the structural and metallurgical evolutions that occur during cooling from HT. The majority of data reported in the literature on the mechanical properties of the (prior-)β_{Zr} phase have been obtained on materials that are enriched either in hydrogen or in oxygen. However, hydrogen and oxygen are likely to have combined effects. Furthermore, these data often concern hydrogen and oxygen contents that are lower than the very high contents encountered in the case of secondary hydriding during a LOCA (see section 1.7). In addition, these data were mostly obtained at low temperatures, while a significant effect of temperature is expected. Furthermore, the microstructural and microchemical evolutions that occur during cooling from HT for high hydrogen contents are undoubtedly quite different from those observed for lower hydrogen contents. This is due in particular to the occurrence of a eutectoid reaction, which is expected to occur at approximately 550 °C.

Objectives: During the PhD theses of I. Turque[35] (Turque, 2016) and T. Le Hong[36] (Le Hong, 2020), we have studied the effects of high contents of hydrogen and/or oxygen on the mechanical behavior of the (prior-)β_{Zr} material as a function of temperature upon cooling from the β_{Zr} phase temperature stability domain. This work has been the subject of papers published in 2018 (Turque et al., 2018), 2020

[35]This thesis was defended in 2016. It was funded by CEA, AREVA and EDF.
[36]This thesis was defended in 2020. It was funded by CEA, AREVA and EDF.

(Le Hong et al., 2020) and 2021 (Le Hong et al., 2021).

Methods: A protocol was developed to homogeneously charge samples of Zircaloy-4 and M5 cladding tubes with hydrogen up to around 3000 wppm, and oxygen up to 9000 wppm. Tensile tests were then performed at various temperatures between 700 °C and 30 °C upon cooling from the β_{Zr} domain (1000–1200 °C) on samples with different hydrogen and oxygen contents. In order to establish a link between the macroscopic mechanical response and the microstructure of the material, we observed the fracture surfaces of certain samples using SEM, and carried out EPMA and µ-ERDA. A tensile test was also carried out in situ under SEM at room temperature, with digital image correlation (DIC) to measure the strain fields.

In order to interpret the results, we conducted a study of the metallurgical evolutions (phase transformations, changes in chemical composition and lattice parameters of the phases) occurring on cooling from the β_{Zr} domain in the two alloys charged with hydrogen up to very high contents. Furthermore, unalloyed zirconium has been charged in hydrogen to isolate the effect of hydrogen and avoid the influence of alloying elements. Several techniques have been used to investigate the metallurgical transformations, including differential scanning calorimetry (DSC), in situ neutron diffraction during cooling from 700 °C (under secondary vacuum), and neutron diffraction, XRD, EPMA, µ-ERDA and electron backscatter diffraction (EBSD) at room temperature after cooling. The study investigated the effects of alloy composition, average hydrogen content, and cooling scenario.

Results: As shown in figures 1.18 and 1.19, the results demonstrated that the mechanical behavior is strongly influenced by the test temperature and the hydrogen and oxygen contents. High contents of hydrogen and oxygen have an embrittlement effect that depends on temperature (figure 1.18). A macroscopic ductile-to-brittle transition has been identified as a function of hydrogen content, oxygen content and temperature. The transition temperature increases continuously with an increase in the hydrogen and oxygen contents, with an apparent additive effect of these two chemical elements. Based on the experimental results obtained, we have proposed a series of relationships to describe the macroscopic mechanical behavior of the material as a function of hydrogen and oxygen contents and temperature. These relationships include the ductile-to-brittle transition, elasticity, plasticity in the case of ductile failure (see figure 1.19), and failure stress in the case of brittle failure. As shown in figure 1.20, a heterogeneity in deformation and fracture mode was observed on a local scale. This heterogeneity is related to microchemical heterogeneities, of oxygen and hydrogen in particular (see figure 1.21).

The results of metallurgical investigations illustrated in figure 1.22 indicated that, during slow cooling, β_{Zr} undergoes a progressive transformation into α_{Zr}, followed by an extensive transformation into α_{Zr} and precipitation of $\delta_{ZrH2\text{-}x}$ hydrides via a eutectoid reaction. The thermodynamic predictions at equilibrium, which had not yet been validated experimentally for the studied high hydrogen contents, are in good agreement with the experimental results. However, according to the experimental results, depending on the cooling scenario and the average hydrogen content, the precipitation of metastable γ_{ZrH} hydrides was evidenced below 350 °C. Furthermore,

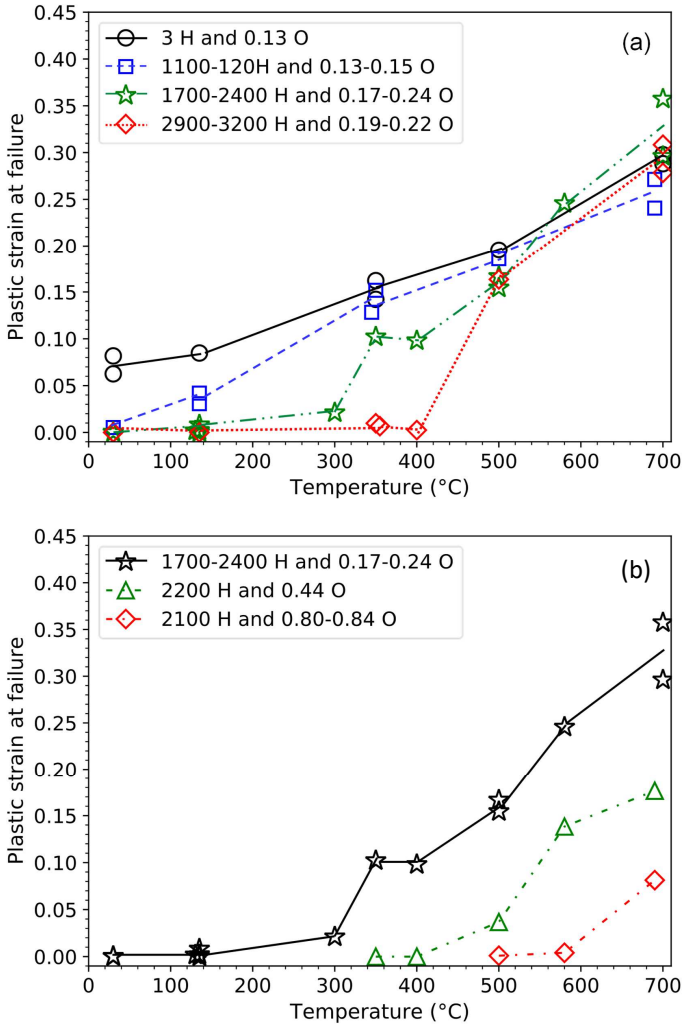

Figure 1.18 – Macroscopic plastic strain at failure as a function of test temperature obtained from tensile tests on prior-β_{Zr} samples containing (a) about 2000 wppm of oxygen and different hydrogen contents (in wppm), and (b) about 2000 wppm of hydrogen and different oxygen contents (in weight percent) (Le Hong et al., 2021).

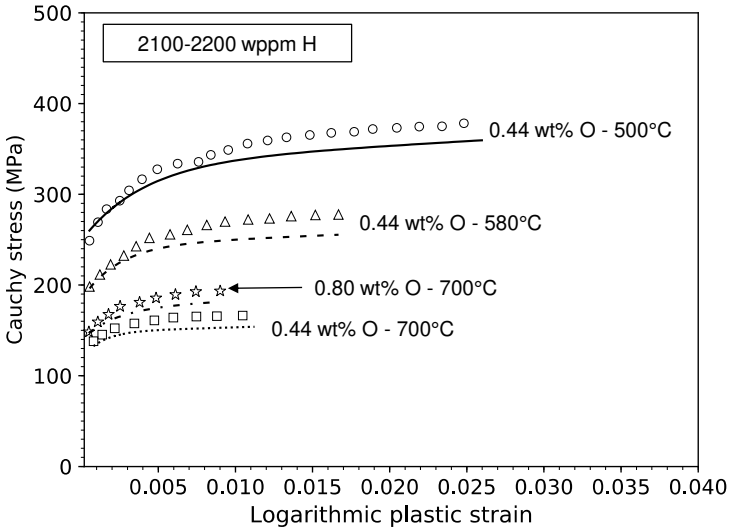

Figure 1.19 – Stress-plastic strain curves (up to the experimental uniform elongation) obtained for uniaxial tension at 500 °C, 580 °C, or 700 °C on the (prior-)β_{Zr} material containing 2100–2200 wppm of hydrogen and 4400 wppm or 8000 wppm of oxygen; comparison of curves obtained experimentally (symbols) and calculated (lines) (Le Hong et al., 2021).

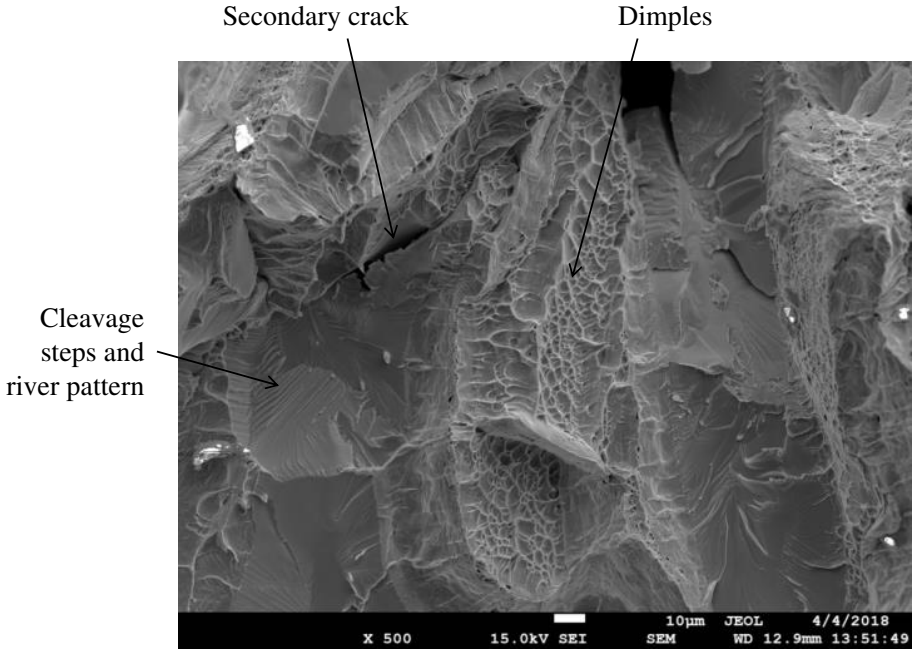

Figure 1.20 – Fracture surface observed by SEM of a Zircaloy-4 sample containing about 2200 wppm of hydrogen and 4400 wppm of oxygen, failed under tension at 580 °C on cooling from the β_{Zr} domain (Le Hong, 2020).

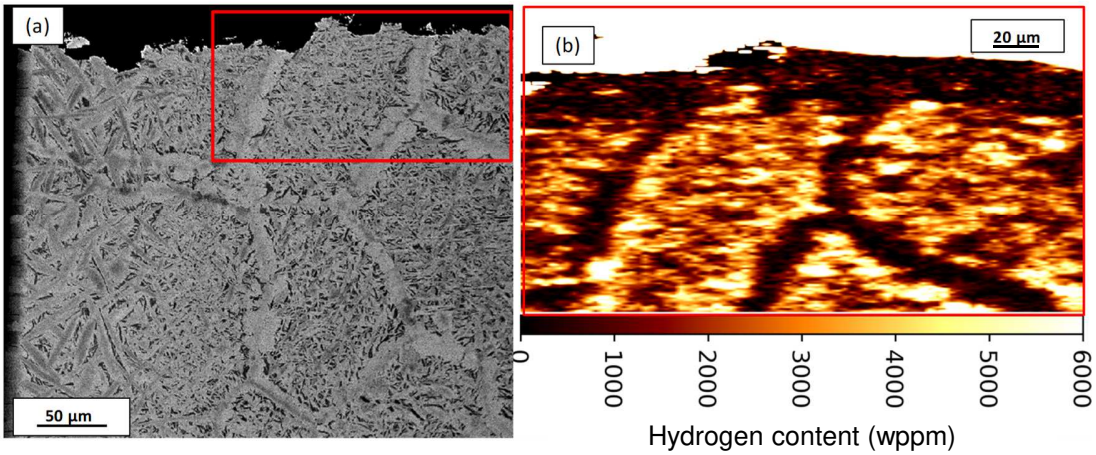

Figure 1.21 – (a) SEM image (backscattered electron mode) and (b) hydrogen mapping (corresponding to the red boxed area on the top right of the SEM image) obtained by µ-ERDA, near the fracture surface of a Zircaloy-4 specimen containing about 2000 wppm of hydrogen and 2000 wppm of oxygen, failed under tension at 135 °C on cooling from the β_{Zr} domain (Le Hong, 2020).

a significant amount of hydrogen can remain in solid solution in α_{Zr}. The results also showed that the metallurgical evolution and the evolution of the lattice parameters of the different phases (see figure 1.23) are significantly influenced by the partitioning of oxygen and hydrogen, which occurs during the β_{Zr} to α_{Zr} transformation. This partitioning is responsible for the microchemical heterogeneities observed, which have an effect on local deformation and failure modes, as previously mentioned.

Conclusions: The mechanical behavior and the failure mode of the (prior-)β_{Zr} material strongly depend on its hydrogen and oxygen contents and on the testing temperature, in relation to the fraction, spatial distribution, chemical composition and mechanical behavior of the phases present in the material. This study has demonstrated the necessity of considering the cumulative effects of hydrogen and oxygen to accurately interpret the embrittlement of claddings subjected to secondary hydriding during LOCA. Going a step further, the data on local hydrogen and oxygen concentrations obtained from the characterizations presented in section 1.7, along with the models established to describe the macroscopic mechanical behavior of the material, could be used for FE simulations to predict the mechanical response of claddings that have undergone secondary hydriding, both during and after cooling and quenching.

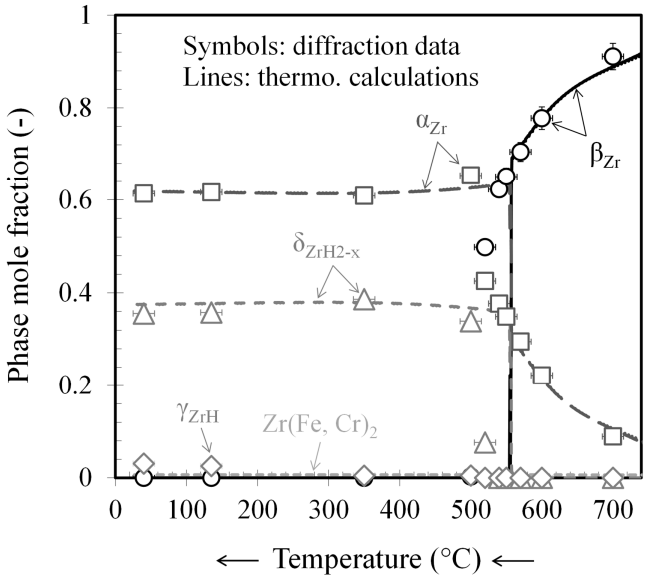

Figure 1.22 – Evolution of the mole fraction of the phases as a function of temperature, obtained by neutron diffraction performed in situ during step-cooling from 700 °C, and by thermodynamic calculations, for Zircaloy-4 containing about 3300 wppm of hydrogen and 2000 wppm of oxygen water-quenched from 1000 °C (Le Hong et al., 2020).

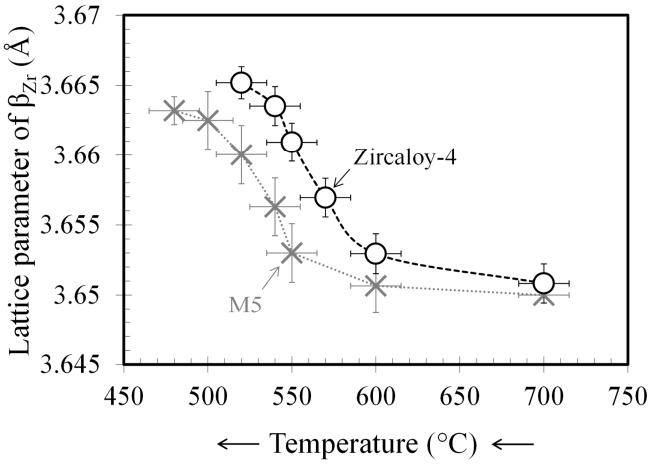

Figure 1.23 – Evolution of the lattice parameter of the β_{Zr} phase as a function of temperature, obtained by neutron diffraction performed in situ during step-cooling from 700 °C on Zircaloy-4 and M5 containing about 3300 wppm of hydrogen and 2000 wppm of oxygen water-quenched from 1000 °C (Le Hong et al., 2020).

Chapter 2

Corrosion at HT and mechanical response of chromium-coated zirconium alloys

Contents

2.1 Introduction

Following the Fukushima Daiichi nuclear disaster in 2011, numerous studies are being carried out around the world to develop enhanced accident tolerant fuel cladding materials, in order to improve the safety of PWRs. In particular, the objective is to slow down the oxidation of the cladding under nominal, and more importantly, accidental conditions. The aim is to reduce the cladding's embrittlement, the heat generated by the exothermic oxidation reaction of zirconium, and the emission of gaseous hydrogen. A study I took part in at CEA demonstrated that this objective could be achieved by depositing a thin layer of chromium (a few micrometers thick) on the surface of the zirconium alloy cladding tube [1]. This initial study was published in 2015 (Brachet et al., 2015) and 2019 (Brachet et al., 2019). The fabrication process has been optimized and internationally patented in 2016 (Brachet et al., 2016).

[1] One advantage of this concept is that the general geometry of the fuel assemblies and the macroscopic behavior of the cladding are not radically changed. In addition, the thin coating thickness allows the use of chemical elements for the coating that are more penalizing in terms of neutron absorption.

It is based on physical vapor deposition (PVD), using direct-current/high power impulse magnetron sputtering (DC/HiPIMS). With optimized deposition parameters, the process produces a dense coating with no visible defects in the thickness or at the interface with the substrate. Throughout the process, the substrate remains at a temperature below 250 °C, ensuring that its properties remain unaltered.

Between 2012 and 2018, I was engaged in research on the behavior of chromium-coated zirconium alloys [2], with a particular focus on two key areas: firstly, the mechanical behavior at low temperature (nominal conditions), and secondly, the oxidation in steam at HT and the subsequent mechanical response during and after cooling (accidental conditions). The following sections present the main work carried out.

2.2 Mechanical behavior of the chromium coating on a zirconium alloy substrate

Context: In order to anticipate the response of the coated cladding, it is essential to have a comprehensive understanding of the mechanical behavior of the chromium coating. In particular, it is important to guarantee that the coating remains undamaged under reactor operating conditions, in order to ensure that it can fulfill its protective role against corrosion. The data available in the literature on the mechanical behavior of chromium is limited and predominantly concerns bulk chromium. Nevertheless, it was expected that the mechanical behavior of the thin chromium coating of interest, which has been deposited by a particular process, differ from that of a bulk material due to specific grain size, texture, purity, or thin film effects. In addition, the stress and mechanical response of the coating are probably influenced by the ductile behavior of the substrate. It is therefore important to characterize the coating as it is deposited on its substrate. During the coating deposition process, residual stresses are generated within the coating. These residual stresses can influence the coating's apparent mechanical response. Furthermore, during nominal operation, the cladding tube is subjected to mechanical loadings that can be biaxial, along its axial and circumferential directions. Therefore, it is essential to investigate the mechanical behavior of the coating in relation to the stress state.

Objectives: As part of D.V. Nguyen's PhD thesis [3] (Nguyen, 2021), we have developed and implemented an approach for the investigation of the mechanical behavior of chromium coatings deposited on a zirconium alloy substrate. A portion of this work has been published in 2022 (Nguyen et al., 2022).

Methods: A chromium coating with an approximate thickness of 15 µm was deposited on zirconium alloy substrates using a DC/HiPIMS PVD process. FEG-SEM observation and contact roughness measurements were conducted in order

[2] This work was initially supported exclusively by the CEA, then by the CEA, Framatome and EDF.

[3] This thesis was defended in 2021. It was funded by CEA, AREVA and EDF.

to characterize the surface and roughness of the coating. The microstructure and crystallographic texture of the coating were characterized by EBSD analysis. Synchrotron XRD analysis was employed to estimate the mean initial stresses in the coating, using the $\sin^2\psi$ method [4].

The behavior of the coating was investigated in the reception state (i.e., non-irradiated or oxidized) at 20 °C. Several experimental techniques were employed at different scales, including biaxial tests with several stress biaxiality ratios on tube samples [5], and in situ uniaxial tensile tests conducted under SEM on sheet samples. The plasticity and cracking of the coating were examined through the use of acoustic emission (AE), DIC, OM, and SEM.

In order to interpret the experimental observations, a modeling approach was implemented. Numerical simulations were conducted using a fast Fourier transform (FFT)-based homogenization technique (to solve the Lippmann-Schwinger equation) [6]. The plasticity of the substrate has been taken into account. Cracking of the coating was described as occurring when the energy release rate associated with crack propagation reaches a critical value.

Results: It has been observed that the surface roughness of the coating is comparable to that of the non-coated substrate. The coating is composed of columnar grains with a size range from a few tenths of a micrometer to a few micrometers (see figure 2.1), and exhibits a strong fiber crystallographic texture. The coating is initially subjected to compressive residual stresses on average. As illustrated in

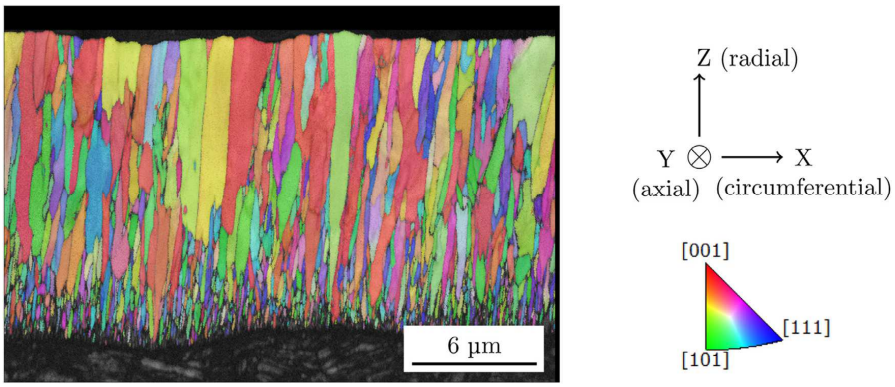

Figure 2.1 – Inverse pole figure map of the tube axial direction with respect to the crystal directions, obtained from cross-sectional EBSD analysis in the thickness of a chromium coating deposited on a M5 cladding tube (Nguyen, 2021; Nguyen et al., 2022).

figure 2.2, the mechanical characterization has shown that the chromium coating has

[4] As a first approach, this method was used despite the pronounced crystallographic texture of the coating material. Stresses were therefore evaluated in a semi-quantitative manner.

[5] An internal pressure and an axial force were simultaneously applied.

[6] These simulations were conducted using the `AMITEX` code: `https://amitexfftp.github.io/AMITEX/`.

minor effect on the macroscopic mechanical behavior of the coated material. The coating cracks when the substrate begins to deform plastically. The strain at the crack onset is dependent upon the stress biaxiality. When the maximum principal stress reaches a critical value, cracks initiate and propagate preferentially parallel to the coating/substrate interface (channeling cracks), in the direction normal to the direction of that maximum principal stress. As shown in figure 2.2, the crack density increases rapidly after the first cracks appear, but reaches saturation after a certain level of applied deformation. The chromium coating initially fractures in a brittle manner, but then exhibits plastic deformation, as illustrated in figure 2.3. The cracks, both transgranular and intergranular, propagate through the entire thickness of the coating but do not significantly penetrate the substrate. The coating demonstrates good adherence to the substrate. As shown in figure 2.4,

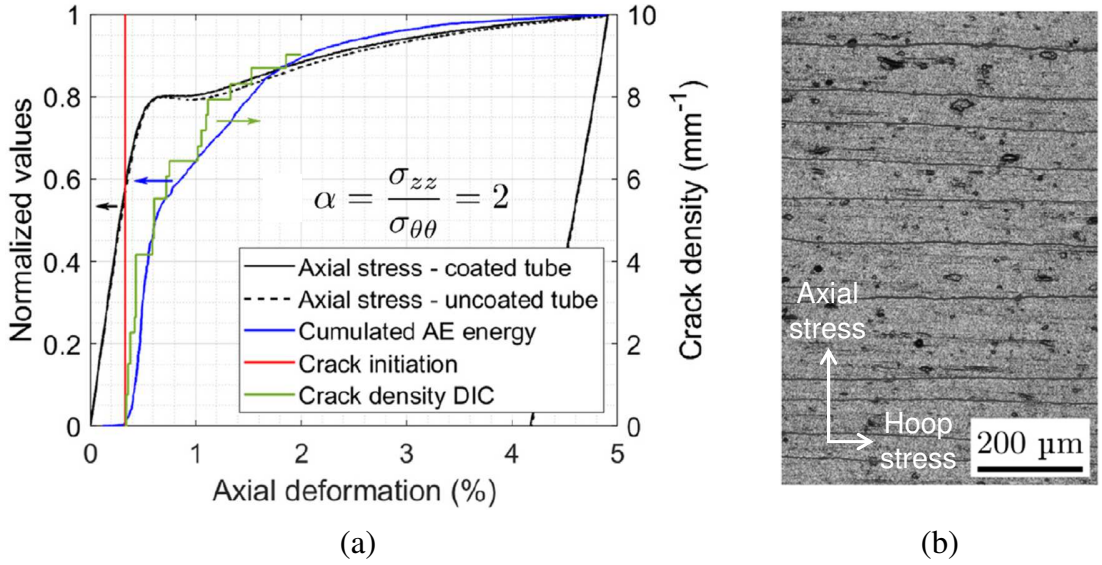

Figure 2.2 – (a) Macroscopic nominal stress-strain curves obtained from biaxial tests performed at room temperature on chromium-coated and uncoated M5 cladding tubes with a ratio between axial and hoop stresses of 2; crack density in the coating determined by DIC and AE. (b) Crack pattern at the coating surface observed by OM after the test (Nguyen, 2021; Nguyen et al., 2022).

the results of the simulations indicated that the use of a non-linear (reversible) elasticity model equivalent to a plasticity model in the case of monotonic loading to describe the behavior of the substrate, as is often done in fracture mechanics, does not permit the accurate estimation of the energy release rate and, consequently, the crack density. It was shown that the cracking kinetics of the coating is significantly influenced by the plasticity of the substrate. Saturation of the coating cracking is attributed to the localization of plastic deformation in the substrate at the bottom of the cracks.

Conclusions: The simulations provide a means of interpreting the experimental results. The coating cracks when the maximum principal stress or the energy release

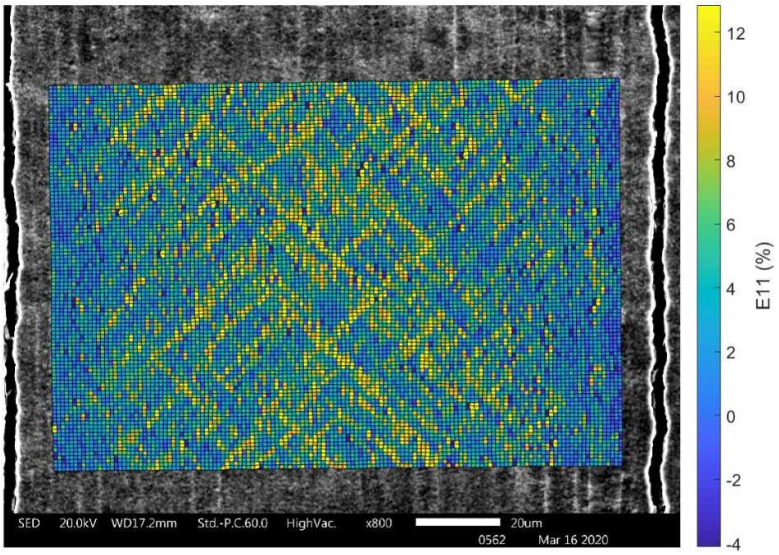

Figure 2.3 – Map of local strain along the loading direction (horizontal) measured by DIC on the chromium coating on a M5 substrate at 6% of macroscopic strain during an in situ tensile test conducted at 20 °C in SEM (Nguyen, 2021; Nguyen et al., 2022).

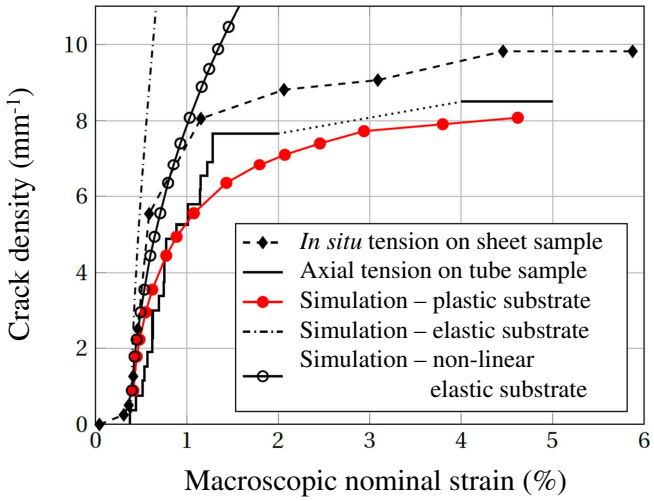

Figure 2.4 – Evolution of crack density as a function of macroscopic strain measured during axial tensile tests performed at 20 °C on chromium-coated M5 sheet sample (in situ test inside SEM) and tube sample; comparison to the results obtained from FFT-based simulations assuming that the coating is elastic and the substrate is elasto-plastic or elastic, and that cracks appear when the energy release rate reaches a critical value (Nguyen, 2021; Nguyen et al., 2022).

rate reaches a critical value, regardless of the stress biaxiality. The cracking of the coating is contingent upon the plasticity of the substrate. The methodologies developed during this thesis could be applied to irradiated coated claddings or higher temperatures.

2.3 Corrosion at HT and subsequent mechanical response

Context: The primary function of the chromium coating is to slow down the oxidation of the claddings in hypothetical accidental conditions in which they would be subjected to steam at HT, up to 1200 °C in LOCA conditions or even higher temperatures (up to 1500 °C typically) in design extension conditions. For oxidation temperatures above 1300 °C, an eutectic reaction is anticipated to occur between zirconium and chromium. There were almost no data in the literature on the oxidation at HT of chromium-coated zirconium alloys.

Objectives: We therefore studied the HT steam oxidation of chromium-coated zirconium alloy claddings, their mechanical strength during post-oxidation quenching and their residual ductility after quenching. The impact of the eutectic reaction between zirconium and chromium on the oxidation kinetics of the cladding was examined. This work has been the subject of papers published in 2015 (Brachet et al., 2015) and 2020 (Brachet et al., 2020a, b).

Methods: This study was carried out on samples with coatings of varying thicknesses, typically between 5 µm and 20 µm, deposited using a DC/HiPIMS PVD process on a Zircaloy-4 substrate initially and on a M5 substrate subsequently. The samples were oxidized in flowing steam at several temperatures between 800 °C and 1500 °C, with oxidation times ranging from a few minutes to a few hours. They were then quenched with water at room temperature. The hydrogen content in the samples was measured using an inert gas fusion thermal conductivity technique. In order to interpret the results, EPMA, SEM, EBSD and transmission electron microscopy (TEM) analyses were carried out on certain samples. Diametral compression tests were performed at 20 °C and 135 °C on samples cut from the HT oxidized and quenched tubes, to assess their post-quench mechanical response. Additionally, calorimetric measurements were conducted to investigate the temperature range over which the eutectic reaction between zirconium and chromium occurs.

Results: As illustrated in figure 2.5, the results showed that when the coating is of the appropriate thickness and deposited using optimized process and parameters, the chromium-coated materials exhibit significantly slower HT steam oxidation than the uncoated materials. After a certain oxidation period (approximately 5000 s in the example in figure 2.5), the oxidation kinetics of the coated material shows a transition and accelerates. However, the level of oxidation for a given time remains significantly lower than for the uncoated material. Prior to this oxidation transition, no hydrogen uptake was observed. A transient hydrogen uptake was observed at

the time of the transition. The results illustrated in figure 2.6 demonstrated that for oxidation temperatures below 1300 °C, the oxidation of the chromium-coated material can be divided into three main successive stages, involving the growth of an outer protective chromia layer, Zr-Cr interdiffusion, thickening of a $Zr(Cr, Fe)_2$ inter-layer, diffusion of chromium within the prior-β_{Zr} substrate, transport of oxygen through the residual metallic chromium and into the zirconium substrate, and finally growth of zirconia beneath the heavily oxidized residual chromium coating.

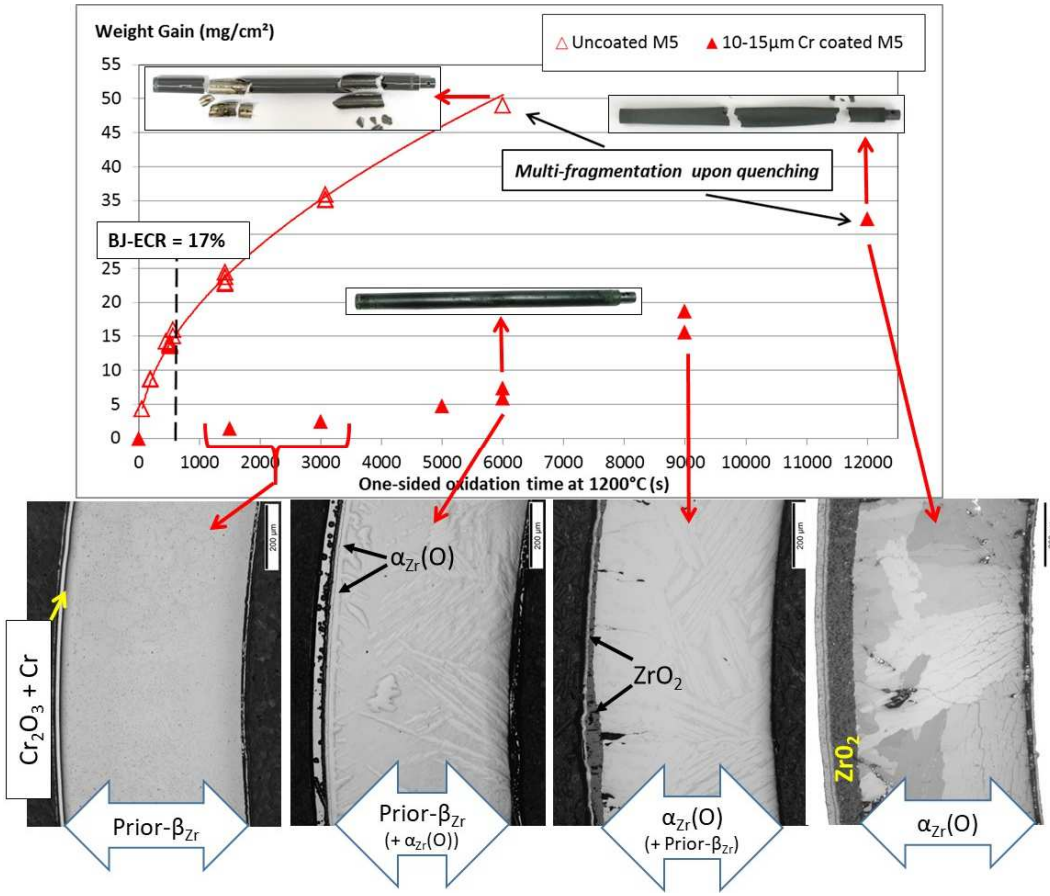

Figure 2.5 – Results of single-sided oxidation tests in steam at 1200 °C and water-quenching, carried out on M5 cladding samples without coating or with a 12–15 µm-thick chromium coating: weight gain as a function of oxidation time, and photograph and optical micrograph of the transverse cross-section of certain samples after the test (Brachet et al., 2020a).

Furthermore, the results indicated that the critical oxidation time at a given temperature, at which the cladding sample breaks during quenching under the influence of thermal stresses (induced by differences in thermal expansion and phase changes), is significantly longer for the coated material than for the uncoated one (see example in figure 2.5). Consistently, the oxidation time after which the material becomes brittle after quenching is much greater for the coated material (figure 2.7). Investigations have shown that the embrittlement of the coated cladding, like that

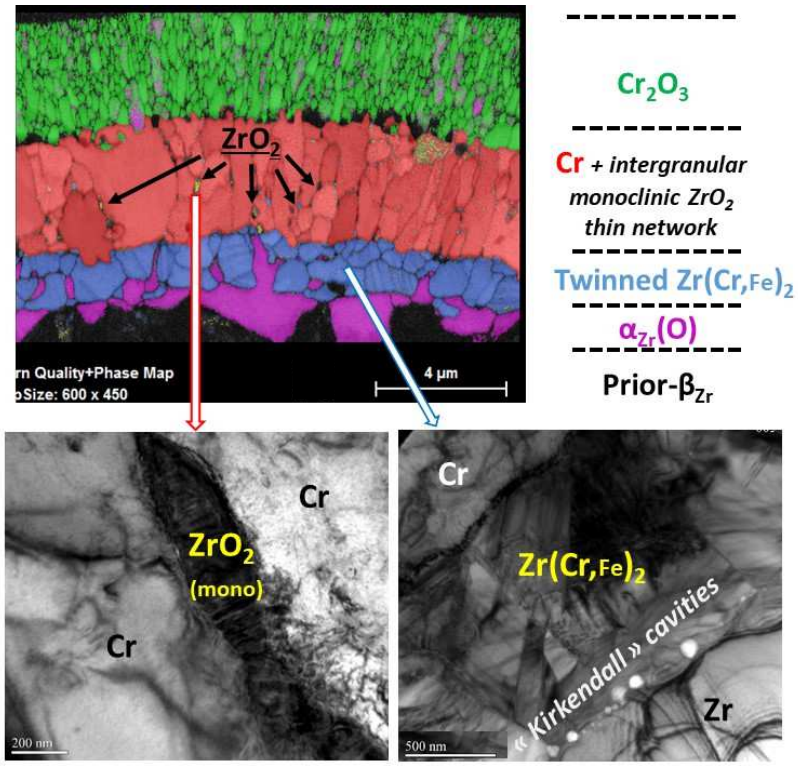

Figure 2.6 – SEM-EBSD phase map and TEM micrographs in a transverse cross-section of a Zircaloy-4 sheet sample with a 12–15 µm-thick chromium coating, after steam oxidation for 1400 s at 1200 °C (oxidation transition stage) and quenching (Brachet et al., 2020b).

of the uncoated cladding (as already discussed in chapter 1), is largely controlled by the diffusion of oxygen into the zirconium substrate. This diffusion is delayed in the presence of a coating.

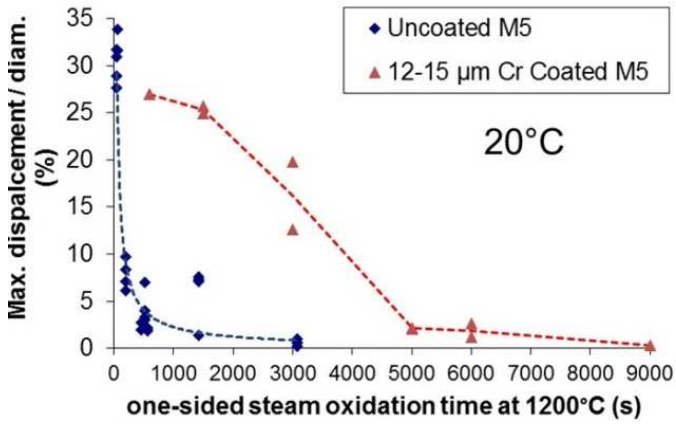

Figure 2.7 – Evolution of the plastic displacement at failure in relation to the initial sample diameter measured during diametral compression tests at 20 °C, as a function of the oxidation time at 1200 °C before quenching, for uncoated M5 and M5 coated with a 12–15 µm-thick chromium coating (Brachet et al., 2020a).

It has been determined that the eutectic reaction between zirconium and chromium occurs at 1305–1325 °C (in near thermodynamic equilibrium conditions). As illustrated in figure 2.8, claddings oxidized at temperatures exceeding 1300 °C exhibit a pattern of protuberances aligned with "pockets" that were liquid at HT due to the eutectic reaction [7]. Local oxidation at these protuberances is the same as elsewhere. The results therefore suggested that the formation of a Zr-Cr liquid phase does not drastically alter the HT oxidation mechanisms and cladding kinetics, at least for the relatively short oxidation times experienced.

Conclusions: The chromium coating deposited using an optimized PVD process results in a significant prolongation of the oxidation time before the cladding becomes completely embrittled. This work contributed to the validation of the concept of zirconium alloy cladding coated with an outer layer of chromium, which led to the introduction of the first fuel rods with this type of cladding in nuclear power reactors in 2019.

The coating mentioned above is only applied to the outer surface of the cladding [8]. However, as mentioned in section 1, under accidental conditions such as a LOCA, the cladding can burst. Its inner surface would then be exposed to HT steam. It is not possible to deposit a coating on the inner surface of a cladding tube using a PVD-type process. I contributed to an early study of the corrosion resistance at HT of an amorphous Cr_xC_y coating deposited on the inner surface of zirconium alloy

[7] This pattern could be due to a small displacement of the Zr-Cr eutectic film caused by possible "capillary" effects of the liquid and the local swelling associated with the solid-liquid volume change.

[8] This is essentially the surface exposed to a corrosive environment.

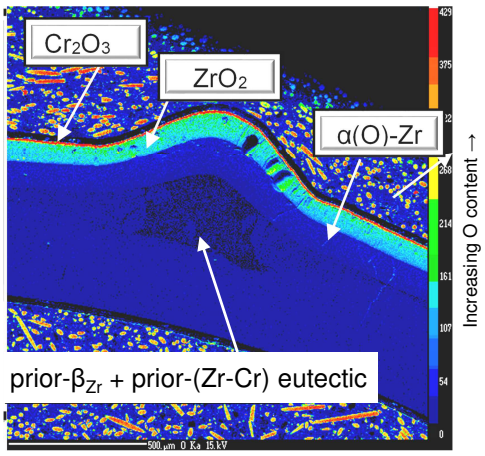

Figure 2.8 – Oxygen mapping obtained by EPMA near a protuberance in a chromium-coated M5 cladding sample oxidized for 100 s in steam at 1400–1450 °C and water-quenched to room temperature (Brachet et al., 2020b).

cladding tube segments, using a metalorganic chemical vapor deposition process using direct liquid injection (Michau et al., 2018).

Chapter 3

Thermo-metallurgical-mechanical behavior of a martensitic steel at HT

Context: From 2010 to 2019 [1], the CEA led the Advanced sodium technical reactor for industrial demonstration (ASTRID) project, which aimed to demonstrate the feasibility of advancing to the industrial stage with sodium-cooled fast neutron reactors, a technology that would have constituted the fourth generation of reactors [2]. It was planned that the bundles of fuel pins would be held in hexagonal wrapper tube. For the first ASTRID core, it was planned to make these tubes from a 9Cr-1Mo [3] tempered martensitic steel [4]. In nominal operating conditions, the hexagonal wrapper tube is subjected to temperatures typically between 400 °C and 550 °C. In incidental or accidental situations, the material could be exposed to HT, potentially up to 926 °C (boiling temperature of sodium), associated with significant mechanical loading. Work carried out in the 1990s on this material [5] provided data on the mechanical behavior of this material at temperatures below 700 °C. However, there was no data for higher temperatures. The material undergoes a transformation from the body-centered cubic tempered martensitic phase to the face-centered cubic austenitic phase on heating above about 810 °C. This transformation is therefore likely to occur during incidental or accidental transients. It is anticipated that this transformation has an impact on the material's mechanical behavior. Furthermore, this transformation is accompanied by a contraction that could have a negative effect on the geometry of the reactor core.

Objectives: In order to assess the response of the hexagonal wrapper tubes in incidental or accidental situations, we have initiated in 2012 a study with the

[1] In 2019, the CEA has decided to abandon the project or postpone it to the "end of the century".

[2] The majority of reactors currently in operation around the world are of the second generation. The third generation of reactors, including the European pressurized reactor, should gradually take over.

[3] 9 w% Cr, 1 w% Mo.

[4] This material was selected in particular because of its very good resistance to swelling, its stable mechanical properties and its limited embrittlement under irradiation.

[5] This work was conducted in particular in preparation for a new fuel load for the Superphénix sodium-cooled fast reactor, shut down in 1997.

objective of modeling the thermo-metallurgical-mechanical behavior of a 9Cr-1Mo tempered martensitic steel at HT [6]. Some of this work was presented in 2014 (Courcelle et al., 2014).

Methods: The martensite to austenite phase transformation upon heating was investigated through dilatometry tests conducted with different heating rates. In order to characterize the elasto-viscoplastic behavior of the material and its dependence on temperature and the phases present, uniaxial monotonic tensile tests were carried out, with different strain rates (between $8 \cdot 10^{-5}\,\mathrm{s}^{-1}$ and $2 \cdot 10^{-3}\,\mathrm{s}^{-1}$), at various temperatures between 550 °C and 950 °C, with or without prior austenitisation heat treatment. Creep tests were also performed at temperatures between 650 °C and 870 °C with different stress levels. The results of the study were then used to develop a model.

Results: As illustrated in figure 3.1, the martensite to austenite transformation takes place between 830 °C and 930 °C within the heating rate range of interest ($8 \cdot 10^{-2}$–20 °C/s). The faster the heating, the higher the transformation temperature. The transformation of martensite to austenite on heating was described using a phenomenological model, considering that the transformation occurs through germination (incubation) followed by growth and coalescence of austenite.

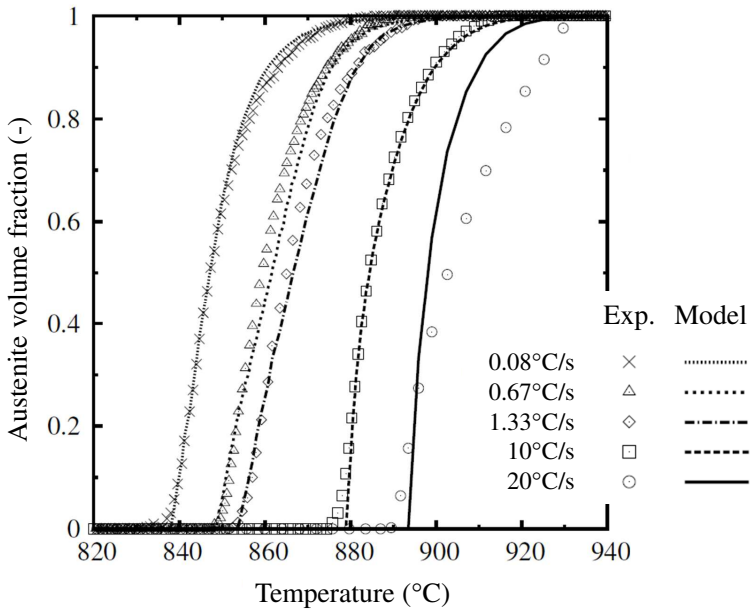

Figure 3.1 – Evolution of the volume fraction of austenite on heating for different heating rates: comparison of experimental data and model predictions (Courcelle et al., 2014).

The mechanical behavior of each phase (martensite and austenite) is described using an isotropic elasto-viscoplastic phenomenological model with non-linear isotropic

[6] This work was funded by the CEA.

strain hardening. The behavior of the two-phase material is expressed as a function of the behavior and the fraction of each phase (calculated using the model mentioned above) using a self-consistent homogenization scheme. Figure 3.2 illustrates the model's ability to describe the response of the material as a function of strain rate, temperature and fraction of phases. Furthermore, the model accounts for strains induced by temperature change and phase transformation.

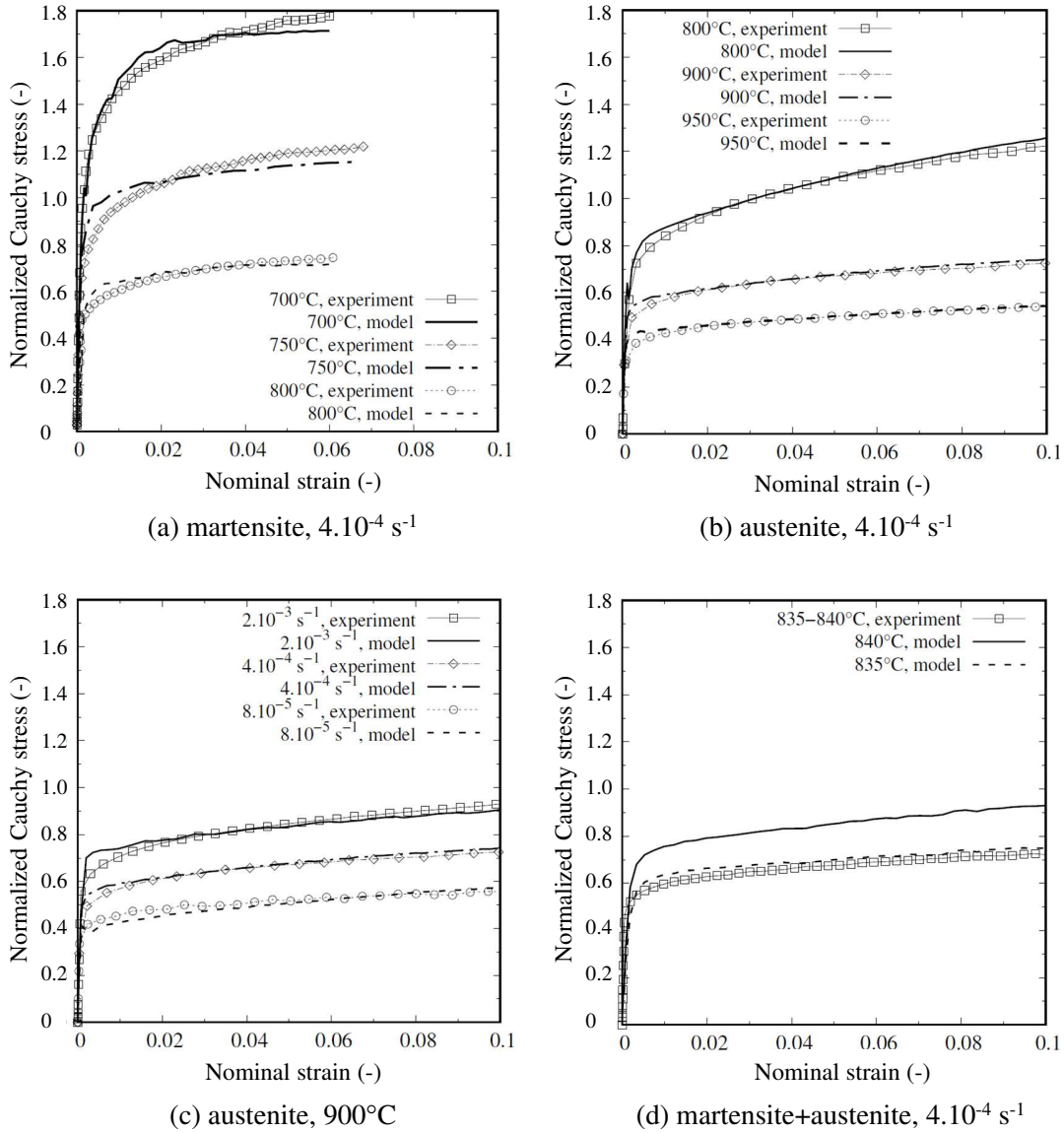

(a) martensite, 4.10^{-4} s^{-1}

(b) austenite, 4.10^{-4} s^{-1}

(c) austenite, 900°C

(d) martensite+austenite, 4.10^{-4} s^{-1}

Figure 3.2 – (Normalized) Cauchy stress-nominal strain curves obtained for uniaxial tension on a 9Cr-1Mo tempered martensitic steel: (a) martensite at 700 °C, 750 °C and 800 °C with a strain rate of $4 \cdot 10^{-4}\,s^{-1}$, (b) austenite at 800 °C, 900 °C and 950 °C with a strain rate of $4 \cdot 10^{-4}\,s^{-1}$, (c) austenite at 900 °C with strain rates of $8 \cdot 10^{-5}\,s^{-1}$, $4 \cdot 10^{-4}\,s^{-1}$ and $2 \cdot 10^{-3}\,s^{-1}$, and (d) two-phase material at 835–840 °C with a strain rate of $4 \cdot 10^{-4}\,s^{-1}$; comparison of curves obtained experimentally and calculated with the model (Courcelle et al., 2014).

Conclusions: The results obtained were used to update the material characterization file for hexagonal wrapper tubes. The model developed was implemented numerically [7], in finite strain [8], in order to permit the simulation of the response of hexagonal wrapper tubes in incidental and accidental conditions.

[7] The implementation was carried out using the `TFEL/MFront` code generator: `http://tfel.sourceforge.net/`.

[8] Strains can reach several percent.

Chapter 4

Thermomechanical behavior and fatigue of short fiber-reinforced thermoplastic composites

Contents

4.1 Introduction

Short fiber-reinforced thermoplastic (SFRT) composites have a wide range of applications in many industrial sectors, including the automotive and aeronautical industries. They are typically used as a replacement for metallic materials. In service, the parts/components concerned may be subjected to cyclic mechanical loading, often multiaxial and variable over time, in addition to a variety of environmental conditions. The implementation of a fatigue design approach is particularly challenging for this type of material due to its

- non-linear dissipative mechanical behavior, linked to the matrix,
- anisotropic and heterogeneous nature, due to the heterogeneous preferential orientation of the fibers, related to the injection process [1] (see example in figure 4.1).

[1] The fibers are often predominantly oriented along the direction of injection in the "skins" of the parts and more or less perpendicular to this direction in the "core" (skin-core microstructure).

- sensitivity to the environment, in particular temperature and humidity,
- sensitivity to mechanical loading conditions, such as the minimum to maximum load ratio and the stress mode.

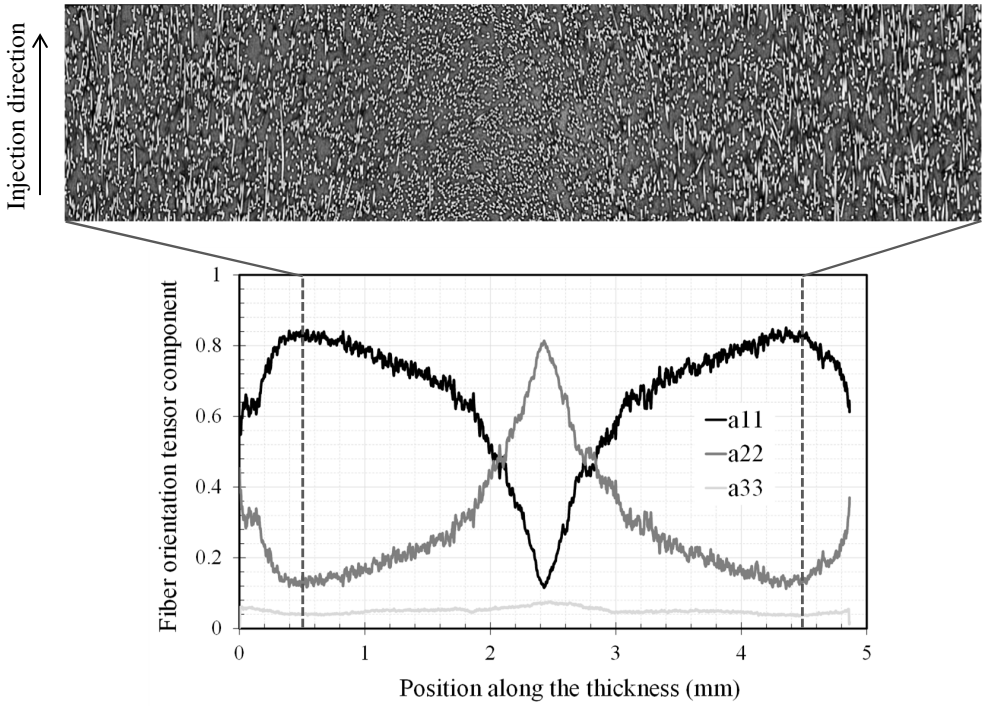

Figure 4.1 – Micro X-ray computed tomography image of a section of a sample taken from an injection-molded plate of PolyEtherEtherKetone (PEEK) reinforced with 30 w% of short carbon fibers (PEEK CF30), in a plane according to the thickness of the plate and the direction of injection; corresponding distribution, along the thickness of the sample, of the diagonal components of the second-order fiber orientation tensor in the orthonormal basis with the injection direction as the first axis and the thickness as the third one (Kwiatkowski, 2023; Kwiatkowski et al., 2023).

The research activities in which I have been involved since 2018 at ENSTA / IRDL on this subject aim at establishing an appropriate experimental characterization approach and then developing mechanical behavior laws and fatigue criteria that allow these multiple phenomena and factors to be taken into account in a unified way. The work places particular emphasis on mechanical loading conditions that have been little investigated until now for these types of materials, but which are of interest for certain applications. This includes compression-compression for example.

Furthermore, the characterization of fatigue properties using conventional tests can be particularly time-consuming for polymer-based materials. This is due to the necessity of maintaining a sufficiently low frequency of the load applied, a few hertz

at most [2], in order to avoid excessive self-heating, which would lead to biases. The self-heating (or heat build-up) method [3] has been successfully applied to accelerate the characterization of the fatigue life of a wide range of materials. Nevertheless, the correlation between self-heating and fatigue life remains unclear for polymer matrix composites. The analysis of the self-heating curve [4] is often conducted empirically, without a clear physical justification. Furthermore, the analysis provides only the mean fatigue lifetime, without the scattering. The objective of our research is not only to apply the method to other composite materials and to other stress conditions, but also and primarily to establish a link between the dissipated energy and the fatigue life. This should enhance the robustness of the rapid self-heating characterization method and enable the construction of fatigue curves with the associated dispersion. This analysis is based on the examination of damage mechanisms and the formulation of behavior laws that can account for the contributions of the various dissipative phenomena.

The following sections provide a summary of published work carried out on these subjects.

4.2 Fatigue criterion taking into account the effects of orientation, environment and load ratio

Context: As mentioned above, the fatigue of SFRTs is generally dependent on the loading direction (relative to the fiber orientation distribution), the loading ratio and the environment. Numerous fatigue criteria have been proposed in the literature for these materials. Several of them take into account the effects of orientation and environment. Some are also able to account for the effects of load ratio, but only over a limited range. There is a lack of criteria for correctly describing fatigue that take into account the effects of orientation and environment, as well as the effect of the load ratio over a wide range, including both highly negative and positive ratios. Furthermore, the generation of an experimental database encompassing the aforementioned effects necessitates a significant investment of time and resources. It would therefore be useful to know the minimum experimental database required for the robust identification of the parameters of the criterion.

Objectives: Consequently, during P. Santharam's PhD thesis [5] (Santharam, 2020), we conducted a research project with the objective of determining a fatigue

[2] For example, at a loading frequency of 4 Hz, it takes almost three days to reach 10^6 cycles.

[3] "Classical" self-heating tests consist of subjecting a sample to a series of cyclic loading steps with increasing stress amplitude and measuring the temperature evolution for each step in order to deduce the dissipated energy density per cycle using the heat equation.

[4] This curve shows the energy density dissipated per cycle as a function of maximum stress or stress amplitude.

[5] This thesis was defended in 2020. It was carried out within the framework of a "Convention industrielle de formation par la recherche" (CIFRE) contract with Vibracoustic with the financial support of the french "Association nationale de la recherche et de la technologie" (ANRT), as part of the IDAFIP project.

criterion that would permit the description of fatigue for a variety of loading directions, load ratios and environments in a unified way, with a single set of parameters. Furthermore, we conducted an investigation into the minimum experimental database required to identify the parameters of the fatigue criterion in order to ensure that the criterion accurately predicts fatigue performance across a wide range of conditions. This work was published in 2020 (Santharam et al., 2020).

Methods: A comprehensive fatigue database comprising almost 500 uniaxial cyclic tests has been constructed for Polyamide 66 reinforced with 50 w% of short glass fibers (PA66 GF50) [6], for

- three loading orientations in relation to the injection direction: 0 °, 45 ° and 90 °;
- two environmental conditions [7]: relative humidity $RH = 50\%$ and test temperature $T = 80\,°C$; $RH = 80\%$ and $T = 23\,°C$; the test temperature is approximately 45 °C higher than the glass transition temperature T_g for the first condition and 30 °C higher for the second;
- a wide range of minimum to maximum stress ratios R_σ, in tension-tension and tension-compression, between -0.5 and 0.7.

The tests were carried out in a climatic chamber. The loading frequency was 3 Hz. The temperature field at the surface of the sample was measured using an infrared (IR) camera to check that the temperature rise due to dissipation was limited. In addition, the deformation of the samples was measured by stereo DIC. The database encompasses a range of number of cycles at failure extending from approximately 10^3 to $3 \cdot 10^6$ cycles. A number of mechanical quantities were derived from the data, including the secant modulus [8], the cyclic strain rate [9], the cyclic creep energy density [10], the energy density involved in the hysteresis loop of the stress-strain response, the cyclic elastic energy density [11], and the tensile cyclic elastic energy density [12]. A total of ten fatigue criteria from the literature were evaluated for their ability to describe the full database, both with and without a unified set of parameters. These include classical and recent criteria based on stress, cyclic strain rate or energy density.

Results: As shown in figure 4.2, the analysis demonstrated that the criteria based on stress components are effective in unifying the orientation and environmental effects when stress is divided by the ultimate stress at failure under monotonic tension. However, they do not succeed in unifying the influence of the load ratio with a single set of parameters. Criteria based on the ratcheting effect, such as cyclic

[6] This material is used for automotive structural components, for example.

[7] These conditions are representative of the conventional atmospheric conditions typically experienced by automotive motor mounts and chassis mounts, respectively.

[8] Ratio between the amplitude of strain and the amplitude of stress.

[9] Increment of mean strain per cycle.

[10] Cyclic strain rate multiplied by average stress.

[11] Half the product of the amplitude of strain and the amplitude of stress, in tension and compression.

[12] Only the part of the cyclic energy density relating to tension is considered.

strain rate or cyclic creep energy density, have been demonstrated to yield highly satisfactory results for positive stress ratios. However, they are unable to provide a unified interpretation of the tests performed for negative stress ratios. The application of criteria based on cyclic energy densities, such as the hysteresis, cyclic elastic or tensile cyclic elastic energy densities, may be effective in certain instances. However, they are inadequate for describing high positive stress ratios, which cause significant ratcheting. We have proposed two variants of a fatigue criterion, designated IDAFIP, that combines the ratcheting and cyclic features. The first one combines the cyclic creep energy density with the hysteresis energy density. The second one combines the same creep energy density with the cyclic elastic energy density. Both variants result in an excellent unification of the database (see figures 4.2 and 4.3). The best results are obtained by considering the energy density values obtained at mid-life. Nevertheless, very good results can be achieved by using values at a given, lower number of cycles, provided that this number is sufficient for the thermomechanical response of the material to have stabilized [13].

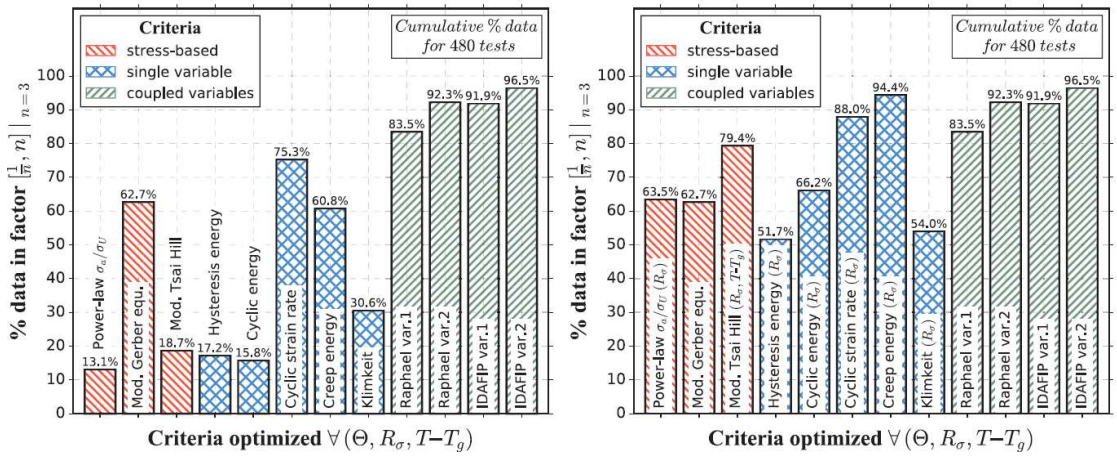

(a) (b)

Figure 4.2 – Percentage of fatigue life data on PA66 GF50 predicted by different criteria within a band of factor 3 using (a) constant parameters and (b) parameters dependent on the orientation Θ, R_σ and/or $T - T_g$ (additional dependence shown in brackets) (Santharam et al., 2020; Santharam, 2020).

The study of the influence of the database was conducted using the second IDAFIP criterion. The results demonstrated that a single atmospheric condition could be sufficient to obtain a reliable assessment for the other (at least as long as the temperature difference with respect to T_g is not too large). As shown in figure 4.4, two distinct orientations should be included in the identification database to ensure optimal results. It was found that identification performed using only two load ratios can give very good results, provided that the two load ratios lead to combined variations of creep and cyclic energies.

[13] This number varies from a dozen to several hundred or even thousands of cycles, depending on the case.

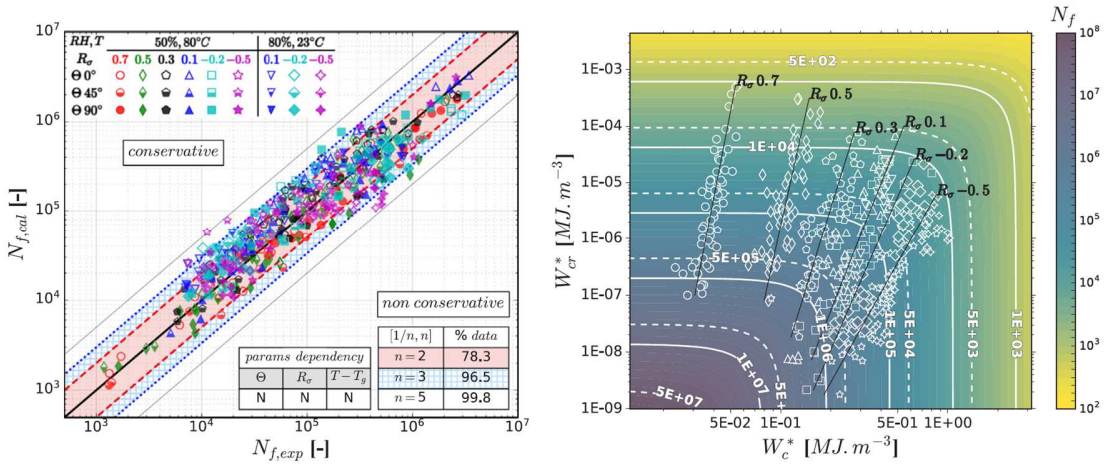

(a) (b)

Figure 4.3 – Performance of the IDAFIP criterion combining a cyclic creep energy and a cyclic elastic energy (at mid-life): (a) comparison of the number of cycles at failure predicted by the criterion and the experimental one for PA66 GF50, for three orientations Θ, several R_σ, and two conditions of RH and T (the table at bottom right gives the percentage of data predicted within bands of factors 2, 3 and 5); (b) shape of the iso-fatigue lifetime as a function of the cyclic elastic energy density W_c^* and the cyclic creep energy density W_{cr}^* (Santharam et al., 2020; Santharam, 2020).

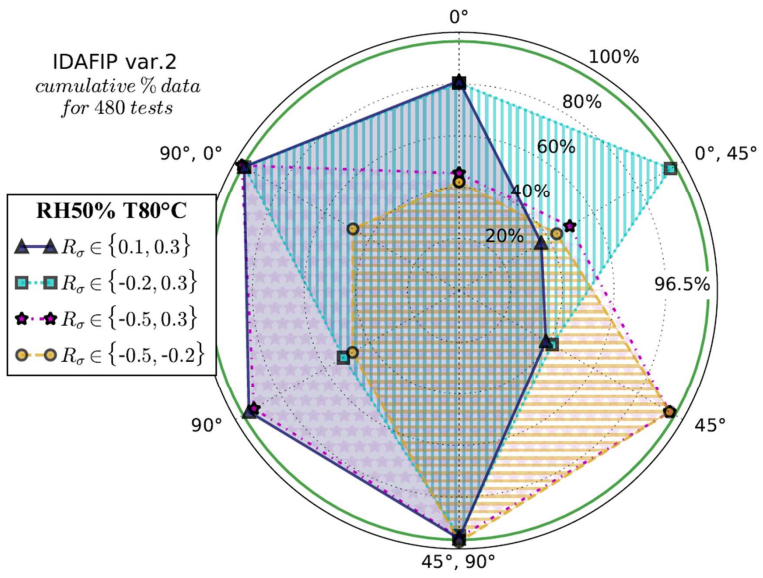

Figure 4.4 – Percentage of fatigue life data on PA66 GF50 predicted by the IDAFIP criterion combining a cyclic creep energy and a cyclic elastic energy (at mid-life), identified over a reduced database including only one atmospheric condition ($RH = 50\%$ and $T = 80\,°C$) and one, or two orientations, for several sets of stress ratios; the green line at 96.5% corresponds to the prediction obtained when parameter identification is based on the entire database (Santharam et al., 2020; Santharam, 2020).

Conclusions: The majority of existing fatigue criteria are unable to provide an accurate description of fatigue life in a unified way, with a single set of parameters, for different orientations, different environmental conditions and, above all, different load ratios, both positive and negative. The proposed IDAFIP criteria can achieve this with only four parameters. The criteria have been validated for uniaxial loading. They now need to be extended to multiaxial loading, so that they can be used to design structures.

4.3 Fatigue under compression: influence of load ratio and prediction from self-heating measurements

Context: In certain industrial structures, the material may be subjected to fatigue under compression-compression cyclic loading. The majority of fatigue data on SFRTs in the literature has been obtained for tension-tension or tension-compression loadings. Furthermore, the limited number of studies that have addressed the fatigue of SFRTs under compression-compression loading have focused on materials other than PEEK CF30, which is being considered as a replacement for metallic materials for certain parts in aircraft landing gear dampers. In addition, it is challenging to perform uniaxial compression tests on samples extracted from plates without premature buckling. The anti-buckling devices frequently used can induce bias (friction, inertia, ...) and make it difficult to change the temperature and to accurately assess strain, stress and temperature in the gauge zone of the specimen. Moreover, the fatigue criteria mentioned in section 4.2 have not been tested for the material considered here, nor for compression-compression loading. Finally, the self-heating method has been successfully applied to SFRTs for cyclic tension-tension loading, but has not yet been investigated for loading involving compression, in particular compression-compression.

Objectives: As part of V. Kwiatkowski's PhD thesis [14] (Kwiatkowski, 2023), we studied the fatigue of PEEK CF30 in compression-compression at different load ratios, and compared it to that obtained in tension-tension and tension-compression. A preliminary objective was to develop a protocol that would enable well-controlled compression tests to be carried out, without the use of an anti-buckling device. Another objective was to study the capacity of the fatigue criteria mentioned above, in particular the IDAFIP criteria, to describe the fatigue life of PEEK CF30 in a unified manner under different load ratios, including compression-compression. A last objective was to investigate the ability of the self-heating approach to rapidly

[14] This thesis was defended in 2023. It was carried out within the framework of a CIFRE contract with Safran Landing Systems with the financial support of ANRT, as part of the "Self-Heating" ANR-Safran-Naval Group research chair involving Safran Companies, Naval Group, ENSTA Bretagne (IRDL), and Institut Pprime.

predict the fatigue life of PEEK CF30 under compression loading. A portion of this study was published in 2023 (Kwiatkowski et al., 2023).

Methods: This work was conducted on PEEK CF30 samples, milled from injection-molded plates measuring 5 mm in thickness, with their gauge length at 0 ° or 90 ° from the injection direction. The distribution of the orientation of fibers through the plate thickness was characterized by processing images obtained using micro X-ray computed tomography (µ-CT). In order to conduct the fatigue tests, the samples were mounted directly in the machine's hydraulic jaws to avoid the disadvantages of anti-buckling devices. The free length of the sample has been optimized to avoid buckling, while retaining a sufficiently large zone where longitudinal strain is homogeneous and allowing kinematic and temperature measurements. An experimental procedure has been developed to detect a potential misalignment of the jaws and ascertain that the loading remains uniaxial during the test. The procedure consists in verifying that the kinematic field and the field of the amplitude of the first harmonic of the temperature signal are symmetric with respect to the specimen's mid-thickness and uniform along the longitudinal direction [15]. The kinematic field was quantified by stereo DIC. The field of the amplitude of the first harmonic was determined from the temperature field measured using an IR camera (under some hypotheses). This amplitude is related to the thermoelastic coupling and thus to the stress state.

The fatigue tests and the self-heating tests were carried out at room humidity [16] and at 25 °C, i.e., at a temperature about 125 °C below T_g. They were conducted with a loading frequency of 2 Hz or 4 Hz and stress ratios of ∞, 10 and 3 (compression-compression), -1 (tension-compression), and 0 (tension-tension). The applied loads resulted in failure after a number of cycles ranging from 10^3 to $4 \cdot 10^6$ cycles. The stress-strain data obtained from the tests were used to calculate the quantities involved in the fatigue criteria. The spatial average of the dissipated energy density per cycle (0D approach) was determined from temperature measurements, which were performed with an IR camera. The evaluation was based on the average rate of temperature increase over the first few cycles (transient approach, adiabatic regime). As a preliminary approach, the empirical method, which has been successfully applied to SFRTs for tensile loading, was employed to establish a fatigue criterion that relates the number of cycles at failure to the energy density dissipated per cycle, from the self-heating curve and one fatigue test [17]. The self-heating curve was then used to relate the number of cycles at failure to the maximum stress in absolute value.

Results: The microstructure was found to be symmetrical with respect to the middle of the sample thickness, and homogeneous along the width and length. The

[15] The material's microstructure is symmetrical along the specimen's thickness and homogeneous along its length.

[16] PEEK is not very sensitive to humidity.

[17] This criterion was identified using only two sets of data: one from a fatigue test; the other from analysis of the self-heating curve. Three distinct regimes were graphically identified on the self-heating curves. It was then assumed that the transition between the first and second regimes corresponds to a given fatigue life, defined arbitrarily at 10^6 or 10^7 cycles.

results illustrated in figure 4.5 demonstrated that a misalignment during the test can be identified through the analysis of the strain field and the field of the amplitude of the first harmonic of the temperature signal. As shown in figure 4.6, the tests

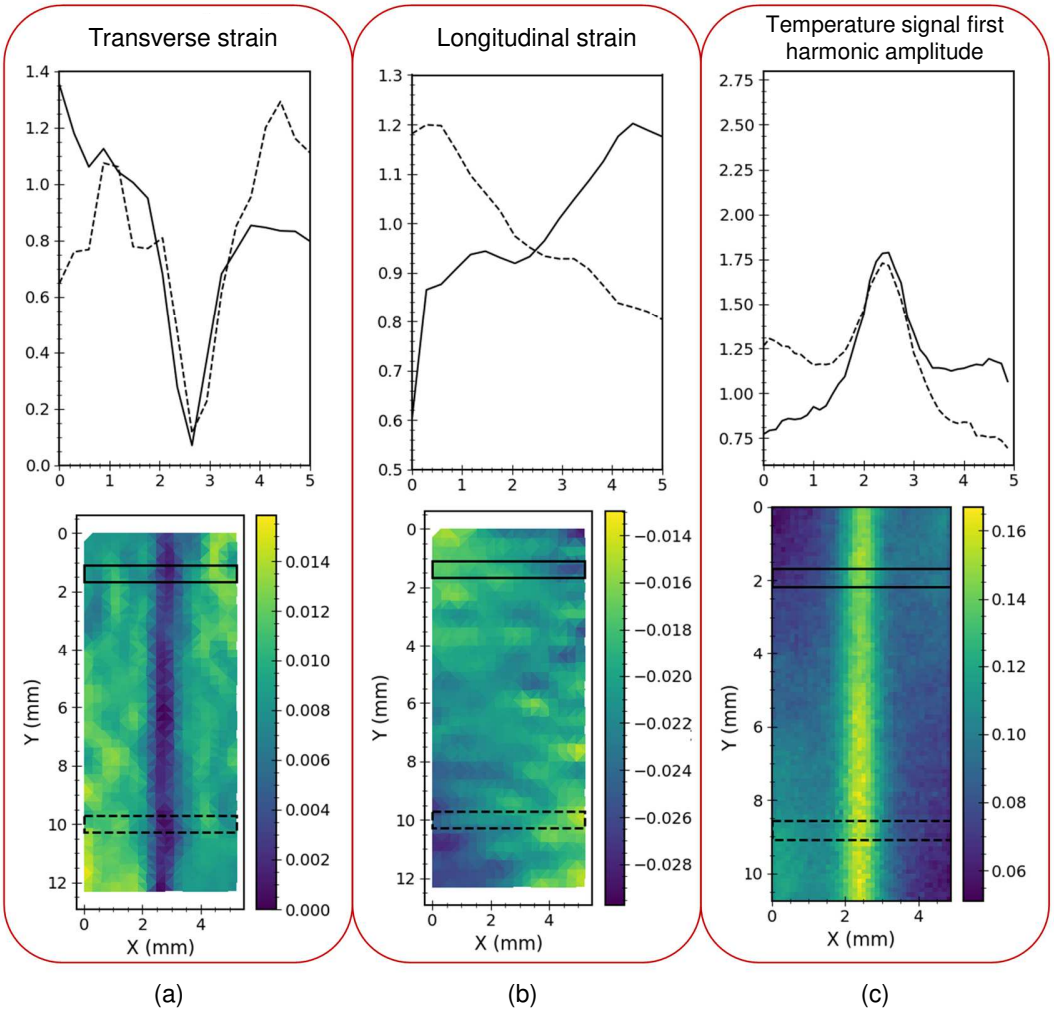

Figure 4.5 – Fields (bottom), and associated normalized profiles along the sample thickness (top), of (a) transverse strain, (b) longitudinal strain and (c) amplitude of the first harmonic of the temperature signal, obtained during a compression test considered as non-uniaxial on a PEEK CF30 sample (X and Y correspond to the sample thickness and length, respectively; the loading is applied along Y) (Kwiatkowski, 2023; Kwiatkowski et al., 2023).

demonstrated that the fatigue lifetime is greater in compression-compression than in tension-tension or tension-compression at equivalent maximum and mean stresses, and that it depends on the load ratio in compression. The study showed that fatigue life in compression-compression is well described using fatigue criteria based on cyclic strain rate and cyclic creep energy density. However, in order to also describe the fatigue life for a stress ratio of -1, it is necessary to associate these quantities with

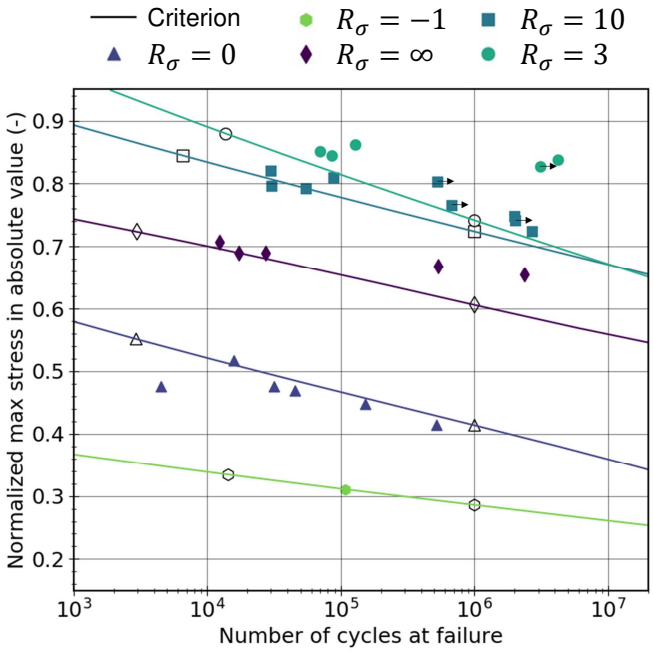

Figure 4.6 – Comparison of fatigue test results on PEEK CF30 loaded along the injection direction, at room temperature, for several stress ratios, and predictions with the dissipated energy-based criterion determined from self-heating results (the empty symbols correspond to the points used to identify the criterion; the transition between the first and the second self-heating regimes is assumed to correspond to a fatigue life of 10^6 cycles) (Kwiatkowski, 2023; Kwiatkowski et al., 2023).

a cyclic energy such as the hysteresis energy density or the cyclic elastic energy density, as done in the IDAFIP criteria.

As shown in figure 4.7, the self-heating curves revealed that, for a given stress amplitude and maximum stress in absolute value, the energy density dissipated per cycle is comparable in tension-tension (stress ratio of 0) and in compression-compression (stress ratio of ∞). The dissipated energy density per cycle depends on the stress ratio (figure 4.7). For a given number of cycles to failure, the dissipated energy per cycle is higher for $R_\sigma = \infty$ than for $R_\sigma = 0$, is similar for $R_\sigma = \infty$ and $R_\sigma = 10$, and is lower for $R_\sigma = 3$. The self-heating approach, with an empirical analysis of the self-heating curve, provides a reasonable assessment of the fatigue life for loadings including compression (see figure 4.8). However, the number of cycles to failure is underestimated for lifetimes greater than 10^6 cycles. Furthermore, in accordance with the results mentioned above, the criterion based on the density of energy dissipated per cycle does not permit the effect of the stress ratio to be accounted for in a unified manner. Consequently, the parameters must be identified for each stress ratio.

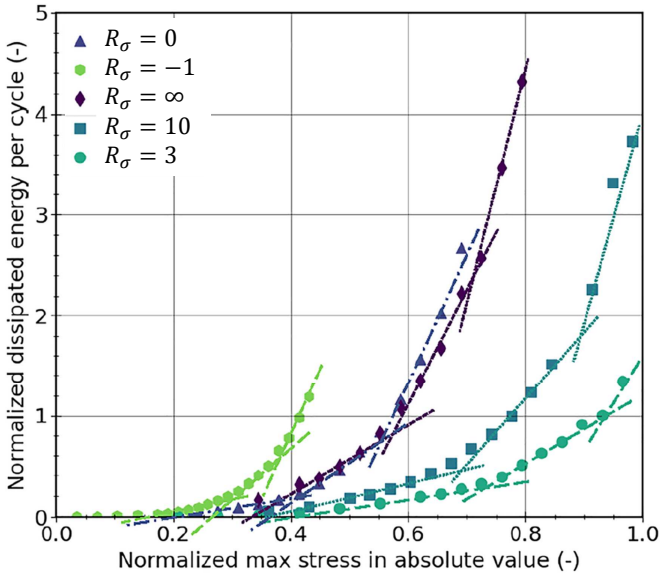

Figure 4.7 – Self-heating curves obtained on PEEK CF30 loaded at room temperature along the injection direction, as a function of the maximum stress in absolute value, for several R_σ; the lines correspond to the three dissipation regimes identified to establish the link between fatigue and dissipation (Kwiatkowski, 2023; Kwiatkowski et al., 2023).

Conclusions: Provided that certain precautions are taken, it is feasible to conduct controlled, cyclic compression tests on samples extracted from plates without anti-buckling device. Fatigue life differs between compression and tension. The IDAFIP fatigue criteria are validated for a material tested at a temperature below the glass transition temperature of the amorphous phase ("glassy" state) and for

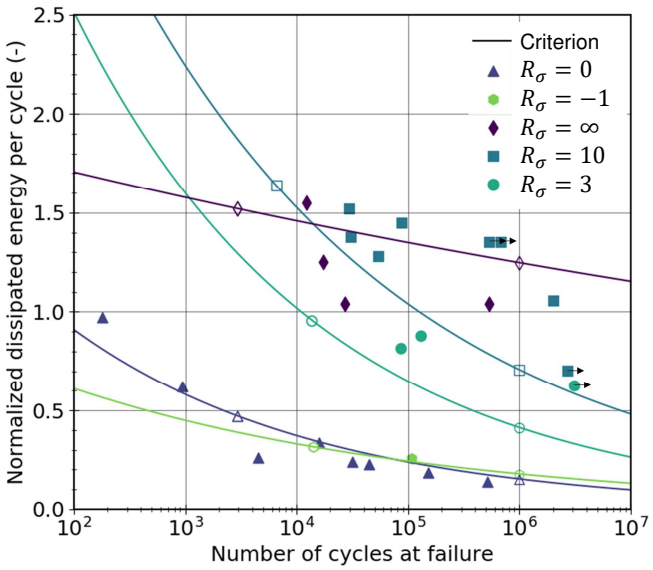

Figure 4.8 – Dissipated energy density per cycle as a function of the number of cycles at failure obtained for PEEK CF30 loaded along the injection direction, at room temperature, for several R_σ: comparison of experimental results (the arrows to the right indicate that the test was stopped before the sample broke) and predictions by the fatigue criterion based on dissipated energy density per cycle with one set of parameters for each stress ratio (the empty symbols correspond to the points used to identify the criterion) (Kwiatkowski, 2023; Kwiatkowski et al., 2023).

cyclic loadings dominated by compression. The self-heating approach enables the fatigue life to be evaluated in a rapid and satisfactory manner, including loads involving compression. The predictions are less reliable for lifetimes exceeding 10^6 cycles with the empirical analysis of the self-heating curves employed. Therefore, it appears necessary to conduct further research and provide a more comprehensive understanding of the self-heating curve.

4.4 Modeling of the cyclic mechanical behavior

Context: In order to design a part against fatigue, it is essential to establish a constitutive model that accurately describes the mechanical behavior of the material under cyclic loading. In particular, this law should be capable of predicting the quantities involved in the fatigue criterion. Furthermore, a behavior law capable of predicting dissipation due to anelastic or inelastic phenomena can be particularly useful for refining the understanding of self-heating curves and the link with fatigue. This would enable to move beyond the empirical analysis, which has been highlighted as having limitations in the previous section. The existing literature lacks models that are capable of describing the complex thermomechanical response of SFRT composites to cyclic loading, and, in particular, of predicting the dissipated energy density, and the energy densities involved in the IDAFIP fatigue criteria (see section 4.2). In addition, the identification of the parameters of the behavior laws developed for SFRTs is often performed by assuming ideal boundary conditions and assimilating the material to a homogeneous material, i.e., the gradient of the fiber orientation distribution along the thickness is not considered. However, the relevance of these simplified representations is questionable when the material is relatively thick and the gauge length of the specimen is relatively short, as in compression testing, for example.

Objectives: We have therefore worked to develop a model describing the mechanical response of SFRT composites to cyclic loading, which is capable of predicting the energy densities mentioned above, for different load ratios and loading directions. The first objective was to construct relevant experimental databases to serve as the foundation for a model. The subsequent objective was to develop a model that can be used in an industrial context to simulate complex parts. The last objective was to propose a robust methodology for identifying the parameters of the model so that it best describes the material's response to the loading conditions of greatest importance. A side objective was to determine the representation of the material and specimens offering the best compromise between accuracy of results and computation time required to perform simulations for identifying the parameters of the behavior law.

This work was essentially initiated during L. Leveuf's PhD thesis [18] (Leveuf, 2017) to describe the behavior of PEEK CF30 under tension at a temperature below

[18] I did not participate in the supervision of this thesis, which was defended before I joined ENSTA Bretagne.

T_g. It was then continued during P. Santharam's PhD thesis (Santharam, 2020) [19] to describe the behavior of PA66 GF50 under a range of humidity and temperature conditions, above T_g. During V. Kwiatkowski's PhD thesis (Kwiatkowski, 2023) [20], further improvements were made to the model and its identification strategy, enabling it to describe the response of a thicker PEEK CF30 material under a range of loading conditions, including compression. This work was the subject of an article published in 2020 (Navrátil et al., 2020) and of a presentation given in 2022 (Kwiatkowski et al., 2022).

Methods: The first step was to build up an experimental database to study the mechanical behavior of the materials in order to formulate a suitable model, identify the material parameters introduced and finally validate the model once it had been identified. Uniaxial tension and/or compression tests were carried out on specimens taken from injected sheets with their gauge length at 0 °, 45 ° or 90 ° to the direction of injection. The distribution of fiber orientations along the plate thickness was characterized by processing images obtained using digital OM and/or µ-CT. The tensile tests were carried out on specimens designated as "full" of the original plates thickness (ranging from 3 mm to 5 mm, depending on the study) with a gradient of fiber distribution through the thickness (see figure 4.1 for example), and specimens designated as "skin" (with a thickness of about 1 mm) obtained from the skin of the full specimens with a "homogeneous" microstructure. The compression tests were carried out on full specimens only to avoid buckling. The tests were conducted using a variety of loading histories in order to determine the different components of the material's mechanical behavior, including monotonic tests at various loading rates, anhysteretic tests [21], cyclic creep-recovery tests [22], and cyclic tests. The cyclic tests were performed with a sinusoidal loading at a frequency typically between 1 and 5 Hz, or between 0.01 Hz and 1000 Hz (dynamic mechanical analysis) in one case, with different stress levels and several R_σ in tension-tension (between 0 and 0.7), tension-compression (between -1 and -0.2) and compression-compression (between 3 and ∞), depending on the study. During all tests excluding dynamic mechanical analysis, the deformation of the specimens was measured by DIC. In addition, during the cyclic tests carried out on PEEK CF30, the temperature of the samples was measured using an IR camera to determine the cyclic dissipation.

Based on the results obtained, a model was formulated in a thermodynamic framework to describe the behavior of the material. The model is based on a hybrid approach combining micromechanical modeling (mean-field homogenization) of elasticity and macromechanical modeling of the inelastic response, in order to combine the advantages of the two approaches [23]. The various components of the behavior

[19] Some of the work described in this thesis has already been presented in section 4.2.

[20] This thesis has already been introduced in section 4.3.

[21] The test consists of applying a series of creep stages at increasing stress level followed by a series of creep stages at decreasing stress level.

[22] The test involves the application of creep stages at several increasing and then decreasing stress levels, with a recovery period at zero stress between each stage; each creep-recovery step is repeated twice.

[23] In particular, the micromechanical approach offers a natural description of the macroscopic

law were identified in a sequential order, one after the other. Several identification procedures have been examined.

Results: The results indicated that the two materials under investigation exhibit anisotropic elasticity, anisotropic plasticity with non-linear kinematic hardening, and non-linear viscoelasticity related to plastic hardening. Linear elasticity was described as a function of the fiber volume fraction, aspect ratio and orientation distribution (via the second-order fiber orientation tensor; see figure 4.1), using a two-step homogenization method. The anisotropic plasticity with non-linear kinematic hardening was described using a phenomenological model that considers the fiber orientation distribution (via a Hill-like tensor expressed as a function of the second-order fiber orientation tensor). A phenomenological model was proposed to describe viscoelasticity, which is assumed to be related to kinematic hardening. The model was implemented numerically [24] in such a way that it can be used for FE simulations.

The results of the simulations indicated that simplifying the boundary conditions to represent the tests for identification has a second-order effect. Conversely, considering the gradient of fiber orientation distribution along the thickness has a non-negligible effect when the material is relatively thick (e.g., 5 mm). Consequently, the parameters of the model were identified through calculations performed on an equivalent material point when homogeneous samples were used, or through FE simulations considering the fiber orientation gradient when present. The first identification strategy proposed involved using solely the results from monotonic and cyclic creep-recovery tests (see example shown in figure 4.9) performed on samples oriented at 0 ° and 90 ° from the injection direction. In the case of PEEK CF30 loaded in tension at room temperature (below T_g), the model identified in this manner is capable of describing the cyclic mechanical behavior of the material (including cyclic dissipation). This is not the case for PEEK CF30 in compression, where the stress levels reached are higher and the non-linearities are therefore greater. This is also not the case for PA66 GF50 loaded at temperatures above T_g, where the non-linearities are further exacerbated. This is partially due to the fact that the characteristic times that are most frequently activated during the cyclic creep recovery tests are lower than those activated during the cyclic tests. Consequently, we proposed the inclusion of some cyclic tests in the identification database. To assess the validity of the identified model, it is applied to simulate anhysteretic tests and cyclic tests with other load ratios, and the predictions are compared with experimental data. As illustrated in figures 4.10 and 4.11, the results demonstrated that the law provides a satisfactory description of the material's cyclic mechanical response under different load directions and load ratios. However, while this is not a major problem in the present case given that the application essentially involves cyclic loading, the current model still presents a significant challenge in accurately describing both cyclic tests and tests with phases during which loading remains

response of the material, taking into account certain microstructural elements, with minimal effort to identify the parameters; the macromechanical approach provides high computation efficiency.

[24] The implementation was conducted using the `TFEL/MFront` code generator.

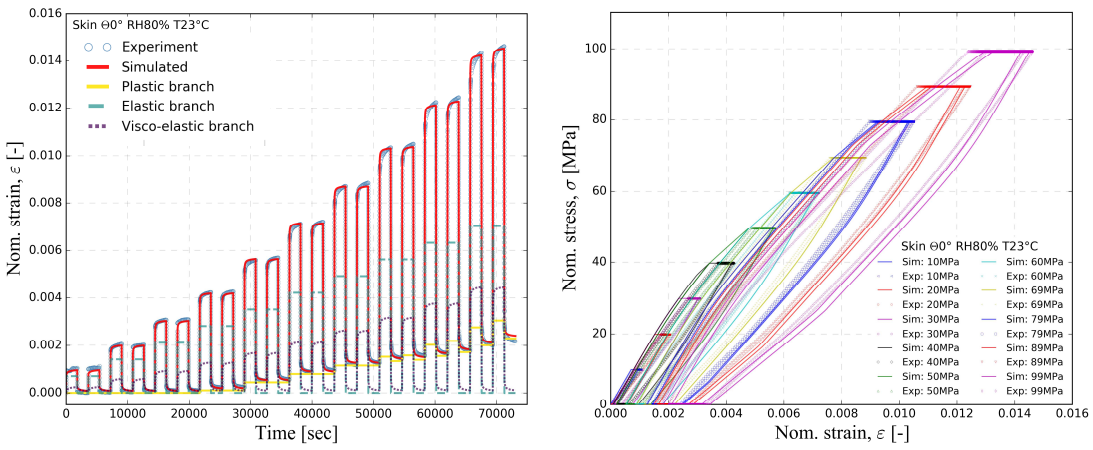

(a) (b)

Figure 4.9 – Comparison of experimental results and results from calculations using the model identified, for a load-controlled cyclic creep-recovery test performed on a skin sample of PA66 GF50 for $RH = 80\%$ and $T = 23\,^{\circ}\mathrm{C}$: (a) nominal strain as a function of time (with the proportions of elastic, viscoelastic and plastic strains predicted by the model); (b) nominal stress-strain curves (Santharam, 2020).

constant (e.g., creep, relaxation or recovery).

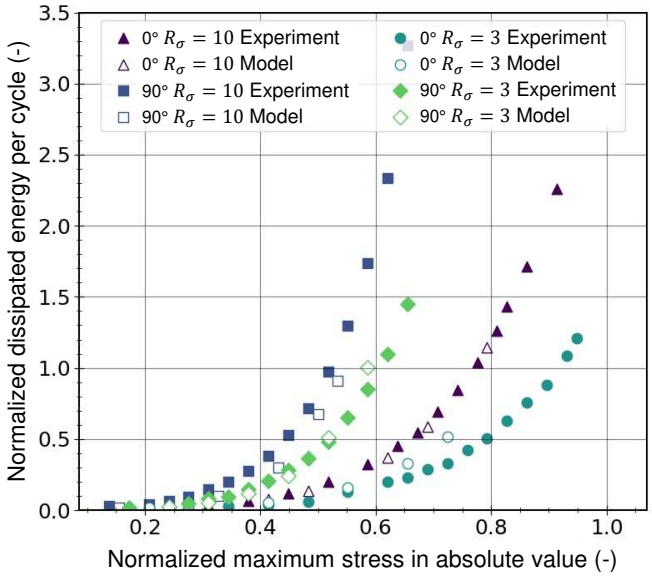

Figure 4.10 – Self-heating curves obtained experimentally and calculated with the model for PEEK CF30 loaded at room temperature, at 0 ° or 90 ° from the injection direction, with a stress ratio of 10 or 3 (Kwiatkowski, 2023).

Conclusions: Ignoring the through-thickness gradient of fiber orientation dis-

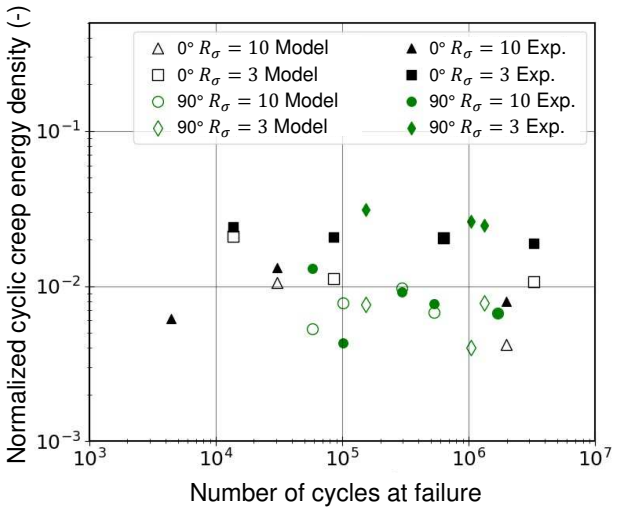

Figure 4.11 – Cyclic creep energy density (average between 5th and 10th cycles) obtained experimentally and calculated with the model, as a function of the experimental number of cycles to failure, for PEEK CF30 loaded at room temperature, at 0 ° or 90 ° from the injection direction, with a stress ratio of 10 or 3 (Kwiatkowski, 2023).

tribution and considering an average fiber orientation tensor, as is often done in literature, can introduce significant errors in some cases. With appropriate experimental database and identification protocol, the model developed is capable of accurately describing the cyclic mechanical behavior of SFRTs, below and beyond T_g. The model currently demonstrates a satisfactory level of accuracy in predicting the quantities involved in the IDAFIP criterion. However, it was found that a small deviation in the prediction of the quantities involved in the criteria could have a significant effect on the prediction of fatigue life. Consequently, the model must be further refined. In particular, the description of ratcheting involved in the cyclic creep energy density used in the IDAFIP fatigue criterion is subject to improvement, particularly for large numbers of cycles. The analysis of the dissipation predicted by the model when simulating self-heating tests leads to the conclusion that the transition between the first and the second regimes of self-heating (see figure 4.7), assumed to correspond to a given lifetime, 10^6–10^7 cycles typically, is linked to the activation of plasticity and its effect on viscoelasticity in the case of tensile loading, as shown in figure 4.12. In contrast, for compressive loading, the stress levels required to achieve a fatigue life of 10^6–10^7 cycles are significantly higher than those at which plasticity is initiated. Thus, the correlation between dissipative mechanisms and fatigue life does not appear to be the same in tension and compression. This remains to be clarified. In particular, a detailed examination of damage was initiated.

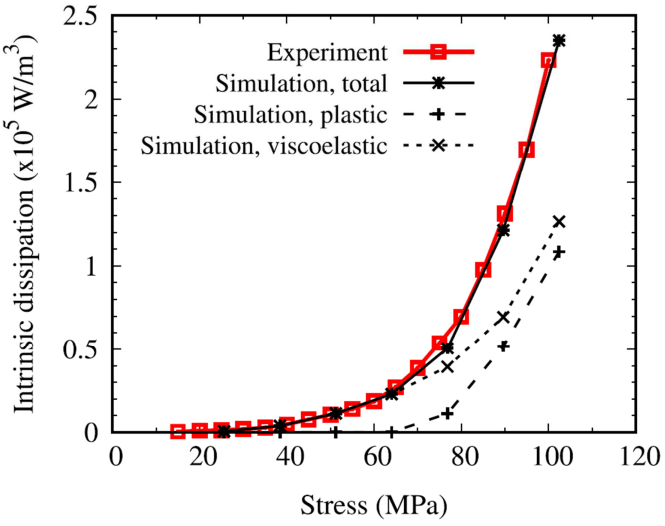

Figure 4.12 – Self-heating curves, as a function of the stress amplitude, obtained experimentally and calculated with the model (the contributions of plasticity and viscoelasticity to the total dissipated energy density per cycle are represented) for PEEK CF30 loaded at room temperature, along the injection direction, with $R_\sigma = 0$ (Navrátil et al., 2020).

Chapter 5

Fatigue of thermoset composite laminates under compression

Context: Thermoset matrix continuous fiber-reinforced composite laminates are employed in a multitude of industrial sectors. In certain applications, such as aeronautics, the material is subjected to cyclic compressive loading in a direction perpendicular to the ply stacking direction, and must withstand several million or tens of millions of cycles (very high cycle fatigue). The fatigue of laminates has been the subject of numerous studies, yet few have focused on fatigue under compression-compression loading. In particular, there is a lack of information on failure mechanisms. In addition, as for SFRTs (chapter 4), fatigue tests on thermoset composite laminates can only be carried out at frequencies limited to a few hertz to avoid excessive self-heating. The characterization of fatigue for very long lifetimes is therefore complicated. It is also important to note that some composite laminates exhibit an endurance limit (or fatigue limit), or at least a stress below which failure does not occur for a very large number of cycles, typically 10^7–10^8 cycles. Approaches based on self-heating measurements have been successfully applied to a variety of materials to reduce the duration of fatigue characterization campaigns, but very few studies have been performed on composite laminates. Moreover, for polymer-based materials, as previously discussed in chapter 4, the analysis of the self-heating curve and the establishment of a correlation with fatigue life are often conducted empirically. Lastly, for laminates, it is currently difficult to determine the dispersion of fatigue life from self-heating curves [1]. One method for reducing the number of tests required to construct a fatigue curve, and possibly the associated dispersion, is to utilize a model based on residual strength degradation (such as the one proposed by Sendeckyj) when the underlying assumptions are met [2]. Nevertheless, in order

[1] In order to assess the dispersion of fatigue life from self-heating data, it is necessary to have a comprehensive understanding of the mechanisms underlying dissipation and their correlation with fatigue life, accompanied by probabilistic modeling of the phenomena. However, in the case of organic composite materials, including laminates, this is a particularly complex undertaking.

[2] These models are based on the several assumptions, in particular: damage induced by cyclic loading leads to a reduction in residual strength; fatigue failure occurs when the residual strength

to identify the model parameters, it is still necessary to perform a number of fatigue tests over a range of lifetimes that covers the range of interest. This can be a time-consuming process, particularly when the concern is very high cycle fatigue and when the material shows an endurance limit.

Objectives: As part of O. Zimmermann de Almeida's PhD thesis [3], we studied the fatigue of a carbon fiber/epoxy resin laminate under cyclic compressive loading. The preliminary objective was to establish a protocol for conducting cyclic compression tests without premature buckling, with the capability of measuring kinematic and/or thermal fields. Subsequently, the objective was to investigate the fatigue under compression-compression up to very high number of cycles, and to identify the failure mechanisms. Another objective was to propose a method for rapidly assessing the endurance limit based on the self-heating curve. The last objective was to investigate the potential for assessing the stress versus number of cycles curve, including the associated dispersion, through the use of an approach based on residual strength. This work was the subject of an article accepted for publication in 2024 (Zimmermann de Almeida et al., 2025).

Methods: This work was carried out on a 6.6 mm-thick quasi-isotropic [4] laminate consisting of 48 plies of unidirectional carbon fibers and epoxy matrix. As with the tests on SFRT composites described in section 4.3, the compression tests were conducted without the use of an anti-buckling device. The free length of the specimen was optimized. In addition to the initial alignment of the jaws and specimen, it was observed that it is crucial for the machine to be sufficiently rigid and capable of blocking the rotation of the jaws to prevent buckling during the test. Compression tests were carried out at ambient temperature and humidity, i.e., at a temperature well below the T_g of the epoxy used (beyond 150 °C). They include monotonic tests, and fatigue tests with a stress ratio $R_\sigma = 10$ at frequencies of 2 Hz and 4 Hz. The fatigue lifetimes investigated range from a few dozen cycles to 10^8 cycles. To identify the failure mechanisms, fatigue tests were interrupted before failure and the samples were observed using SEM and CT.

Self-heating tests were performed using the same stress ratio and frequency, with temperature field measurement using an IR camera. The spatial average of the energy density dissipated per cycle was determined from the average rate of temperature increase during the first cycles (transient approach, adiabatic regime) or from the average stabilized temperature increase after a few thousand cycles (steady-state regime approach). A constitutive law describing the viscoelastic behavior of the laminate plies as a function of their orientation was used to determine the

reaches the maximum cyclic stress applied; the mechanisms responsible for dispersion are the same under monotonic and cyclic loading; and the equivalent static (monotonous loading) strength is described by a probability density function (e.g., Weibull).

[3] This thesis began in 2022. It is carried out within the framework of a CIFRE contract with Safran Composites with the financial support of ANRT, as part of the "Self-Heating" ANR-Safran-Naval Group research chair involving Safran Companies, Naval Group, ENSTA Bretagne (IRDL), and Institut Pprime.

[4] The material consists of a balanced and symmetric stacking of unidirectional plies with different orientations, typically 0 °, 90 ° and ±45 °.

contribution of plies to the measured average dissipation. To estimate the endurance limit from the self-heating curve, the average cyclic dissipation obtained from the measurements was compared with the dissipation expected for a linear viscoelastic behavior at the laminate scale.

Finally, the results of monotonic and fatigue tests carried out until failure and the endurance limit deduced from the self-heating curve were used to identify a fatigue criterion based on residual strength.

Results: As shown in figure 5.1, the results of the fatigue tests suggested the existence of an endurance limit. The observations made after interrupting fatigue tests showed that the cracks initiate in the plies where the fibers are oriented at 45 ° to the loading direction and propagate in neighboring plies oriented at 0 °, causing complete failure of the laminate.

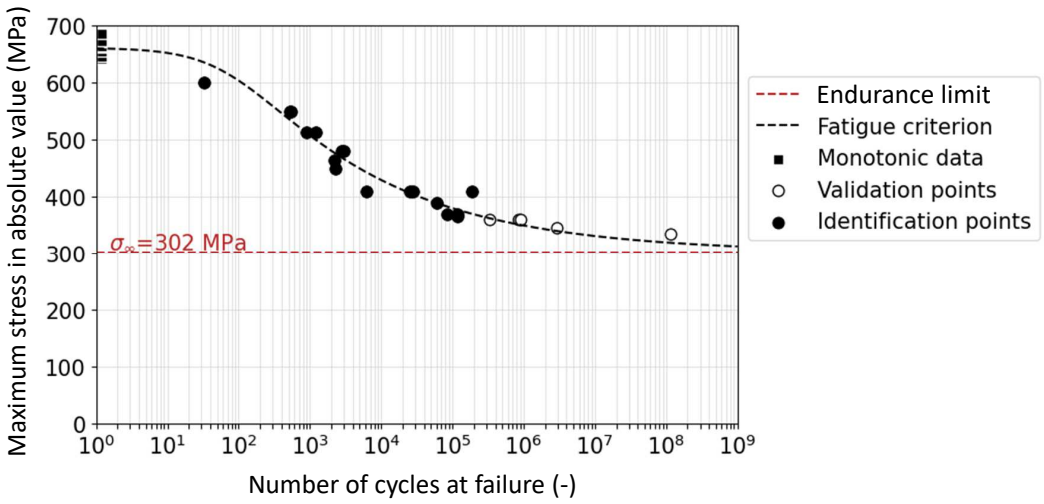

Figure 5.1 – Results of monotonic tests in compression and fatigue tests in compression-compression with $R_\sigma = 10$ at frequencies of 2 Hz and 4 Hz, performed at room temperature on a quasi-isotropic carbon/epoxy laminate; comparison with the predictions of the criterion based on residual strength and the endurance limit estimated from the self-heating curve (Zimmermann de Almeida et al., 2025).

The various self-heating tests performed have shown that the average dissipative behavior of the laminate volume can be calculated from surface measurements of temperature variation, including using a transient approach (figure 5.2). According to the dissipation calculated with a viscoelastic model at the ply scale, the average measured dissipation is mainly due to dissipation in plies oriented at 45 °. As shown in figure 5.2, the observed dependence of the cyclic dissipation on the applied stress level corresponds to that expected for a linear viscoelastic behavior below a certain stress level. Beyond this level, the dissipation measured is higher than that which would be expected for this type of behavior. It is assumed that new dissipation mechanisms are activated, which are likely to be associated with damage that could result in failure of the laminate. Therefore, it is suggested that this stress level be

considered as the endurance limit of the material. As shown in figure 5.1, the stress value obtained is consistent with fatigue data. Once identified, the model based on residual strength provides a relatively accurate description of the stress versus number of cycles curve of the laminate and the associated dispersion.

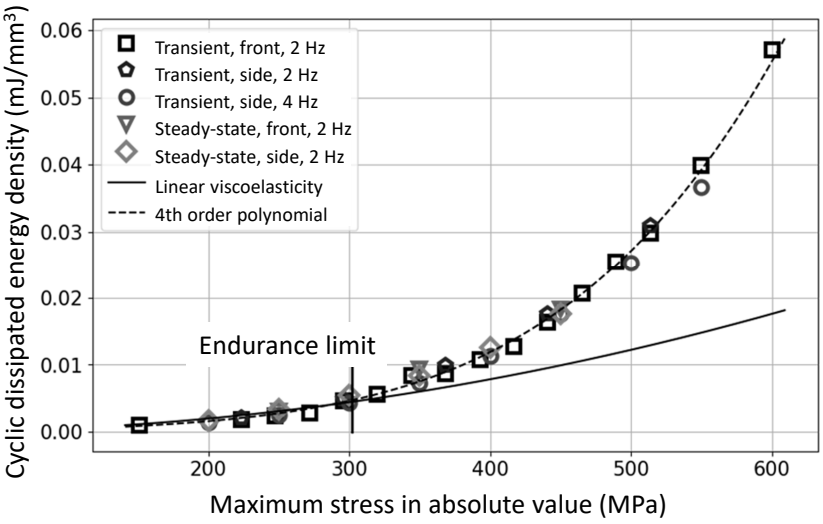

Figure 5.2 – Self-heating curves obtained using a transient/adiabatic approach and a steady-state approach, from temperature measurements performed on the sample's front surface and side surface, on a quasi-isotropic carbon/epoxy laminate loaded at room temperature in compression-compression with $R_\sigma = 10$ and frequencies of 2 Hz and 4 Hz; comparison to the energy density dissipated per cycle predicted for a linear viscoelastic behavior, and endurance limit deduced from the comparison (Zimmermann de Almeida et al., 2025).

Conclusions: The damage mechanisms and kinetics of quasi-isotropic laminates under compression-compression loading are different from those observed under tension-tension or tension-compression loading. The proposed methodology, based on a linear viscoelastic model, enables the endurance limit to be estimated with great rapidity, from a self-heating test that lasts for less than a day. By combining this approach with a residual strength approach, it is possible to determine a stress versus number of cycles curve and the associated dispersion using only a few static tests, a few low-cycle fatigue tests, and a self-heating curve.

Chapter 6

Microstructure and mechanical behavior of elastomer foams

Contents

6.1 Microstructure

Context: Microcellular polyurethane (MCU) foams are versatile materials that find application in a range of industrial contexts. Their effective properties are closely related to their cellular microstructure, which is influenced by the ingredients and the process used to elaborate the part. For instance, the mechanical behavior of the material depends on the volume fraction, size, shape, orientation or spatial distribution of the cells. The acquisition of quantitative data on the microstructure is therefore of significant importance for a number of contexts, including, for example, process control and the understanding of the material's effective physical properties throughout numerical simulations. SEM is a commonly used technique for observing the microstructure of polymer foams. This technique offers a very good spatial resolution, but it also has some drawbacks. It is destructive and surface preparation is challenging for soft materials. Additionally, the observed area is limited, requiring the acquisition of multiple images to obtain a representative view of the microstructure, which may introduce bias. Furthermore, the segmentation of images obtained with this technique to separate the cells from the matrix and the cells from each other is not a straightforward process [1]. Finally, it provides a 2D view of the microstructure. µ-CT is particularly well-suited to the characterization

[1] In the literature, SEM images are often used qualitatively and not processed to extract quantitative data. When they are, processing is either manual or not fully automatic, requiring the user to possess sufficient image processing skills to obtain satisfactory segmentation.

of the microstructure of cellular materials at the cellular scale. It provides a distinct contrast between the interior of the cells and the surrounding matrix. It can analyze large volumes of material without the need for extensive sample preparation. The technique yields 3D information. Nevertheless, this technique may lack spatial resolution [2]. Furthermore, it is less common than SEM, particularly in industrial laboratories. Image segmentation to separate the cells from the matrix is often performed using conventional thresholding algorithms. These algorithms are not always suitable, and generally do not enable automatic, robust and objective segmentation.

Objectives: We have worked on the development of protocols for the quantitative characterization of the cellular microstructure of MCU from µ-CT and SEM images. A specific aim was to develop robust image processing procedures for automatically segmenting the images. An additional objective was to ascertain the extent to which the information derived from surface observations (without applying 2D to 3D transformation using stereological methods) is indicative of the 3D microstructure. Furthermore, we investigated the potential for SEM images to be used to characterize the cellular microstructure of MCUs in a quantitative, automatic (for routine use, even by a user with limited knowledge of image processing), objective (to limit operator influence on the results), robust (with minimal sensitivity to sample preparation and operator influence), and efficient (enabling integration into industrial processes such as quality control) manner. This work was published in 2023 (Le Saux et al., 2023).

Methods: Samples of elastomer MCU, with densities between 400 $\mathrm{kg{\cdot}m^{-3}}$ and 600 $\mathrm{kg{\cdot}m^{-3}}$ and differing microstructures, were subjected to examination by SEM (pixel size: $0.6 \times 0.6\,\mathrm{mm^2}$) and µ-CT (voxel size: $5.8 \times 5.8 \times 5.8\,\mathrm{mm^3}$). Robust image processing techniques have been developed [3] to automate image segmentation with the goal of separating the cells from the matrix and from each other. Several indicators of cell size, shape, orientation, and spatial distribution were determined. The results of 3D analysis of µ-CT images, 2D analysis of µ-CT slices, and 2D analysis of SEM images were compared.

Results: As shown in figures 6.1 and 6.2, the robust image processing procedures implemented permit the automatic segmentation of images, even those captured by SEM, which are relatively challenging to segment due to the highly variable appearance of the cells. Nevertheless, automatic image segmentation is less accurate for SEM images compared with µ-CT images. It has been observed that in order for the results to be statistically representative, it is necessary to analyze a considerable number of cells (several thousand cells, typically). It is therefore essential that the image segmentation be carried out automatically. The results indicated that the cells are predominantly connected to at least one other cell, exhibit a size range that varies across the sample, and are typically between a few micrometers and several hundred micrometers in diameter (see figure 6.3). They tend to be relatively

[2] The resolution depends on the size of the sample or the µ-CT system characteristics.

[3] Open-source `Python` algorithms have been used, as also done to detect inclusions in dense elastomers (Glanowski et al., 2023), and to separate the various components and damage in textile fiber-reinforced rubber (Klauke et al., 2024).

spherical and rounded, with no apparent preferred orientation, and are often grouped by size class. On the one hand, 2D analysis can provide a reliable estimation of the cell volume fraction and a satisfactory evaluation of the cell size distribution. On the other hand, 2D analysis does not provide a precise quantitative description of cell shape and spatial distribution in 3D. In the case of SEM images, the evaluation is further degraded by segmentation error.

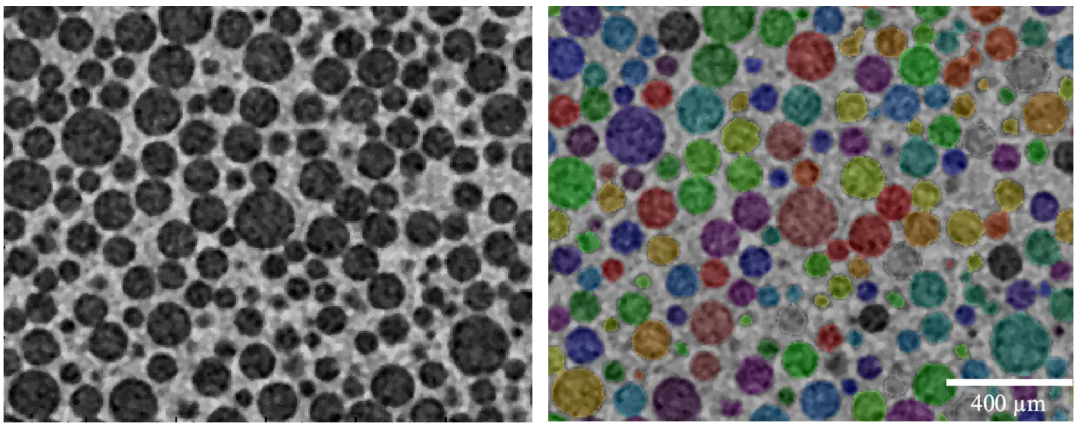

(a) (b)

Figure 6.1 – (a) Portion of a µ-CT image obtained on a MCU sample with a density of approximately 500 kg·m^{-3}; (b) same image with the cells detected using automatic segmentation painted in color (Le Saux et al., 2023).

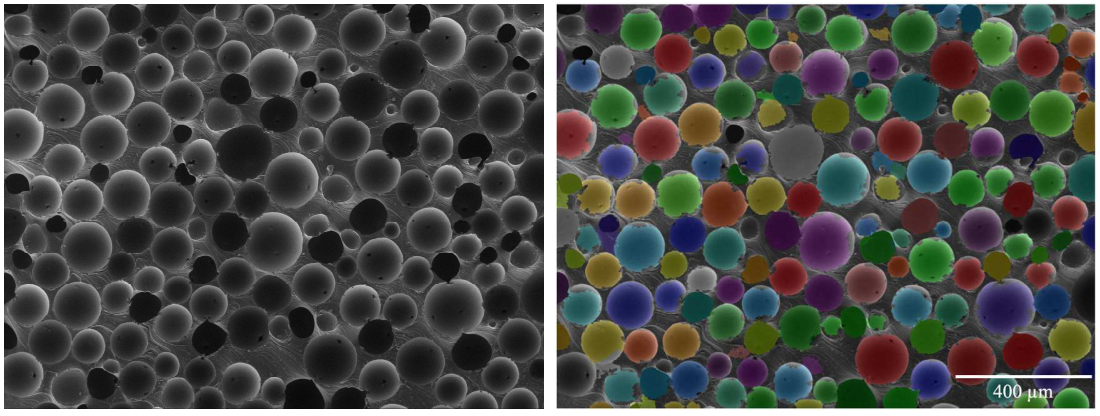

(a) (b)

Figure 6.2 – (a) SEM image obtained on a MCU sample with a density of approximately 500 kg·m^{-3}; (b) same image with the cells detected using automatic segmentation painted in color (Le Saux et al., 2023).

Conclusions: It was concluded that 3D analysis of µ-CT images remains the optimal method for quantitatively and precisely characterizing the microstructure of microcellular polymer foams. Nevertheless, SEM combined with an appropriate automatic image processing method can provide relevant information about the mi-

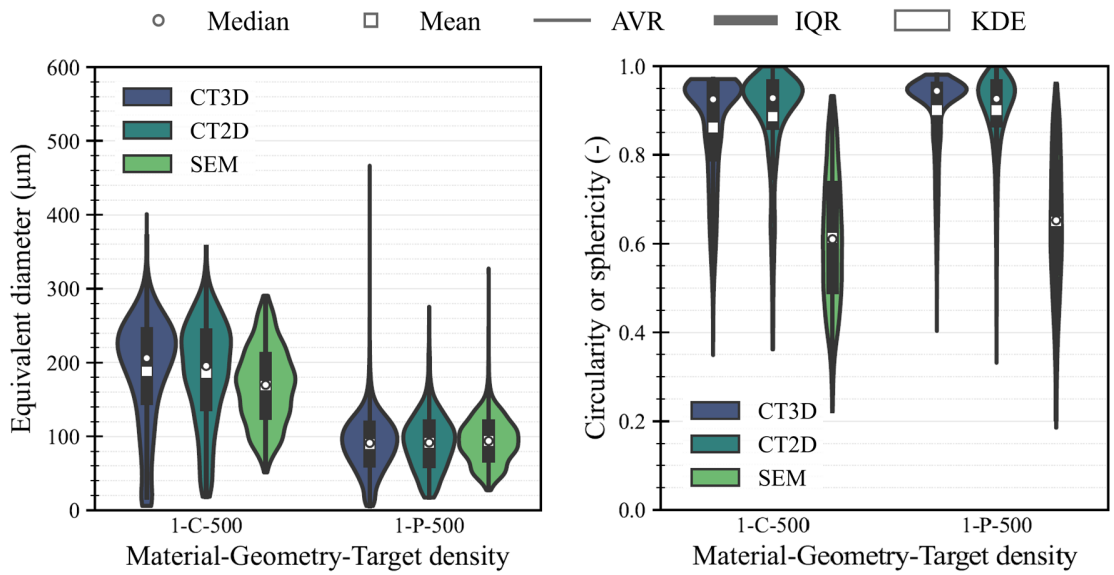

(a) (b)

Figure 6.3 – Distribution of (a) equivalent diameter and (b) circularity (in 2D) and sphericity (in 3D) of the cells according to 3D analysis of µ-CT images (CT3D), 2D analysis of one µ-CT slice image (CT2D), and 2D analysis of SEM images (SEM), for two MCU samples with a density of approximately 500 $kg{\cdot}m^{-3}$ (1-C-500 and 1-P-500); AVR represents the adjacent value range, IQR the interquartile range, and KDE the kernel density estimate (Le Saux et al., 2023).

crostructure relatively easily and quickly. This may be sufficient to conduct comparative qualitative studies (to compare materials, or for quality control in production, for example). Additionally, it is worth noting that the data obtained can be used to generate microstructures for the purpose of numerical simulations.

6.2 Mechanical behavior

Context: In certain applications, such as jounce bumpers in automotive suspension, MCU is subjected to intense multiaxial, compression-dominated mechanical loading, resulting in significant deformation and volume variations, typically in the range of several tens of percent. The mechanical design of such parts is frequently based on FE simulations. These simulations necessitate the development of a constitutive model that accurately describes the mechanical behavior of the material within the loading range of interest. MCU exhibits complex mechanical behavior, including highly non-linear compressible elasticity. Moreover, this behavior depends on the density of the material or, in other words, the porosity fraction. Therefore, there is a need for a constitutive law that reflects this dependence. Indeed, the initial density of the foam [4] may vary between different parts or within the same part.

The majority of studies investigating the mechanical behavior of elastomer MCU and the effect of foam density are based on the results of a limited number of types of tests, often one or two, among uniaxial tension, uniaxial compression, confined compression and simple shear tests. This provides only a partial characterization of the material's behavior, and is probably not sufficient to determine the material's response to multiaxial loading. Moreover, there are few hydrostatic compression tests on elastomeric foams in the literature. The devices used are either complex to set up or do not allow for hydrostatic pressures of several megapascals to be applied or for volume variations of several tens of percent to be achieved. In addition, when pressure is applied to the sample via a fluid, it is challenging to prevent penetration of the fluid into the foam, particularly when it is open-cell. Last but not least, the majority of the constitutive models proposed in the literature are unable to accurately represent the highly non-linear, compressible, elastic behavior of elastomer MCU over a range of loading modes and levels as wide as that of interest here, and/or are too computationally demanding to be used in an industrial context.

Objectives: During J. Becker's PhD thesis [5], we worked on developing a constitutive model that describes the highly non-linear compressible elasticity of elastomer MCU [6] over a wide range of loading modes and loading levels, and its dependence

[4] Foam density is related to the density of the parent solid material and the volume fraction of porosity.

[5] This thesis began in 2022. It is carried out within the framework of a CIFRE contract with Vibracoustic with the financial support of the french ANRT.

[6] The mechanical response of this type of material also exhibits other components, including cyclic softening and time-dependency. Nevertheless, the description of these phenomena is not a primary concern in the context of the intended application.

on the initial density of the material. Firstly, the objective was to construct a comprehensive experimental database on the mechanical behavior of the material, incorporating tests leading to different loading modes. One objective was the development of a hydrostatic compression test for polymeric foams that would overcome the limitations of the existing tests. Secondly, the objective was to propose, identify and validate a model that could accurately describe the behavior of the material while maintaining a sufficiently low numerical cost to be used efficiently for the simulation of complex parts. These works were published in 2022 (Becker et al., 2022) and 2024 (Becker et al., 2024a, b).

Methods: The study was conducted on samples of elastomer MCUs [7] of the same type as those presented in section 6.1, with different densities ranging from 380 $kg{\cdot}m^{-3}$ to 600 $kg{\cdot}m^{-3}$. An original test, called Sphere foam in rubber (SFIR), was developed with the objective of characterizing the response of polymeric foams under near-hydrostatic compression (Becker et al., 2024b): as illustrated in figure 6.4, a cylinder of a nearly incompressible material is molded around a spherical sample of the foam of interest. The entire assembly is then subjected to confined compression in a rigid chamber. A post-processing procedure was developed based on FE analysis to determine the hydrostatic stress in the foam and its volume ratio from the axial load and displacement data measured.

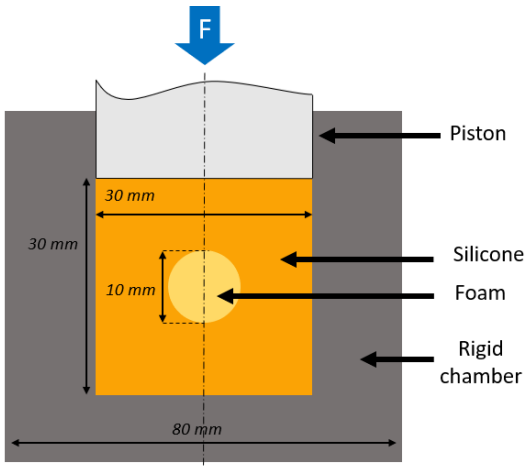

Figure 6.4 – Schematic representation of a section of the axisymmetric experimental setup developed to apply hydrostatic compression to a spherical foam sample (SFIR test) (Becker et al., 2024b).

A series of tests was conducted at room temperature up to strain levels of several tens of percent, including uniaxial tensile tests, uniaxial compression tests, simple shear tests, confined compression tests, and hydrostatic compression tests (Becker et al., 2024a). A phenomenological isotropic [8], hyperelastic-type constitutive model, which has been recently proposed in the literature, has been selected for the purpose

[7] The foams studied are flexible, non-crushable, with no strain localization at the macroscale.

[8] It is assumed that the material's behavior is isotropic, given its microstructure (see section 6.1).

of describing the non-linear compressible elastic response of the material. This model is based on three invariants of the Hencky strain tensor, which are respectively associated to volume change, amplitude of distortion and mode of distortion. The model includes an explicit coupling between volumetric and distortion responses. A sequential identification strategy has been formulated based on the results of the various tests conducted [9]. To validate the identification, compression tests were conducted on jounce bumpers with different material densities [10]. The deformation of the jounce bumper under load was analyzed using CT. A FE model of the test, using the identified behavior law, was developed. The calculated load-displacement response and the deformed shape of the jounce bumper were then compared with the experimental observations.

Results: FE simulations of the SFIR test indicate that the foam sample is subjected to a stress state close to hydrostatic compression. As shown in figure 6.5, the results of the various tests conducted demonstrated that the material exhibits a strongly non-linear compressible elastic behavior, with notable dependence on its initial density. The higher the density, the greater the apparent stiffness and the smaller the change in volume at which densification [11] occurs. The proposed methodology facilitated the robust and reliable identification of model parameters and the assessment of their dependence on density. The model identified provides a relatively accurate description of the material's response to the various elementary tests, as a function of the initial density of the material, over the large range of deformations investigated (see figure 6.5). As illustrated in figure 6.6, the simulations conducted with the model correctly reproduce the experimentally measured load-displacement response and deformation of the jounce bumper under compression.

Conclusions: The SFIR test enables the characterization of any type of highly compressible polymer foam [12] in quasi-hydrostatic compression, up to hydrostatic stress levels of the order of several megapascals and volume reductions in the range of several tens of percent. The proposed solution is readily implementable with standard equipment.

The model, when used in conjunction with the proposed identification procedure based on a large database including five different types of elementary tests, provides a more accurate description of the non-linear compressible elastic response of MCUs and the material density dependence than most other models. With limited computational complexity, the model allows the numerical simulation of complex structures where the material is subjected to heterogeneous multiaxial mechanical loading resulting in significant strains and volume variations.

[9] The load response subsequent to three load-unload cycles, i.e., following cyclic softening, was considered.

[10] During these tests, the height of the jounce bumper was reduced by up to 70%.

[11] Densification corresponds to a drastic increase in apparent stiffness, when most cells are closed.

[12] Nevertheless, the bulk modulus of the foam must be at least a hundred times lower than that of the surrounding, nearly incompressible material.

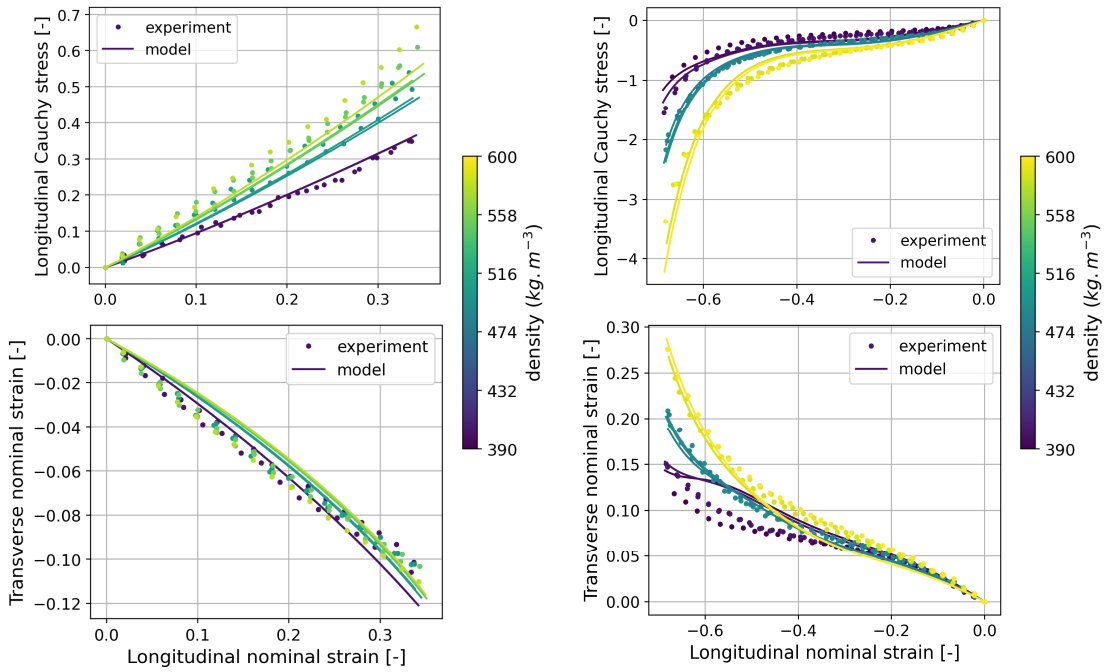

(a) Uniaxial tension

(b) Uniaxial compression

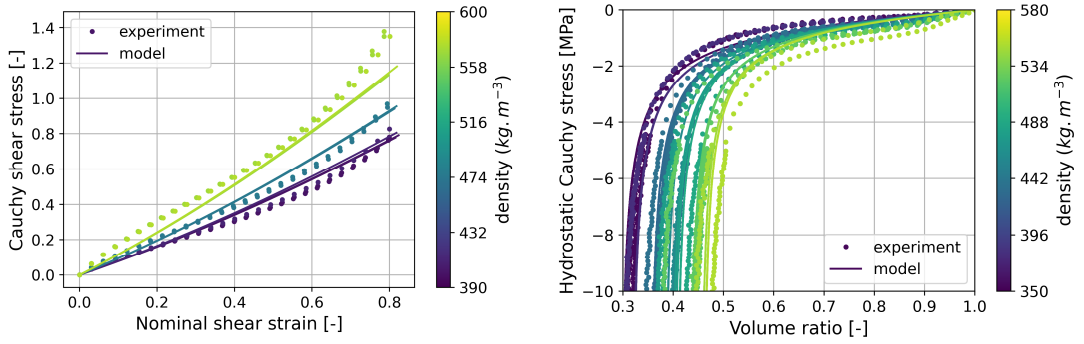

(c) Simple shear

(c) Hydrostatic compression

Figure 6.5 – Comparison of (normalized) responses obtained experimentally and calculated with the model for (a) uniaxial tension (longitudinal stress on the top figure, transverse strain on the bottom one), (b) uniaxial compression (longitudinal stress on the top figure, transverse strain on the bottom one), (c) simple shear and (d) hydrostatic compression tests performed on elastomer MCU samples of different initial densities (Becker et al., 2024a).

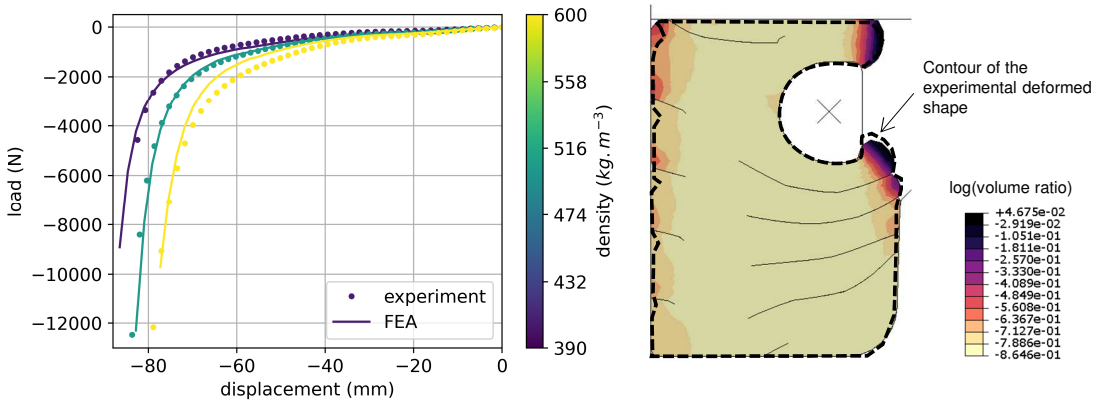

(a) (b)

Figure 6.6 – Comparison of results obtained experimentally and calculated by FE analysis for compression tests performed on jounce bumpers in elastomer MCU: (a) load-displacement curves obtained for three initial material densities; (c) deformed shape (along with the calculated field of the logarithm of the ratio between the current volume and the initial volume of the material) obtained for a material density of about $500\,\mathrm{kg{\cdot}m^{-3}}$ (Becker et al., 2024a).

Summary and perspectives

Summary

This dissertation offered an overview of the main published research activities in which I have participated since the defense of my PhD thesis. My research work has revolved around various issues. However, there are at least three common denominators that hold the patchwork together:

The domain: my research activities focus on the *behavior of heterogeneous materials* whose macroscopic response is strongly related to heterogeneities. These heterogeneities may be present initially, as in composite materials, or may result from microstructural changes that occur during the service life of the material, as is the case with HT oxidized zirconium alloys. Furthermore, my research activities are systematically related, to varying degrees, to the *mechanical behavior* of these materials.

The purpose: the research I conduct is applied in nature. The majority of my work is carried out in collaboration with industrial companies, with the general objective of providing three key elements to help in implementing processes for designing structural parts:

- *understanding*, for example on the mechanisms at the microstructural level involved in the macroscopic response;
- *methods*, like ad hoc characterization protocols for example;
- *tools*, such as constitutive models and failure criteria.

The ultimate goal is typically to provide solutions that are usable in an industrial context. Therefore, the focus is not necessarily on finding the most complete, accurate, rigorous, or elegant solution (from a scientific perspective), but rather on proposing one that offers a good balance between reliability, robustness, and efficiency. Although the primary aim is to respond to a specific practical problem, we try, as far as possible [13], to propose generic methods and tools that can be adapted to other problems.

The approach: the approach adopted systematically combines *experimental characterization*, *modeling* and *numerical simulation* at different scales; a variety

[13] This may conflict with the desire to provide the most effective method of solving a particular problem.

of techniques have been used [14]:

- HT oxidation, using several facilities with different capacities;
- physicochemical and microstructural characterization, using techniques such as DSC, dilatometry, OM, SEM, (µ-)CT, image processing, EBSD, XRD (using laboratory and synchrotron X-ray sources), neutron diffraction, EPMA, µ-LIBS, and µ-ERDA;
- thermomechanical characterization, using standard or specific mechanical tests, kinematic fields measurement using DIC, temperature fields measurement by means of a IR camera, and AE;
- modeling of the material's response, including the transformation of solid phases and the thermomechanical behavior;
- numerical simulations, using the FE method or a FFT-based homogenization technique.

The integration of testing, modeling, and simulation, along with a multi-scale approach, allows us to validate the relevance of our working hypotheses, gain insight into the phenomena involved, and develop effective methods and tools.

Perspectives

My objective is to pursue a research trajectory that builds upon the work I have been engaged in since 2018 at ENSTA / IRDL. My research activities should continue to focus on the characterization and modeling of the thermomechanical behavior and fatigue of heterogeneous polymer-based materials. I plan to continue using the same approach, combining experimentation, modeling, and numerical simulation. However, I would like to strengthen the multi-scale aspect, without losing sight of the scale of primary interest to industry, which is the macroscopic scale. Indeed, the study of the relationships between material microstructure and constituent properties, and macroscopic response can be an effective means of refining and enhancing the robustness of the designing tools developed. It should provide a basis for justifying or feeding the interpretation of experimental observations on the one hand, and for formulating macroscopic constitutive models and failure criteria on the other. This type of approach has not yet been widely used for the kind of heterogeneous polymer-based materials that we are interested in, or not with the same objectives as we are. In particular, the objective is to develop and more systematically apply methods for:

[14] Of course, I am not an expert in all these techniques. I often call on expert colleagues, particularly for advanced physicochemical and microstructural characterization techniques. Nevertheless, I endeavor to gain a comprehensive understanding of the potential and limitations of these techniques, with the aim of ensuring their judicious application. I have a more advanced level of expertise in characterization, modeling and numerical simulation methods for the thermomechanical behavior of materials.

- quantitatively characterizing the material microstructure at appropriate scales, typically by microscopy [15] or µ-CT [16];
- characterizing the mechanical behavior (often non-linear and time-dependent) of the various constituents of the material through methods such as nano- or micro-indentation [17], with the goal of developing a model to describe this behavior;
- characterizing the thermomechanical response of the material, including observations and measurements of kinematic and/or thermal fields at different scales, for example through in situ testing using techniques such as tomography or microscopy;
- simulating the response of the material at the microstructural scale, employing the FE method and/or FFT-based methods, using microstructures generated from µ-CT images or derived from algorithms.

My research activities over the next four years will primarily be based on the PhD theses that have already started or are in preparation. The following theses are currently in progress:

Fatigue of laminates under compression and out-of-plane loading: In the context of aeronautical applications, this study focuses on the fatigue of carbon fiber/epoxy resin laminates when subjected to in-plane compression-compression loading or out-of-plane loading. This project started in 2022. It is part of O. Zimmermann de Almeida's PhD thesis, carried out in collaboration with Safran Composites (CIFRE contract) and Institut Pprime. Some of the objectives related to fatigue under compression-compression have been presented in chapter 5, along with some of the results obtained to date on this subject. The second part of the study addresses the fatigue of laminates subjected to transverse (interlaminar) shear stresses. Indeed, only a limited number of studies in the existing literature have addressed this subject. The objective is to develop a protocol for characterizing the fatigue life of the material subjected to interlaminar shear and to define a fatigue criterion. The aim is to use temperature field measurements to accelerate the characterization process.

Fatigue of 3D woven composites: This study is concerned with the (very) high cycle fatigue of 3D carbon/epoxy composite materials designed for aeronautical applications. It is being conducted as part of B. Simoes Barini's PhD thesis, initiated in 2024 in collaboration with Safran Composites (CIFRE contract). The principal objective is to establish a correlation between the dissipative mechanisms that cause temperature rise under cyclic loading and the fatigue strength of the material. Ultimately, the goal is to use the self-heating method as a rapid approach for characterizing fatigue. Indeed, the method has rarely

[15] OM and SEM are available at ENSTA / IRDL.
[16] ENSTA / IRDL has recently acquired a X-ray tomograph.
[17] ENSTA / IRDL is equipped with a nano-indenter.

been evaluated for 3D woven composites, and the relationship between dissipative mechanisms [18] and fatigue has not yet been fully understood. The approach is based upon a multi-scale methodology that integrates the use of multiple instruments for experimental characterization, in conjunction with modeling and numerical simulation at the microstructure scale.

Mechanical behavior and fatigue of microcellular elastomer foams: This project addresses the mechanical behavior and the fatigue of elastomer MCU under multiaxial loading, for automotive applications. It is part of J. Becker's PhD thesis, which began in 2022, conducted in collaboration with Vibracoustic (CIFRE contract). The primary objective and findings to date regarding the mechanical behavior have already been presented in chapter 6.2. The second objective is to develop an approach for characterizing the fatigue of the material under conditions relevant to the intended application, which involves multiaxial mechanical loading, and to establish a fatigue criterion. In fact, there is almost no literature on the fatigue of these materials under conditions relevant to the intended application.

Thermomechanical behavior and fatigue of thermoplastic vulcanizates: This study is concerned with the cyclic thermomechanical and fatigue behavior of a thermoplastic vulcanizate for an automotive application, which is composed of polypropylene and dynamically vulcanized ethylene-propylene-diene monomer. This study is part of A. Walle's PhD thesis, which was initiated in 2024 in collaboration with Vibracoustic (CIFRE contract). The first objective is to develop methods for analyzing the microstructure of the material at an appropriate scale in order to explain its macroscopic behavior and establish a link with the elaboration process. A second objective is to establish and apply a protocol for the characterization of the diverse components of the non-linear cyclic mechanical behavior of the material over a wide range of temperatures and loading frequencies. The aim is then to identify a comprehensive model that captures the full complexity of the behavior. A third objective is to establish an approach for characterising the fatigue life of the material and to propose a fatigue criterion. Indeed, the models proposed in the literature describe only a portion of the behavior of these materials, and studies dealing with fatigue are relatively scarce.

Ageing, mechanical behaviour and failure of biopolymers: This work is concerned with the effects of aging in the marine environment and its impact on the mechanical response of biopolymers, such as polybutylene succinate. It is carried out as part of L. Soutif--Cormerais's PhD thesis, which started in 2024, in collaboration with the french research institute for exploitation of the sea [19] (contract between the Carnot MERS institute and the Carnot ARTS institute). The first objective is to develop an experimental characterization approach at different scales to investigate the (heterogeneous) aging process

[18] Dissipative mechanisms have multiple origins in these materials due to their particularly complex microstructure.

[19] IFREMER, "Institut français de recherche pour l'exploitation de la mer" in french.

of biopolymers in a marine environment and its impact on the mechanical behavior and failure of the materials. The second objective is to establish a multi-scale modeling approach with the aim of anticipating the heterogeneous long-term effects of marine aging on the mechanical behavior of the material.

Mechanical behaviour of polymer ropes: The study focuses on the mechanical behavior of polymer ropes designed for anchoring offshore floating wind turbine platforms. It is the subject of T. Armand's PhD thesis, which began in 2024 as part of a European partnership. One of the main objectives is to develop experimental characterization and modeling approaches to account for the effects of construction (number of strands, helix angle, ...) on the overall mechanical response of the rope.

Bibliography

Becker, J., Le Bail, J., Le Saux, M., Le Saux, V., Marco, Y., Mahéo, L., Charrier, P., Hervouet, W. (2024a). Characterization and modelling of the compressible hyperelastic behaviour of polyurethane foams: influence of the density. In: *XIII European Conference on Constitutive Models for Rubbers (ECCMR 2024)*.

Becker, J., Le Bail, J.B., Charrier, P., Le Saux, M., Le Saux, V., Mahéo, L., Marco, Y. (2022). Modelling of the compressible hyperelastic behavior of polyurethane foams : analysis of some models and of the influence of the identification strategy. In: *XII European Conference on Constitutive Models for Rubbers (ECCMR 2022)*, pp. 20–25.

Becker, J., Le Saux, M., Charrier, P., Hervouet, W., Le Saux, V., Mahéo, L., Marco, Y. (2024b). The SFIR test: an innovative hydrostatic compression test to characterize the volumetric behavior of polymeric foams. *Experimental Mechanics* 64, 1407–1422.

Bouayoune, A., Guillou, R., Béchade, J.L., Rouesne, E., Thiaudière, D., Grosseau-Poussard, J.L., Panicaud, B., Le Saux, M. (2023). Study of the evolution of stresses and associated mechanisms in zirconia growing at high temperature on Zircaloy-4 by use of synchrotron radiation. *Corrosion Science* 221, 111328.

Brachet, J.C., Billard, A., Schuster, F., Le Flem, M., Idarraga-Trujillo, I., Le Saux, M., Lomello, F. (2016). Gaines de combustible nucléaire, procédés de fabrication et utilisations contre l'oxydation/hydruration (nuclear fuel claddings, production method thereof and uses of same against oxidation/hydriding). *Patent* WO 2016/042261.

Brachet, J.C., Hamon, D., Le Saux, M., Vandenberghe, V., Toffolon-Masclet, C., Rouesne, E., Urvoy, S., Béchade, J.L., Raepsaet, C., Lacour, J.L., Bayon, G., Ott, F. (2017). Study of secondary hydriding at high temperature in zirconium based nuclear fuel cladding tubes by coupling information from neutron radiography/tomography, electron probe micro analysis, micro elastic recoil detection analysis and laser induced breakdown spectroscopy microprobe. *Journal of Nuclear Materials* 488, 267–286.

Brachet, J.C., Idarraga-Trujillo, I., Le Flem, M., Le Saux, M., Vandenberghe, V., Urvoy, S., Rouesne, E., Guilbert, T., Toffolon-Masclet, C., Tupin, M., Phalippou,

C., Lomello, F., Schuster, F., Billard, A., Velisa, G., Ducros, C., Sanchette, F. (2019). Early studies on Cr-coated Zircaloy-4 as enhanced accident tolerant nuclear fuel claddings for light water reactors. *Journal of Nuclear Materials* 517, 268–285.

Brachet, J.C., Le Saux, M., Bischoff, J., Palancher, H., Chosson, R., Pouillier, E., Guilbert, T., Urvoy, S., Nony, G., Vandenberghe, T., Lequien, A., Miton, C., Bossis, P. (2020a). Evaluation of equivalent cladding reacted parameters of Cr-coated claddings oxidized in steam at 1200 °C in relation with oxygen diffusion/partitioning and post-quench ductility. *Journal of Nuclear Materials* 533, 152106.

Brachet, J.C., Lorrette, C., Michaux, A., Sauder, C., Idarraga-Trujillo, I., Le Saux, M., Le Flem, M., Schuster, F., Billard, A., Monsifrot, E., Torres, E., Rebillat, F., Bischoff, J., Ambard, A. (2015). Etudes du CEA sur les gainages avancés de combustible nucléaire pour un combustible REL avec une tolérance aux accidents améliorée, en APRP et au-delà. *La Revue Générale Nucléaire* 1, 14–20.

Brachet, J.C., Rouesne, E., Ribis, J., Guilbert, T., Urvoy, S., Nony, G., Toffolon-Masclet, C., Le Saux, M., Chaabane, N., Palancher, H., David, A., Bischoff, J., Augereau, J., Pouillier, E. (2020b). High temperature steam oxidation of chromium-coated zirconium-based alloys: Kinetics and process. *Corrosion Science* 167, 108537.

Cabrera, A., Vandenberghe, V., Besson, J., Le Saux, M., Brachet, J.C., Mardon, J.P., Hafidi, B. (2010). Finite element modeling of ring compression tests on post-quenched single side oxidized zirconium-based alloys (LOCA conditions). In: *International Topical Meeting on Light Water Reactor Fuel Performance*, pp. 261–269. Orlando, Florida, USA.

Cabrera, A. (2012). Modélisation du comportement mécanique "post-trempe", après oxydation à haute température des gaines de combustible des réacteurs à eau pressurisée. PhD thesis, Ecole des Mines ParisTech, France.

Courcelle, A., Millard, F., Gavoille, P., Le Saux, M., Bosonnet, S., Flament, J.L., Guilbert, T. (2014). A metallurgical-mechanical model to describe the behaviour at high temperature of EM10 for generation IV fast-reactor applications. In: *NuMat 2014: The Nuclear Materials Conference*. Florida, USA.

Glanowski, T., Le Saux, M., Le Saux, V., Huneau, B., Champy, C., Charrier, P., Marco, Y. (2023). Combined techniques and relevant image processing for quantitative statistical characterization of inclusions in elastomers. *Rubber Chemistry and Technology* 96(1), 59–89.

Gosset, D., Le Saux, M. (2015). In-situ X-ray diffraction analysis of zirconia layer formed on zirconium alloys oxidized at high temperature. *Journal of Nuclear Materials* 458, 245–252.

Gosset, D., Le Saux, M., Simeone, D., Gilbon, D. (2012). New insights in structural characterization of zirconium alloys oxidation at high temperature. *Journal of Nuclear Materials* 429(1), 19–24.

Guillou, R., Le Saux, M., Brachet, J.C., Hamon, D., Rouesne, E., Toffolon-Masclet, C., Béchade, J., Menut, D., Thiaudière, D. (2018). Structural evolutions and internal stresses in Zr alloys during oxidation at high temperature and subsequent cooling. In: *THERMEC'2018: 10th International Conference on Processing & Manufacturing of Advanced Materials*. Paris, France.

Guillou, R., Le Saux, M., Guinebretière, R., Castelneau, O., Béchade, J., Menut, D., Boudet, N., Blanc, N., Arnaud, S. (2019a). Evolutions structurales au sein d'un alliage de zirconium oxydé à haute température en diffraction des rayons X in situ au rayonnement synchrotron. In: *Colloque Réseau National de la Mťallurgie : La Métallurgie, Quel Avenir !* Nancy, France.

Guillou, R., Le Saux, M., Rouesne, E., Hamon, D., Toffolon-Masclet, C., Menut, D., Brachet, J.C., Béchade, J.L., Thiaudière, D. (2019b). In-situ time-resolved study of structural evolutions in a zirconium alloy during high temperature oxidation and cooling. *Materials Characterization* 158, 109971.

Klauke, R., Lips, M., Serrurier, N., Charrier, P., Le Saux, M. (2024). Analysis of the durability damage scenarios of air spring sleeves with axial reinforcements based on computer tomography and digital image processing. In: *XIII European Conference on Constitutive Models for Rubbers (ECCMR 2024)*.

Kwiatkowski, V. (2023). Fatigue de composites thermoplastiques à fibres courtes pour applications aéronautiques sous sollicitations de compression : loi de comportement et approche de dimensionnement. PhD thesis, ENSTA Bretagne, France.

Kwiatkowski, V., Le Saux, M., Le Saux, V., Leclercq, S., Marco, Y. (2022). Cyclic mechanical behaviour of a PEEK CF30 under compressive loadings. In: *International Conference on Advanced Computational Engineering and Experimenting (ACEX2022)*. Florence, Italy.

Kwiatkowski, V., Le Saux, M., Le Saux, V., Leclercq, S., Marco, Y. (2023). Fatigue of short carbon fiber reinforced PEEK under compression: Influence of the load ratio and predictions from heat buildup measurements. *Fatigue & Fracture of Engineering Materials & Structures* 46(7), 2396–2410.

Le Hong, T. (2020). Effets de l'oxygène et de l'hydrogène sur la microstructure et le comportement mécanique d'alliages de zirconium après incursion à haute température. PhD thesis, PSL Research University, Mines ParisTech, France.

Le Hong, T., Brachet, J.C., Crépin, J., Le Saux, M. (2021). Combined effects of temperature and of high hydrogen and oxygen contents on the mechanical behavior of a zirconium alloy upon cooling from the β_{Zr} phase temperature range. *Journal of Nuclear Materials* 554, 153069.

Le Hong, T., Turque, I., Brachet, J.C., Crépin, J., André, G., Barres, Q., Guillou, R., Toffolon-Masclet, C., Joubert, J.M., Le Saux, M. (2020). Phase transformations during cooling from the β_{Zr} phase temperature domain in several hydrogen-enriched zirconium alloys studied by in situ and ex situ neutron diffraction. *Acta Materialia* 199, 453–468.

Le Saux, M., Besson, J., Carassou, S. (2015). A model to describe the mechanical behavior and the ductile failure of hydrided Zircaloy-4 fuel claddings between 25 °C and 480 °C. *Journal of Nuclear Materials* 466, 43–55.

Le Saux, M., Besson, J., Carassou, S., Poussard, C., Averty, X. (2008). A model to describe the anisotropic viscoplastic mechanical behavior of fresh and irradiated Zircaloy-4 fuel claddings under RIA loading conditions. *Journal of Nuclear Materials* 378(1), 60–69.

Le Saux, M., Besson, J., Carassou, S., Poussard, C., Averty, X. (2010). Behavior and failure of uniformly hydrided Zircaloy-4 fuel claddings between 25 °C and 480 °C under various stress states, including RIA loading conditions. *Engineering Failure Analysis* 17(3), 683–700.

Le Saux, M., Brachet, J.C., Vandenberghe, V., Gilbon, D., Mardon, J., Sebbari, B. (2011). Influence of pre-transient oxide on LOCA high temperature steam oxidation and post-quench mechanical properties of Zircaloy-4 and M5™ cladding. In: *2011 Water Reactor Fuel Performance Meeting*. Chengdu, China.

Le Saux, M., Brachet, J.C., Vandenberghe, V., Rouesne, E., Urvoy, S., Ambard, A., Chosson, R. (2019). Effect of a pre-oxide on the high temperature steam oxidation of Zircaloy-4 and $M5_{Framatome}$ alloys. *Journal of Nuclear Materials* 518, 386–399.

Le Saux, M., Guilbert, T., Brachet, J.C. (2018). An approach to study oxidation-induced stresses in Zr alloys oxidized at high temperature. *Corrosion Science* 140, 79–91.

Le Saux, M. (2008). Comportement et rupture de gaines en Zircaloy-4 détendu vierges, hydrurées ou irradiées en situation accidentelle de type RIA. PhD thesis, Ecole Nationale Supérieure des Mines de Paris, France.

Le Saux, M., Brachet, J.C., Vandenberghe, V., Ambard, A., Chosson, R. (2020). Breakaway oxidation of zirconium alloys exposed to steam around 1000 °C. *Corrosion Science* 176, 108936.

Le Saux, M., Le Bail, J.B., Becker, J., Caër, C., Charrier, P., Le Saux, V., Maheo, L., Marco, Y. (2023). Statistical characterization of microcellular polyurethane foams microstructure based on 2D and 3D image analysis. *Journal of Cellular Plastics* 59(5–6), 395–417.

Leveuf, L. (2017). Caractérisation et modélisation du comportement mécanique et de la tenue en fatigue d'un composite thermoplastique à fibres de carbone courtes pour applications aéronautiques. PhD thesis, Université Bretagne Loire, France.

Marckmann, G., Chagnon, G., Le Saux, M., Charrier, P. (2016). Experimental investigation and theoretical modelling of induced anisotropy during stress-softening of rubber. *International Journal of Solids and Structures* 97–98, 554–565.

Michau, A., Maury, F., Schuster, F., Lomello, F., Brachet, J.C., Rouesne, E., Le Saux, M., Boichot, R., Pons, M. (2018). High-temperature oxidation resistance of chromium-based coatings deposited by DLI-MOCVD for enhanced protection of the inner surface of long tubes. *Surface and Coatings Technology* 349, 1048–1057.

Navrátil, L., Leveuf, L., Le Saux, V., Marco, Y., Olhagaray, J., Leclercq, S., Moyne, S., Le Saux, M. (2020). A model to describe the cyclic anisotropic mechanical behavior of short fiber-reinforced thermoplastics. *Mechanics of Time-Dependent Materials* 24, 481–503.

Nguyen, D.V. (2021). Comportement mécanique à température ambiante d'un revêtement de chrome déposé sur un substrat en alliage de zirconium. PhD thesis, Université Paris–Saclay, France.

Nguyen, D.V., Le Saux, M., Gélébart, L., Brachet, J.C., Bonthonneau, J.P., Courcelle, A., Guillou, R., Rouesne, E., Urvoy, S. (2022). Mechanical behavior of a chromium coating on a zirconium alloy substrate at room temperature. *Journal of Nuclear Materials* 558, 153332.

Santharam, P. (2020). Thermomechanical investigation for the fatigue design of short glass fibers reinforced plastic parts. PhD thesis, ENSTA Bretagne, France.

Santharam, P., Marco, Y., Le Saux, V., Le Saux, M., Robert, G., Raoult, I., Guévenoux, C., Taveau, D., Charrier, P. (2020). Fatigue criteria for short fiber-reinforced thermoplastic validated over various fiber orientations, load ratios and environmental conditions. *International Journal of Fatigue* 135, 105574.

Turque, I., Chosson, R., Le Saux, M., Brachet, J.C., Vandenberghe, V., Crépin, J., Gourgues-Lorenzon, A. (2018). Mechanical behavior at high temperature of highly oxygen- or hydrogen-enriched α and (prior-) β phases of zirconium alloys. In: *Zirconium in the Nuclear Industry : 18th International Symposium, ASTM STP 1597*, pp. 240–280. ASTM International, West Conshohocken, PA.

Turque, I. (2016). Effet de fortes teneurs en hydrogène sur les propriétés métallurgiques et mécaniques des gaines en alliage de zirconium après incursion à haute température. PhD thesis, PSL Research University, Mines ParisTech, France.

Vandenberghe, V., Brachet, J.C., Le Saux, M., Gilbon, D., Billone, M., Hamon, D., Mardon, J.P., Hafidi, B. (2010). Influence of the cooling scenario on the post-quench mechanical properties of pre-hydrided Zircaloy-4 fuel claddings after high temperature steam oxidation (LOCA conditions). In: *International Topical Meeting on Light Water Reactor Fuel Performance*, pp. 270–277. Orlando, Florida, USA.

Zimmermann de Almeida, O., Carrère, N., Le Saux, M., Le Saux, V., Moreau, G., Pannier, Y., Castagnet, S., Marco, Y. (2025). Compression-compression fatigue of quasi-isotropic laminates: failure mechanisms and link between dissipative behavior and fatigue life. *International Journal of Fatigue* 193, 108780.

Contribution à l'étude de la réponse de matériaux hétérogènes soumis à des sollicitations environnementales et mécaniques

Résumé : Ce document fait la synthèse d'une quinzaine d'années de recherche, à vocation appliquée, sur la réponse de matériaux hétérogènes soumis à des sollicitations environnementales et mécaniques. Une partie de ces activités de recherche porte sur la réponse de matériaux métalliques soumis à des variations importantes de température, à un environnement oxydant et à des sollicitations mécaniques. Les matériaux étudiés comprennent des alliages de zirconium, des alliages de zirconium revêtus de chrome et un acier martensitique. Les problématiques abordées incluent la corrosion à haute température, le comportement mécanique, la rupture, et l'influence des évolutions microstructurales et des hétérogénéités induites par les variations de température et la corrosion (changements de phases et absorption d'oxygène et d'hydrogène par exemple). Une autre partie des activités de recherche présentées porte sur la réponse de matériaux hétérogènes à base de polymères soumis à des chargements mécaniques cycliques, dans des environnements (température et humidité notamment) susceptibles de varier dans certains cas. Les travaux exposés portent sur le comportement thermomécanique et la tenue en fatigue de différents matériaux incluant des composites à matrice thermoplastique renforcée de fibres courtes, des composites à matrice thermodurcissable renforcée de fibres longues et des mousses élastomères. La démarche mise en œuvre associe caractérisation expérimentale, modélisation et simulation numérique.

Mots clés : matériaux métalliques, matériaux polymères, matériaux composites, comportement thermomécanique, fatigue, corrosion à haute température, microstructure, caractérisation expérimentale, modélisation, simulation numérique

---

Contribution to the study of the response of heterogeneous materials subjected to environmental and mechanical loading

Abstract: This document presents a summary of approximately fifteen years of applied research into the response of heterogeneous materials to environmental and mechanical loading. One area of focus within this research is the response of metallic materials to wide temperature variations, an oxidizing environment, and mechanical loading. Materials under investigation include zirconium alloys, chromium-coated zirconium alloys, and a martensitic steel. The following issues are addressed: high temperature corrosion, mechanical behavior, failure, and the influence of microstructural changes, and heterogeneities induced by temperature variations and corrosion (phase changes and oxygen and hydrogen absorption, for example). Another area of focus in the research is the response of heterogeneous polymer-based materials to cyclic mechanical loading in environments (temperature and humidity in particular) that may vary in certain cases. The work presented examines the thermomechanical behavior and fatigue life of a range of materials, including short fiber-reinforced thermoplastic matrix composites, long fiber-reinforced thermoset matrix composites, and elastomer foams. The methodology employed integrates multiscale experimental characterization, modeling, and numerical simulation.

Keywords: metallic materials, polymeric materials, composite materials, thermomechanical behavior, fatigue, high temperature corrosion, microstructure, experimental characterization, modeling, numerical simulation